
# Ammonia Synthesis on Proton-enriched Palladium Substrate

Thesis submitted for the degree of
Doctor Philosophiæ

CANDIDATE:
Lorenzo Paulatto

SUPERVISOR:
Prof. Stefano de Gironcoli

December 2009

*I think it is a sad reflection on our civilization that while we can and do measure the temperature in the atmosphere of Venus we do not know what goes on inside our soufflés.*

Nicholas Kurti

# Table of Contents

# Introduction

Production of Ammonia is one of the most important in the chemical industry; most of the Ammonia produced is then converted to other Nitrogen-containing molecules, such as anhydrous ammonium nitrate or urea, which are typically used for inhorganic fertilizers. The standard industrial reaction for the production of Ammonia is the Haber-Bosch Process (sec. 1.1); an high-pressure and high-temperature process known and developed since the early twentieth century [31, 11]. The Haber-Bosch process produces Ammonia directly from its components, Nitrogen and Hydrogen, supplied in gas form. Although successful, this industrial process, consumes a large amount of energy which, given the huge production volume, employs a significant percentage of total world energy production and natural gas consuption [70].

Because of its economical importance, improving the Ammonia production process is still an open challenge and a rich field of research. A search in related journal archives for papers regarding Ammonia production typically returns hundreds or thousands of results; nevertheless there is still room for improvement and better understanding of the reaction.

A part of the studies have been focused on improving the Haber-Bosch process itself; e.g. replacing the original Iron catalyst with more efficient metal alloys. However other studies have tried to find novel reaction mechanisms, that could possible overcome the high-pressure and high-temperature requirements. Some studies have been based on certain biological process, occuring in bacteria, that can produce Ammonia at room temperature and pressure [77, 68, 24]. In the biological process the energy required by the reaction is not supplied

thermally but by reduction of adenosine triphosphate (ATP) molecules, which makes them difficult to reproduce in vitro.

Another possible approach is to supply the required energy electrochemically, by applying an external electric field to a solid-state catalyst, or having a certain amount of current circulating through it, it is possible to transfer to the reactants the necessary amount of energy. The electrical source can also act in an indirect way, modifying the nano-scale properties of the catalyst in a way that improves its properties; this effect is called non-Faradayc Electrochemical Modification of Catalytic Reaction (NEMCA) [56, 80].

In 1998 Stoukides and coworkers [50, 49] (sec. 1.2)demonstrated the possibility of producing Ammonia at atmospheric pressure by supplying the required amount of Hydrogen via a proton-conducting perovskite. The perovskite, in the form of a little brick or a pipe, is coated on two sides with a Palladium paste, obtaining two catalytic surfaces separated by a proton conductor. The two catalysts are then connected through an electrical circuit and a certain bias is applied, making them act as an anode and a cathode. When the anode is exposed to molecular Hydrogen, $H_2$ dissociates spontaneously. Because of the bias, the Hydrogen atoms are stripped of their electron and forced to cross the proton conductor; the electron will instead travel through the external electrical circuit; recombination of protons and hydrogens happens in the cathode. The cathode itself is exposed to Nitrogen gas.

Combining this electrochemical mechanism with high temperature (between 500° C and 750° C) the author were able to induce a steady flux of Ammonia, with a high conversion efficiency. They also proposed the presence of a NEMCA effect, although weak. In the present work we will re-examine the original experiment and tackle its characteristic and inner mechanics at the nano-scale level. We will use ab-initio methods (chap. 2) to construct a model of the catalytic process and simulate its intermediate steps. In our study we have used the computational tools provided by the Quantum-ESPRESSO distribution [28]. In particular we will use Density Functional Theory (sec. 2.2) and the Projector-Augmented Wave method (PAW, sec. 2.3) to reproduce the electronic structure of the system; the Born-Oppenheimer approximation, together with the Hellmann-Feynman theorem, will be

implicitly used to optimize the nanoscopic structure, and find intermediate steps of the reactions. We will also used the Transition State Theory (sec. 3.3) and the Nudged-Elastic Band method (sec. 3.4) to estimate the energy barriers involved in the reaction and, consequently, the reaction rate.

In chapter 4 we will examine the catalyst structure in detail; in particular we will focus on the effect of active Hydrogen pumping by mean of the applied cell potential. In section 4.1 we will see how a cell potential of realistic amplitude can force a very large amount of Hydrogen in the Palladium bulk. The resulting system, called Palladium hydride, can undergo a phase transition that changes its unit-cell volume up to 10%; we will see the details of this phase change and the possibly resulting structures.

In section 4.2 we will move our focus to the catalyst surface. We will tackle the problem of determining the adsorbed Hydrogen population, in the case of normal Palaldium and Palladium hydride. This complex problem involves a three-phase equilibrium, where the chemical potentials of Hydrogen in the gas and Hydrogen adsorbed in the bulk or on the surface have to be equal. In order to estimate the chemical potential we will use a Monte Carlo simulation built on top of a simplified model where the total energy is computed as a sum of adsorption on-site energies and neighbour-site interactions.

Finally, in chapter 5, we will tackle the core of the problem, trying to find a suitable reaction path for the Ammonia production. We will examine the possibility of Nitrogen dissociative adsorption as well as the possiblity of Nitrogen hydrogenation prior to its dissociation. The former will be easily proved impossible, at the experimental conditions, so we will focus on the subsequent hydrogenations of the $N_2$ molecules. We will examine the process up to the final breaking of the N–N bond, where the formation of Ammonia can proceed without further barriers. An order of magnitude estimate of the Ammonia production in the system will be made and found to be compatible with the experimental findings.

# Chapter 1

# Production of Ammonia

*In the first section of this short chapter we will present the Haber-Bosch process: the traditional and only industrial-grade process for production of Ammonia, its characteristics and main drawbacks.*

*In the second section we will instead review the experiments of Soukides et. al. [49, 50] which proved it possible to produce Ammonia at dramatically different conditions than the usual, namely at low pressure. We will discuss the experimental results and report some of the original paper arguments, trying to put them in the frame of our work.*

## 1.1 Industrial production of Ammonia: the Haber-Bosch Process

The Haber-Bosch process is named after the German chemist Fritz Haber who invented it in 1909 and Carl Bosch who developed the necessary technology to scale it up to industrial-level production. Both authors were awarded a Nobel prize for they discoveries, in 1918 and 1931 respectively [31, 11].

The process produces Ammonia, starting from Nitrogen and Hydrogen, using an enriched-iron catalyst:

$$3H_2 + 2N_2 \rightleftharpoons 2NH_3 + 2\varepsilon \tag{1.1}$$

The reaction is exothermal, it releases an energy $\varepsilon = 92.4$kJ/mol which corresponds to 958 meV per Ammonia molecule produced. Moreover the process produces two moles of gas out of 5, hence, according to Le Chatelier's principle, production of Ammonia is favoured by high pressure while at low pressure the equilibrium will move toward the reactants.

The reaction proceeds according to the following intermediate steps:

- $N_2^g \rightarrow N_2^\star$
- $\mathbf{N_2^\star \rightarrow 2N^\star}$ *rate limiting step*
- $H_2^g \rightarrow H_2^\star$
- $H_2^\star \rightarrow 2H^\star$
- $N^\star + 3H^\star \rightarrow NH_3^\star$
- $NH_3^\star \rightarrow NH_3^g$

The star indicates an adsorbed species, while the super-script $g$ indicates that the species is in the gas phase.

In this process the dissociative adsorption of Nitrogen is the rate limiting step; the strong triple bond of $N_2$ requires more than 10 eV to be broken in the gas phase and, even on the best available catalysts, it cannot proceed at low temperature. To improve the dissociation the industrial process employs temperatures between 300° C and 550° C. As a drawback high temperature moves the chemical equilibrium toward the reactants reducing the conversion rate to unacceptably low levels. To compensate for this the reaction has to be carried at high pressure, typically between 150 and 250 bar; nevertheless the resulting conversion rate is only about 15%, thus the process must use several passes to completely convert the reactants.

## 1.2 Electrochemical production of $NH_3$ at Atmospheric pressure

Production of Ammonia from Hydrogen and Nitrogen at atmospheric pressure has been proved experimentally for the first time in 1998 using an electro-chemical method [49, 50]. The basic elements of the experimental setups are a Palladium catalyst deposited on top of a strontia-cerbia-ytterbia perovskite of composition $SrCe_{0.95}Yb_{0.05}O_3$. In these experiments two different setups were used. The first setup consists a single chamber, where Nitrogen and Hydrogen are fed directly, mixed to stoichiometric ratio, and diluted with inert Helium gas. Inside the chamber there is a suspended perovskite disk covered with the Palladium catalyst on both sides. The other setup consists of two chambers, namely the interior and exterior of a perovskite cylindrical container, which is itself placed inside a larger quartz container. A region of the perovskite container is covered with Palladium on two sides, one exposed to Hydrogen, the other exposed to Nitrogen diluted in Helium. The structure of the experimental setups are represented in figure 1.1. In both cases the temperature is kept between 550°C and 750°C.

In both setups the two pieces of Palladium catalysts are connected to a voltage source, which makes them act as an anode and a cathode. In the double chamber setup the catalyst exposed to Hydrogen is the positively-charged anode, while the cathode is exposed to the Nitrogen gas. Provided that Hydrogen dissociates spontaneously on Palladium surface, and because the perovskite is a good proton-conductor, a steady flow of protons is established from anode to cathode. Measuring the circuit current, it is easy to estimate the amount of protons that flows through the perovskite; in the double-cell setup it corresponds exactly to the amount of Hydrogen available for reacting with Nitrogen. In the single-chamber setup it is not necessary for all the Hydrogen to pass through the proton-conductor, as it can dissociate directly on the Cathode, nevertheless also in this case the circuit of current can be simply related to the number of protons that go through the perovskite. The applied bias ranges from 0.4V to 2.0V.

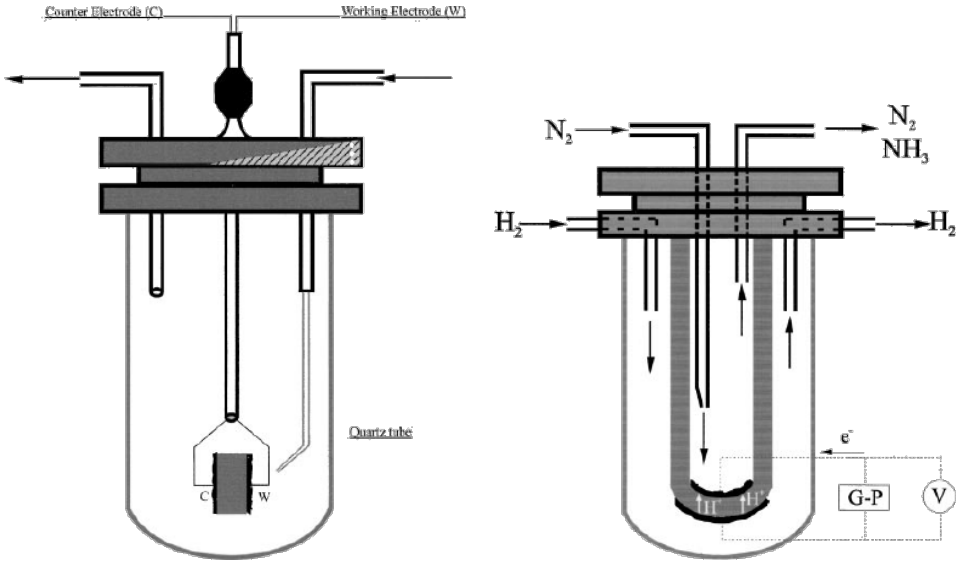


Figure 1.1: The experimental setup used to produce Ammonia; on the left the single-chamber reactor and on the right double-chamber one (from ref. [50]).

### 1.2.1 Effect of Cell Potential on Ammonia Formation

When the circuit was open a negligible production of Ammonia was observed. When the circuit was closed the production rate increased for about 2 to 6 minutes and then stabilized at a value several orders of magnitude higher than for the open circuit.

The applied voltage can act in two way to modify the conditions of the reaction. The first possible mechanism is purely Faradayc, i.e. it depends only on the shift of chemical potential due to the flow of current. The second effect is the so-called non-Faradayc Electrochemical Modification of Catalytic Reaction (NEMCA), which requires the properties of the catalyst to be substantially modified by the experimental details. The presence of a shift in the chemical equilibrium can be proved with an argument based on the electrochemical enhancement of the reaction. We briefly rephrase here the original argumentation as presented in ref. [50].

The enhancement factor, $\Lambda$, is defined as the rate of Hydrogen consumption over the rate of electro-chemically supplied Hydrogen; if the current flowing through the circuit is $I$ it is

defined as:

$$\Lambda = \frac{\Delta n_{H2}}{I/2F} \tag{1.2}$$

where $\Delta n_{H2}$ is the molar Hydrogen consumption per second and $F$ is the Faraday constant, i.e. the charge of a mole of protons. Clearly in the double chamber experiment $\Lambda$ cannot be higher than 1, as all the Hydrogen supplied to the reaction has to be supplied electrochemically. Conversely, in the single chamber experiment it is possible to achieve higher values of $\Lambda$, e.g. a value $\Lambda = 100$ would mean that for the flow of a single Hydrogen through the perovskite proton-conductor 100 more are consumed in the production of Ammonia. It is possible to estimate $\Lambda$ experimentally, measuring the amount of Ammonia produced and the current flowing through the circuit.

In the original work the authors measured values of $\Lambda$ between 1 and 2, thus proving the presence of a NEMCA effect, although relatively weak. The presence of a NEMCA effect implies a change of the catalytic mechanism, which can either come from a change in the rate limiting step barrier, i.e. the dissociation of Nitrogen, or from a more dramatic change in the reaction path. We will go back to this subject, which happens to be the main focus of our work, in chapter 4, where we will examine the structure of the Palladium catalyst in detail, and in chapter 5, where we will study the chemical reaction.

### 1.2.2 Electro-chemical Power Balance

In this section we are going to seen how the electrical power supplied to the experimental system is internally dissipated or used. What we are really interested in is how the electrical power can change the effective chemical potential of Hydrogen in the Palladium-based catalyst; this subject will be threated more in-depth in the next section, for now we only want to give a quick overview of the energy scales involved in the experiment.

During the experiment several different values of cell potential and, depending also on other factors such as the kind of setup and the partial pressure of the species in the gas phase, different values of current intensity were measured.

First of all part of the energy is take away by the products; even if Ammonia is more stable, i.e. it has a higher internal chemical energy, than its the reactants, this is not the only factor in the power balance. The experimental team [50, 48, 59] developed a sophisticated thermodynamical argument which, assuming the setup to be isothermal, proves how the production of Ammonia actually consumes a certain amount of energy. We are not going to review the argument in-depth, as it is mainly focused on determining the process power efficiency, but we wish to restate the main point in a more informal way.

The crucial point of the balance is the isothermal assumption. If we assume the experimental cell to work adiabatically it is trivial, i.e. because $NH_3$ has a higher binding energy than its components, the change of Enthalpy per mole of Ammonia produced ($\Delta H$) is simply the binding energy difference between one mole of $NH_3$ and half mole of $N_2$ plus 3/2 moles of Hydrogen. On the other hand, if we impose the temperature of reactant and products to be equal and constant, the difference between the partition functions of the various species can dramatically change the balance. Let's take a typical, although idealized, case from the experiment as an example: we keep the cell at 900 K and feed it with a stoichiometric flow of $H_2$ at 6kBar and $N_2$ at 2kBar. If we assume a 100% conversion rate we will have an outgoing flow of 4kBar Ammonia gas. Under these specific conditions the gas-phase chemical potential of the species are $-1.47$ eV for $H_2$, $-2.12$ eV for $N_2$ and $-2.11$ eV for $NH_3$; multiplying them by the stoichiometric coefficient of the reaction we find that it consumes 1.15 eV of thermodynamical energy per Ammonia molecule produced; this loss is partly compensated by the stronger chemical bonds of Ammonia, with a net a cost of 95 meV per $NH_3$ molecule.

In general, given or measured the composition of chemical species entering and exiting the experimental cell, it is possible to determine the amount of energy necessary to keep the reaction steady. In the experimental conditions it turns out to be a small amount of the total power, only about 15%; the exact fraction depends significantly on the detail and on the free parameters of the experiment, such as the temperature, the current intensity and the cell potential.

The other effect that contributes to dissipate the electrical power is the resistance of the

proton conductor. It is also possible to estimate experimentally this resistance, $R_{\text{cell}}$ and, known the circuit current, it is easy to compute the fraction of electrical power it dissipates; it turns out to be about 50% of the total electrical power. Again this is only an estimate; a more precise value would depend on the precise value of experimental free parameters.

The remaining fraction of the power, about 35% of the total, is dissipated by some other mechanism. In particular at high temperature the Perovskite is not a perfect electron insulator, hence it can dissipate some more current; some experimental studies indicate that this effect can dissipate up to 20% of the total power [75]. Furthermore some other kind of ions, not just simple protons, can cross the perovskite. Finally, the protons can also encounter some resistance, and thus dissipate some power, while crossing the Perovskite-Palladium interface and the Palladium bulk.

### 1.2.3 Cell Potential as Effective Chemical Potential

We have see how the cell potential contributes to pump Hydrogen through the proton conductor inside the catalyst bulk, this effect can be modeled as an effective chemical potential for Hydrogen, which would add up to the real one to determine the Hydrogen population in the catalyst. As we have seen in the previous section, the bias difference between the two Pd–perovskite interfaces can be estimated experimentally, and account for about half of the total cell potential. However on the interfaces there will be a certain amount of polarization, which causes the formation of two overpotentials: $\eta_A$ on the anode and $\eta_C$ on the cathode. In our system anode and cathode where prepared with the same technique and with the same material; we can roughly expect $\eta_A \sim \eta_C$, but it is important to stress that they don't have to be equal as the polarization direction is opposite.

According to reference [30], once the overpotential is known, the effective chemical potential ($\Delta\mu$) can be estimated as

$$\Delta\mu = -e\left(\Delta V - \eta_A - \eta_C\right) . \tag{1.3}$$

Instead of estimating the overpotential with a complex nano-scale model, which would anyway depend on the detail of the metal-perovskite interface, we have decided to rely on

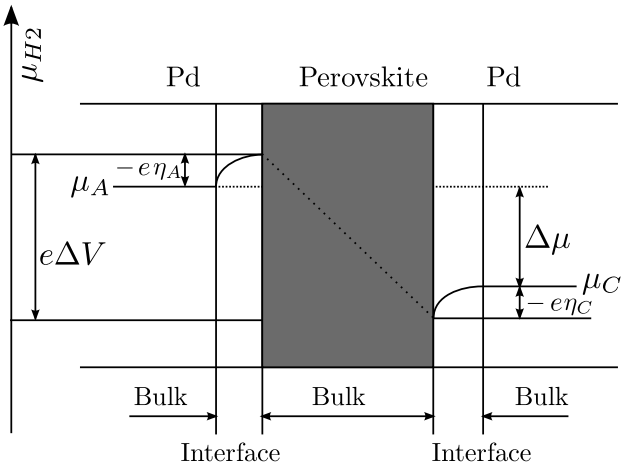


Figure 1.2: A qualitative representation of the effective chemical potential generated by the cell potential (adapted from ref. [30])

experimental data available on the subject. In particular two recent papers [62, 75] have examined a similar problem, with the same kind of proton-conductor and in the same range of temperature and partial Hydrogen pressure, but with different metals at the cathode. This two studies estimate, in the relevant range of current intensity and temperature, a total overpotential ($\eta_C + \eta_A$) of about 0.4 V. Another paper [69] studies the overpotential of Palladium-perovskite[1] interface and Platinum-perovskite interface but with a different kind of perovskite ($SrZr_{0.9}Y_{0.1}O_{3\alpha}$). The value measured for the overpotential is similar to the previous works for Platinum, but dramatically lower, less than 0.1 V for Palladium; however the Palladium sample was prepared with a sputtering technique specifically aimed at reducing the overpotential. In both cases the overpotentials depend strongly on the current density per unit of interface surface; the values we have reported correspond to 1 mA.

In the Ammonia production experiment the very first sign of a NEMCA effect arises when the total cell potential reaches about 0.8 V. In this specific, and quite extreme, case the bias between the two perovskite interfaces is measured to be only one third of the total cell

[1] In the reference a pressure gradient is induced and the bias is measure, as a consequence the effect of the overpotential is inverted; the reason is that $\eta$ will always work against the forcing effect, reducing $\Delta\mu$ if $\Delta V$ is applied and reducing $\Delta V$ if $\Delta\mu$ is applied.

potential, about 0.25 V. This can sets an upper bound to the total interface overpotential, and hints to it being somewhere in the middle of the different values from literature.

Even though we are not able to give a precise value for the effective chemical potential, we can still infer a good enough estimate for the purpose of our research. In the Ammonia production reaction a sensible NEMCA effect was measured for values of the cell potential in the range between 1.5 V and 2 V; which, even in the most pessimistic case, correspond to an effective chemical potential shift between 0.35 eV and 0.60 eV. As we will see in chapter 4 a change in chemical potential of the 0.30 eV is sufficient to induce a substantial change in the catalyst structure.

### 1.2.4 Hydrogen Transport Through Palladium-covered Perovskite

In the previous section we have seen how the bias applied to the Palladium electrodes can affect the chemical potential of Hydrogen inside the Palladium bulk, in the region close to the interface with the perovskite. As we have seen we can expect an effective chemical potential difference in the order of 0.50 eV. However, this raises an apparent contradiction with another property of the system: the partial pressure of Hydrogen on the Palladium-gas interface is the same on the two sides of the perovskite, hence also the chemical potential of the $H_2$ gas is the same. Because the surface has to be in equilibrium with the gas we could infer that the chemical potential of Hydrogen ($\mu_H$) has to be constant from the surface of the anode to the surface of the cathode.

The explanation is that the system is not in equilibrium, but in a steady state were a constant flux of Hydrogen is established from anode to cathode, hence its chemical potential throughout the system does not need to be constant. The protons are dragged through the perovskite by the external electric field; but inside the Palladium bulk the field is totally screened. From the surface of the Palladium to the Palladium-perovskite interface Hydrogen atoms moves *because* of the gradient of the chemical potential.

To make the argument clearer we have represented qualitatively the shape of both $\mu_H$ and the Hydrogen density $\rho_H$ in figure 1.3. As we will see in chapter 4 the two gas-metal interface

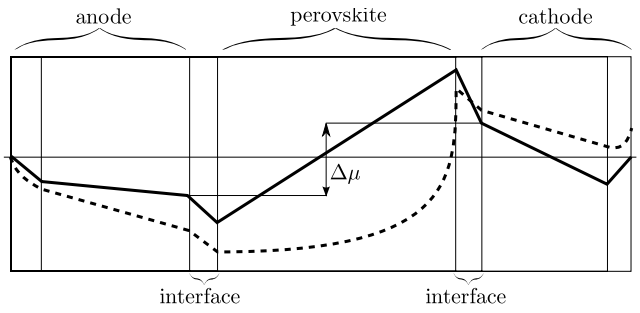


Figure 1.3: A qualitative representation of the Hydrogen chemical potential (solid line) and its density (dashed line) from the surface of the anode to the surface of the cathode.

can have different characteristics, hence the Hydrogen density does not need to be equal on the extremes. Conversely, the chemical potential on the surface must be the same as in the gas, while the difference $\Delta\mu$ is what we have discussed in the previous section. The active removal of Hydrogen from the anode-perovskite interface and its addition to the cathode-perovskite interface perturbs the chemical potential; its gradient drives the Hydrogen atoms through the two metal layers.

# Chapter 2

# Ab-initio Electronic Structure Calculation

*In these chapter we will briefly review the theoretical background underlying the computational methods we have used in the present work. In the first section we will see how to simplify an atomic-scale problem using the Born-Oppenheimer approximation and, in the next section, the Density Functional Theory (DFT).*

*In section 2.3 we will discuss in some depth the Projector-Augmented Wave method (PAW); this formalism can be used to perform DFT calculation of all-electron quality on a basis of planewaves. At first we will briefly discuss its main characteristics and our implementation, then we will present a series of computational tests where PAW calculations will be compared to all-electron and ultrasoft ones. We will finally comment these results to outline the main advantages and drawbacks of PAW method.*

## 2.1 Born-Oppenheimer Approximation

In principle, when studying a physical system, such as a molecule or the surface of a metal crystal at the nano-scale, both electrons and nuclei have to be treated in a quantum-

mechanical framework; consequently all degrees of freedom, electronic and ionic, should be dealt with simultaneously. The Hamiltonian operator for the system can be written in the following form:

$$\begin{aligned} H &= -\sum_{I=1,N_I} \frac{\hbar^2}{2M_I}\nabla^2_{\mathbf{R}_I} - \sum_{i=1,N_e} \frac{\hbar^2}{2m_e}\nabla^2_{\mathbf{r}_I} \\ &+\frac{1}{2}\sum_{i\neq j} \frac{e^2}{|\mathbf{r}_i - \mathbf{r}_j|} - \sum_{i,I} \frac{Z_I e^2}{|\mathbf{r}_i - \mathbf{R}_I|} + \frac{1}{2}\sum_{I\neq J} \frac{Z_I Z_J e^2}{|\mathbf{R}_I - \mathbf{R}_I|}, \end{aligned} \tag{2.1}$$

where $N_I$ and $N_e$ are the number of nuclei and electrons respectively, their coordinates being $\mathbf{R}_I$, for nuclei and $\mathbf{r}_i$ for electrons. Following a widespread notation we use upper-case indeces $I, J$ for nuclei, while lower-case indeces $i, j$ are reserved for electrons. Furthermore, $M_I$ and $Z_I e$ are the mass and charge of the I-th nucleus, while the electronic mass and charge are $m_e$ and $-e$ respectively.

The Born-Oppenheimer approximation, introduced in 1927, can be used to factorize the system wavefunction $\Phi(\mathbf{R}, \mathbf{r})$, in a nuclear and an electronic part:

$$\Phi(\mathbf{R}, \mathbf{r}) = \phi(\mathbf{R})\psi_{\mathbf{R}}(\mathbf{r}), \tag{2.2}$$

where we collectively indicate the ensemble of nuclear and electronic coordinates with $\mathbf{R}$ and $\mathbf{r}$ respectively; the action of the kinetic energy of the nuclei on $\psi_{\mathbf{R}}(\mathbf{r})$ is neglected. This approximation can be justified assuming the momentum of electrons to be comparable in magnitude to the momentum of nuclei; which is justifiable *a posteriori* by noting that for tightly bound electrons $\psi_{\mathbf{R}}(\mathbf{r})$ is approximately $\psi(\mathbf{r} - \mathbf{R})$. Under this assumption the kinetic energy of nuclei can be neglected, due to the high $M_I/m$ ratio. Neglecting the kinetic energy operator for nuclei we can solve the electronic problem with *clamped* or *frozen* nuclei: the ground state electronic wavefunction becomes a parametric function of the nuclear positions.

The electronic Hamiltonian can be written in the following form:

$$\begin{aligned} \Bigg( &-\sum_{i=1,N_e} \frac{\hbar^2}{2m_e}\nabla^2_{\mathbf{r}_i} + \frac{1}{2}\sum_{i\neq j} \frac{e^2}{|\mathbf{r}_i - \mathbf{r}_j|} \\ &-\sum_{i,I} \frac{Z_I e^2}{|\mathbf{r}_i - \mathbf{R}_I|} + E_{\text{ions}} \Bigg) \psi_{\mathbf{R}}(\mathbf{r}) &= E(\mathbf{R})\psi_{\mathbf{R}}(\mathbf{r}), \end{aligned} \tag{2.3}$$

where the term $E_{\text{ions}} = \frac{1}{2}\sum_{I\neq J}\frac{Z_I Z_J e^2}{|\mathbf{R}_I-\mathbf{R}_J|}$, is only a constant and thus plays no role in the solution of the electronic problem.

In principle it is possible to solve equation 2.3 for any configuration of the nuclei, finding the corresponding electronic ground-state and its energy. If necessary this information can be used to write the nuclear Hamiltonian in the following way:

$$\left(-\sum_{I=1,N_I}\frac{\hbar^2}{2M_I}\nabla^2_{\mathbf{R}_I}+E(\mathbf{R})\right)\phi(\mathbf{R})=\varepsilon\phi(\mathbf{R})\,, \tag{2.4}$$

where the nuclear kinetic energy has been reintroduced. More often a classical treatment of the nuclei, e.g. by molecular dynamics, is sufficient.

For this purpose, it is possible to calculate the forces acting on the nuclei at a given configuration using only the electronic ground-state information thanks to the Hellmann-Feynman theorem:

$$\begin{aligned}\mathbf{F_I}(\mathbf{R}) &= -\frac{\partial E(\mathbf{R})}{\partial \mathbf{R}_I}\\ &= -\left\langle\psi_{\mathbf{R}}(\mathbf{r})\left|\frac{\partial H(\mathbf{R})}{\partial \mathbf{R}_I}\right|\psi_{\mathbf{R}}(\mathbf{r})\right\rangle,\end{aligned} \tag{2.5}$$

where $\mathbf{F}_I(\mathbf{R})$ is the force acting on the I-th nuclei, at position $\mathbf{R}$. It is worth mentioning that the partial derivative of $H(\mathbf{R})$ can usually be computed analytically, allowing us to calculate forces without having to resort to numerical approximations, such as finite-difference derivatives.

## 2.2 Density Functional Theory

### 2.2.1 Introduction and Historical Note

In the previous section we have seen that Born-Oppenheimer approximation can separate the Hamiltonian of a chemical-physical system in an electronic and a nuclear part, making the problem much more tractable. Nevertheless the electronic ground state wavefunction is

still a function of all the electron coordinates, namely $3N_e$ degrees of freedom, which double if we also consider the spin; furthermore the electrons are interacting particles, thus the resulting system is a many-body problem in a fixed external potential. As every electron interacts with each other, complexity increases exponentially with the number of particles: finding the ground-state wavefunction becomes an intractable problem for any system of realistic, although nano-scopic, size.

An important breakthrough toward a practical solution of this problem came in 1964, when Hohenberg and Kohn [36] demonstrated that the ground-state energy of a system only depends, as a functional, on the ground state electron density. This result alone, although important, does not make the search for a solution any easier, as the functional form is unknown. Nevertheless, the next year Kohn and Sham [40] proposed an important development where the kinetic and interaction density functional was split in three terms: the kinetic energy of an auxiliary non-interacting system, with the same ground state density as the real system, the classical electrostatic (Hartree) interaction energy and a remainder, named Exchange and Correlation (XC) energy functional, for which an effective approximation was given by the Local Density Approximation (LDA). This decomposition set the ground for the practical use of Density Functional Theory.

### 2.2.2 Theory Elements and Formalism

In a quantum mechanical treatment the potential exerted by the atomic nuclei is considered a static external potential $V_{\text{ext}}$, electronic state is then described by the many-body $3N$-variables wavefunction $\Psi(\{\mathbf{r}\}) = \Psi(\mathbf{r}_1, \ldots, \mathbf{r}_N)$ satisfying the many-electron Schrödinger equation. If we use $\hat{T}$ to indicate the kinetic-energy operator and $\hat{U}$ to indicate the electron-electron interaction we have:

$$\begin{aligned}
\hat{H}\Psi(\{\mathbf{r}\}) &= \left(\hat{T}+\hat{V}_{\text{ext}}+\hat{U}\right)\Psi(\{\mathbf{r}\}) && (2.6)\\
&= \left(\sum_{i}^{N} -\frac{\hbar^2}{2m}\nabla_i^2 + \sum_{i=1,N_e} V_{\text{ext}}(\mathbf{r}_i) + \frac{1}{2}\sum_{i\neq j}^{N} U(\mathbf{r}_i,\mathbf{r}_j)\right)\Psi(\{\mathbf{r}\}) && (2.7)\\
&= E\Psi(\{\mathbf{r}\})\,.
\end{aligned}$$

The operator $\hat{V}_{\text{ext}}$ is the system-dependent external potential: Hohenberg and Kohn proved that $V_{\text{ext}}$ is in a one-to-one relation with the ground-state electronic density of the system, i.e. that there is only one possible ground-state density $n_0(\mathbf{r})$ for each external potential, and only one external potential that has $n_0(\mathbf{r})$ as its ground-state density[1]. This important result was not formally demonstrated in the original HK formulation of DFT; it was included a few years later in the constrained-search formulation by Levy [46, 45]. More specifically, not every possible positive-definite $N$-normalized function can be the ground state density of an Hamiltonian; nevertheless, the conditions it has to meet are simple and very generic[2].

In general the electronic density is defined in the following way:

$$\begin{aligned}
n(\mathbf{r}) &= N\int \mathrm{d}\mathbf{r}_2 \cdots \int \mathrm{d}\mathbf{r}_N \left|\Psi(\mathbf{r},\mathbf{r}_2,...,\mathbf{r}_N)\right|^2\\
&= \left\langle \Psi(\{\mathbf{r}\}) \left| \sum_{i=1,N} \delta(\mathbf{r}-\mathbf{r}_i) \right| \Psi(\{\mathbf{r}\}) \right\rangle && (2.8)
\end{aligned}$$

The external potential and the number of electrons in the system are sufficient to define the Hamiltonian uniquely, hence, as it can be derived from the Hamiltonian, also the many-body wavefunction is determined by the charge density. Finally, the total energy of the system can be computed directly from the density (i.e. without passing through the wavefunctions) with the following formula:

$$E[n] = F[n] + \int \mathrm{d}^3 r\, V_{\text{ext}}(\mathbf{r}) n(\mathbf{r}) + E_{II} \qquad (2.9)$$

[1] in this regard, two external potentials $V_{\text{ext}}$ and $V'_{\text{ext}}$ are considered *equivalent* if $V_{\text{ext}}(\mathbf{r}) - V'_{\text{ext}}(\mathbf{r}) = \text{const}$, which is consistent with the fact that an absolute energy scale has no meaning for an isolated physical system; although some choices of the zero energy are more convenient than others.

[2] Specifically, the density must be derivable from a single Slater determinant of non-interacting ground state eigenfunctions.

where $F[n] = T[n] + E_{\text{int}}[n]$ and $T[n]$ is the kinetic energy functional while $E_{\text{int}}[n]$ is the energy of electron-electron interaction; $E_{II}$ is the ion-ion interaction, which can be treated classically.

The ground-state energy is, by definition, the minimum possible energy for a quantum system. Hence, once the functional form is established, the density can be found variationally by minimizing $E[n]$.

The practice is not so straight-forward: even if the existence of functionals $T$ and $E_{\text{int}}$ is guaranteed by the theorem their form is unknown and, likely, prohibitively complicated. In the next section we will see how the introduction of an auxiliary system and an approximate *local* density exchange and correlation functional can significantly simplify the problem.

### 2.2.3 Kohn-Sham Formalism and Local Density Approximation

In order to introduce the Local Density Approximation (LDA) we start from a system of independent non interacting particles defined by an auxiliary single-particle Hamiltonian:

$$\hat{H}_s = -\frac{\hbar^2}{2m}\nabla^2 + V_s(\mathbf{r}) \tag{2.10}$$

When it is populated by $N$ independent particles, the many-body wavefunction for this system will just be the Slater determinant of the first $N$ single-particle eigenstates. We note that the HK theorem also applies to a system of independent particles as it does for a system of real electrons; thus given a particle density:

$$n^0(\mathbf{r}) = \sum_{i=1}^{N} |\psi_i(\mathbf{r})| \ , \tag{2.11}$$

it is always possible to find an auxiliary potential that has $n^0(\mathbf{r})$ as its ground state density.

The idea of Kohn and Sham was to introduce an auxiliary system of independent particles, with the same ground-state density as the original many-body system. The functional $F[n]$ is then decomposed in three contributions:

$$F[n] = T_s[n] + E_H[n] + E_{\text{xc}}[n] \, , \tag{2.12}$$

where $T_s[n]$ is the non-interacting kinetic energy defined as:

$$T_s[n] = \frac{\hbar^2}{2m} \sum_{i=1}^{N} \int \mathrm{d}^3 r \, |\nabla \psi_i(\mathbf{r})|^2 \,, \tag{2.13}$$

and $E_H[n]$ is the classical Hartree electrostatic interaction energy associated to the density:

$$E_H[n] = \frac{1}{2} \int n(\mathbf{r}) \frac{e^2}{|\mathbf{r} - \mathbf{r}'|} n(\mathbf{r}') \mathrm{d}^3 r \mathrm{d}^3 r' \,. \tag{2.14}$$

and $E_{\mathrm{xc}}[n]$, *defined* by eq. 2.12 is the still-unknown exchange-correlation functional.

The assumed condition that $n$ is simultaneously the ground state of the interacting system (with external potential $V_{\mathrm{ext}}$) and of the auxiliary non-interacting system (with potential $V_{\mathrm{KS}}$) provides a link between these quantities:

$$V_{\mathrm{KS}} = V_{\mathrm{ext}} + V_H + V_{\mathrm{xc}} \,, \tag{2.15}$$

where the Hartree potential is

$$V_H(\mathbf{r}) = e^2 \int \mathrm{d}^3 r' \frac{n(\mathbf{r}')}{|\mathbf{r} - \mathbf{r}'|} \tag{2.16}$$

and the XC potential is defined by the following functional derivative:

$$V_{\mathrm{xc}} = \frac{\delta E_{\mathrm{xc}}[n]}{\delta n(\mathbf{r})} \,. \tag{2.17}$$

The reciprocal dependencies of the involved quantities is also outlined in figure 2.1:

The critical approximation of the KS scheme, is to replace the unknown $E_{\mathrm{xc}}$ functional with an approximate one, constructed in some simple case that can be computed exactly. The first approach used the homogeneous electron gas (HEG) as a template to construct the functional. In this case, the energy dependence on the density can be computed by Monte Carlo simulations or perturbative models. Furthermore, because the HEG has a constant electronic density, the functional dependency reduces to a simple function of the density. When applied to an inhomogeneous system LDA prescription is to assign to each volume element the same XC energy contributions as in the corresponding homogeneous system:

$$E_{\mathrm{xc}}^{\mathrm{LDA}}[n] = \int \mathrm{d}^3 r n(\mathbf{r}) \varepsilon_{\mathrm{xc}}^{\mathrm{HEG}}(n(\mathbf{r})) \,; \tag{2.18}$$

$$\begin{array}{ccccccc} V_{\text{ext}}(\mathbf{r}) & \overset{HK}{\Longleftarrow} & n_0(\mathbf{r}) & \overset{KS}{\Longleftrightarrow} & n_0(\mathbf{r}) & \overset{HK}{\Longrightarrow} & V_{\text{KS}}(\mathbf{r}) \\ \Downarrow & & \Uparrow & & \Uparrow & & \Downarrow \\ \Psi_i(\{\mathbf{r}\}) & \Rightarrow & \Psi_0(\{\mathbf{r}\}) & & \psi_{i=1,N}(\mathbf{r}) & \Leftarrow & \psi_i(\mathbf{r}) \end{array}$$

Figure 2.1: Schematic representation of the HK theorem: in a normal solution of the quantum-mechanical hamiltonian, the eigenstates $\psi_i$ are determined by $V_{\text{ext}}$, the ground state can easily be found among them and used to construct the ground state electronic density $n_0(\mathbf{r})$; the HK theorem closes the chain of dependencies, proving all those quantities to be equivalent representations of the system (adapted from Martin [51])

where $\varepsilon_{\text{xc}}^{\text{HEG}}(n(\mathbf{r}))$, is the XC energy density of an HEG of density $n(\mathbf{r})$. The XC potential can then be computed directly as:

$$V_{\text{xc}}(\mathbf{r}) = \varepsilon_{\text{XC}}(n(\mathbf{r})) + n(\mathbf{r}) \left.\frac{\partial \varepsilon_{\text{xc}}(n)}{\partial n}\right|_{n=n(\mathbf{r})} . \tag{2.19}$$

Before leaving the details of the local density to the following section, we recap the form of KS electronic Hamiltonian in the LDA:

$$H_{\text{KS}} = -\frac{\hbar^2}{2m}\nabla^2 + V_{\text{ext}}(\mathbf{r}) + V_{\text{H}}(\mathbf{r}) + V_{\text{XC}}(\mathbf{r})\,; \tag{2.20}$$

where $V_{\text{ext}}$ is the same as in the many-body initial problem, the Hartree potential $V_{\text{H}}$ is defined in equation 2.16 and the XC potential has just been defined. Inside the scope of the LDA, this Hamiltonian for non-interacting electrons, has the same ground state density as the original Hamiltonian. Because the H and XC potential depend on the density, which is itself computed from the wavefunction, the problem is non-linear: the solution can be searched in a self-consistent way.

### 2.2.4 Choice of Approximate XC Density Functionals

Since the sixties, many different functional forms have been proposed for the XC energy. Historically LDA , the first one proposed by Kohn and Sham, reused some previous works from Slater [76] for the exchange part, and a parametrization of the homogeneous electron

gas for the correlation. About 15 years later, the availability of accurate Quantum Monte Carlo data for the homogeneous electron gas, from Ceperley and Alder [13], allowed Perdew and Zunger [63] and Vosko, Wilk and Nusair [81] to improve the functional significantly, also keeping into account spin-polarizability.

Another significant improvement of the functional came in 1991 with a work by Perdew and Wang [65]. The new functional form they introduced depends not only on the local value of the density, but also on its gradient; the resulting approximations are called Generalized Gradient Approximation (GGA). GGA succeeds in improving several of the LDA shortcoming, such as the large over-binding of molecules. A later improvement of the PW91 functional, called PBE from the name of its authors (Perdew, Burke and Ernzerhof [64]) is nowadays one of the most commonly used GGA's, especially in the Condensed Matter community.

For this work we have used the PBE functional, as it combines accuracy and reliability. Nevertheless, it is worth mentioning one of its main shortcoming. PBE does not reproduce van der Waals interactions correctly, missing completely long range effect; this problem is common to every local and semi-local density functional and can only be improved by very computationally expensive non local functionals, such as the one recently proposed by Dion et. al. [23], or adding empirical or semi-empirical long range corrections.

## 2.3 Projector-Augmented Waves Method

The first formulation of the Projector-Augmented Waves method (PAW) has been proposed by Blöchl in 1994 [61]; the original article showed an elegant way to generalize the old concepts of linearly-augmented plane wave method (LAPW [4]). Furthermore advantages of LAPW method were somehow merged with the concept of Ultrasoft pseudopotential, which had been introduced a few years before [79].

In our implementation of the PAW method in the Quantum-ESPRESSO [28] distribution we have mostly followed a subsequent revision of PAW formalism, proposed by Kresse and

Joubert in 1999 [42]. For a full explanation of the method we refer to the original articles, here we will only give a short summary to outline the main features and recall the notation.

### 2.3.1 PAW formalism

The PAW method is based on the assumption that the all-electron one-particle wavefunctions can be reconstructed from the pseudo wavefunctions. A linear mapping that transforms the pseudo-wavefunctions into the all-electron ones is defined as following:

$$|\psi_\nu\rangle = |\tilde{\psi}_\nu\rangle + \sum_i (|\phi_i\rangle - |\tilde{\phi}_i\rangle)\langle\tilde{p}_i|\tilde{\psi}_\nu\rangle. \tag{2.21}$$

Namely, for each valence pseudo wavefunction, $\tilde{\psi}_\nu$, where $\nu$ is the band index, you can reconstruct the all-electron wavefunction $\psi_\nu$ by adding a linear combination of one-center corrections $\phi_i - \tilde{\phi}_i$. Wavefunctions $\phi_i$ are all-electron wavefunctions from the atomic calculation, while $\tilde{\phi}_i$ are the corresponding pseudo wavefunctions.

The functions $\tilde{p}_i$ are projectors functions, that only need to respect an orthonormality condition to the wavefunctions:

$$\langle\tilde{p}_i|\tilde{\phi}_j\rangle = \delta_{i,j}. \tag{2.22}$$

The index $i$ is composite and runs over all the ionic sites $\mathbf{R}_I$, over the angular momenta $\{l_j, m_j\}$ of the atomic valence wavefunctions and over the multiple reference energies $\varepsilon_k$, which can be defined for each angular momentum. Because the projector functions are localized inside a small region surrounding each atom their orthogonality between different atoms is not enforced but only assumed; this is usually a very good approximation but can give rise to some problem, when projectors from different atoms overlap, as we will see in section 2.5.3.

Pseudo atomic wavefunctions are constructed as in the ultrasoft pseudopotential method: they are equal to all-electron ones beyond a certain cutoff radius which can be chosen arbitrarily, usually somewhere between the ionic and the covalent radius of the element. The region inside the cutoff radius is usually referred as augmentation sphere. Norm conservation condition can be imposed to the wavefunctions, but is not necessary.

The linear mapping operator can be defined in the following way:

$$\mathcal{T} = 1 + \sum_i (|\phi_i\rangle - |\tilde{\phi}_i\rangle) \langle \tilde{p}_i| \,. \tag{2.23}$$

It allows us to remap any all-electron operator, $A$, to the corresponding pseudo operator, $\tilde{A}$, acting on the pseduo-wavefunctions:

$$\begin{aligned} \tilde{A} &= \mathcal{T}^\dagger A \mathcal{T} \\ &= A + \sum_{i,j} |\tilde{p}_i\rangle \left( \langle \phi_i | A | \phi_j \rangle - \langle \tilde{\phi}_i | A | \tilde{\phi}_j \rangle \right) \langle \tilde{p}_j | + \Delta A \end{aligned} \tag{2.24}$$

Where the term $\Delta A$ is defined as:

$$\begin{aligned} \Delta A = \sum_i \Bigg\{ & |\tilde{p}_i\rangle (\langle \phi_i| - \langle \tilde{\phi}_i|) A \left( 1 - \sum_j |\tilde{\phi}_j\rangle \langle \tilde{p}_j| \right) \\ & + \left( 1 - \sum_j |\tilde{p}_j\rangle \langle \tilde{\phi}_j| \right) A \left( |\phi_i\rangle - |\tilde{\phi}_i\rangle \right) \langle \tilde{p}_j| \Bigg\} \end{aligned} \tag{2.25}$$

In order to derive equation 2.24 we have exploited the fact that $\phi_i$ and $\tilde{\phi}_i$ are equal outside the augmentation region; furthermore we have assumed that the pseudo wavefunction can be expanded as a sum of pseudo atomic orbitals inside the augmentation spheres:

$$|\tilde{\psi}_\nu\rangle = \sum_i |\tilde{\phi}_i\rangle \langle \tilde{p}_i | \tilde{\psi}_\nu \rangle. \tag{2.26}$$

The motivation for transforming the operators, instead of reconstructing the all-electron wavefunction, is to keep the treatment of pseudo wavefunction $\tilde{\psi}_\nu$, which has a "soft" plane-wave expansion, and the one-center all-electron orbital $\phi_i$, which is usually "hard" to expand, separated.

The only term that contains mixed one-center and plane wave terms is $\Delta A$; it can be shown to vanish when the operator is local or quasi-local, like for the exchange and correlation or the kinetic energy terms. The only practical case when $\Delta A$ is non-zero is the Hartree energy operator; we will see later a convenient way to treat this case, but before going into detail we have to calculate an expression for the charge density.

Density is defined as the sum over partially occupied bands of all-electron wave functions modulo squared, times the occupation $f_\nu$. Occupation is usually 1 or zero for insulators, but can have a fractional value when using tetrahedral [10] or smearing occupations in metals [54, 52]:

$$\begin{aligned} n(\mathbf{r}) &= \sum_\nu f_\nu \langle\psi_\nu|\mathbf{r}\rangle\langle\mathbf{r}|\psi_\nu\rangle \\ &= \tilde{n}(\mathbf{r}) + n^1(\mathbf{r}) - \tilde{n}^1(\mathbf{r}) \end{aligned} \tag{2.27}$$

To derive the second equivalence we have used equation 2.24 to decompose the density in three terms:

$$\tilde{n}(\mathbf{r}) = \sum_\nu f_\nu \langle\tilde{\psi}_\nu|\mathbf{r}\rangle\langle\mathbf{r}|\tilde{\psi}_\nu\rangle \tag{2.28}$$

$$\tilde{n}^1(\mathbf{r}) = \sum_{\nu,(i,j)} f_\nu \langle\tilde{\psi}_\nu|\tilde{p}_i\rangle\langle\tilde{\phi}_i|\mathbf{r}\rangle\langle\mathbf{r}|\tilde{\phi}_j\rangle\langle\tilde{p}_j|\tilde{\psi}_\nu\rangle \tag{2.29}$$

$$n^1(\mathbf{r}) = \sum_{\nu,(i,j)} f_\nu \langle\tilde{\psi}_\nu|\tilde{p}_i\rangle\langle\phi_i|\mathbf{r}\rangle\langle\mathbf{r}|\phi_j\rangle\langle\tilde{p}_j|\tilde{\psi}_\nu\rangle \tag{2.30}$$

The term $\tilde{n}$ is constructed from the self-consistent wavefunctions $|\tilde{\psi}\rangle$, the $\tilde{n}^1$ and $n^1$ terms are one-center densities constructed from the pseudo and all-electron atomic wavefunctions respectively. The advantage of this decomposition is that the $\tilde{n}$ term can be expanded in plane-waves up to a low cutoff while the hard $n^1$ term can be stored on radial support grids, localized inside the cutoff radius of each atom.

### 2.3.2 Total Energy in the PAW Formalism

The total energy, as a functional of the all-electron variational density, is expressed in the following way:

$$E = \sum_\nu f_\nu \langle\psi_\nu| - \frac{1}{2}\nabla^2 |\psi_\nu\rangle + \tag{2.31}$$

$$+\frac{1}{2}\int \mathrm{d}r \int \mathrm{d}r\,' \frac{n(r)n(r')}{|r-r'|} + \int \mathrm{d}r\, n\, \varepsilon_{\mathrm{xc}}(n). \tag{2.32}$$

Each contribution can be separated in a plane-wave based pseudo part and two one-center based parts. In analogy to what happens for the density, the one-center pseudo part cancels

the contributions of the plane-wave part inside the augmentation spheres; then the exact all-electron one-center contribution is added.

For the complete procedure we refer to the original article by Blöchl, [61] we will only remark here a few points. The exchange-correlation energy is invariant with respect to the addition of an arbitrary density to both $\tilde{n}^1$ and $\tilde{n}$. A first consequence of this fact is that we can use an arbitrary non-linear core correction, or no core correction at all; in practice we have used a very soft core correction which improves the behaviour of gradient-corrected functional close to the ion nuclei.

The second and more important consequence is that the augmentation charge doesn't have to emulate the all-electron density, as it does in the ultrasoft scheme: it only needs to be chosen in a way that cancels long-range electrostatic interaction between augmentation spheres in the $\tilde{n}$ component. This condition is satisfied imposing:

$$\int_{\Omega_{\mathbf{R}}} \mathrm{d}r \, \left(n^1(r) - \tilde{n}^1(r) - \hat{n}(r)\right) |\mathbf{r} - \mathbf{R}|^L Y_{LM}(\mathbf{r} - \hat{} \, \mathbf{R}) = 0, \tag{2.33}$$

where $\hat{n}$ is the augmentation charge. In other words: the total electrostatic multipoles of the all-electron one center terms must be equal to the ones of the pseudo one-center terms, augmentation charge included.

The final one-center contribution to the total energy is composed of an all-electron part and a pseudo part: $\Delta E^1 = E^1 - \tilde{E}^1$; the explicit expressions follow:

$$\begin{aligned} E^1 &= \sum_{ij} \tilde{\rho}_{ij} \langle \phi_i | -\frac{1}{2}\nabla^2 | \phi_j \rangle \\ &\quad + E_H[n^1] + E_{\mathrm{xc}}[n^1 + n_c^1] \end{aligned} \tag{2.34}$$

$$\begin{aligned} \tilde{E}^1 &= \sum_{ij} \tilde{\rho}_{ij} \langle \tilde{\phi}_i | -\frac{1}{2}\nabla^2 | \tilde{\phi}_j \rangle \\ &\quad + E_H[\tilde{n}^1 + \hat{n}] + E_{\mathrm{xc}}[n^1 + \tilde{n}_c^1 + \hat{n}] \end{aligned} \tag{2.35}$$

Where $n_c$ and $\tilde{n}_c$ are respectively the all-electron and pseudo core charges densities, and we have defined the cross channel occupation $\tilde{\rho}_{ij}$:

$$\tilde{\rho}_{ij} = \sum_{\nu} f_\nu \langle \tilde{\psi}_\nu | \tilde{p}_i \rangle \langle \tilde{p}_j | \tilde{\psi}_\nu \rangle. \tag{2.36}$$

### 2.3.3 Generalized Hamiltonian Operator

The hamiltonian operator can be computed in analogy to the ultrasoft case, we have followed the derivation by Kresse and Joubert [42], which is considerably simpler that the first formulation by Bloechl. The only part which differs from the ultrasoft pseudopotential formalism is the derivative of the energy with respect to the augmentation channel occupations $\tilde{\rho}_{ij}$.

The final espression is composed of an all-electron and a pseudo term, which can be computed on the radial support grid:

$$D_{ij} = \int \mathrm{d}r\, q^1_{ij}(r) v^1_{\mathrm{eff}}(r) \tag{2.37}$$

$$\tilde{D}_{ij} = \int \mathrm{d}r\, \left(\tilde{q}^1_{ij}(r) + \hat{q}_{ij}(r)\right) \tilde{v}^1_{\mathrm{eff}}(r) \tag{2.38}$$

With $q_{ij}(r) = \phi_i(r)\phi_j(r)$ and $\tilde{q}_{ij}(r) = \tilde{\phi}_i(r)\tilde{\phi}_j(r)$, the terms $\hat{q}_{ij}(r)$ are the components of the augmentation charge that cancel the electrostatic multipoles of $q_{ij} - \tilde{q}_{ij}$; finally the effective potentials $v^1_{\mathrm{eff}}$ and $\tilde{v}^1_{\mathrm{eff}}$ are defined as:

$$v^1_{\mathrm{eff}} = v_{\mathrm{xc}}[n^1 + n^1_c] + v_H[n^1] \tag{2.39}$$

$$\tilde{v}^1_{\mathrm{eff}} = v_{\mathrm{xc}}[\tilde{n}^1 + \tilde{n}^1_c + \hat{n}] + v_H[\tilde{n}^1 + \hat{n}]\,. \tag{2.40}$$

In addition to these two terms there are some terms which do not involve the effective potential: they can be computed once and for all during the dataset generation. The first term of this kind is the kinetic energy difference:

$$\Delta K_{ij} = \langle\phi_i| - \frac{1}{2}\nabla^2 |\phi_j\rangle - \langle\tilde{\phi}_i| - \frac{1}{2}\nabla^2 |\tilde{\phi}_j\rangle\ . \tag{2.41}$$

The second term is the effect of the local potential on the atomic wavefunctions:

$$D^0_{ij} = \int \mathrm{d}r\, q^1_{ij}(r) v^1_{\mathrm{loc}}(r) - \int \mathrm{d}r\, \left(\tilde{q}^1_{ij}(r) + \hat{q}_{ij}(r)\right) \tilde{v}^1_{\mathrm{loc}}(r)\,, \tag{2.42}$$

where $v_{\mathrm{loc}}$ and $\tilde{v}_{loc}$ are the all-electron and pseudo local potentials.

The final expression for the hamiltonian is very similar to the ultrasoft case:

$$H = -\frac{1}{2}\nabla^2 + \tilde{v}_{\text{eff}} \tag{2.43}$$

$$+\sum_{ij} |\tilde{p}_i\rangle \left(\Delta K_{ij} + D^0_{ij} + D_{ij} - \tilde{D}_{ij}\right) \langle \tilde{p}_j| \,. \tag{2.44}$$

The main difference resides in the correction terms $D_{ij} - \tilde{D}_{ij}$, which are updated self-consistently and do not have a counterpart in the ultrasoft scheme.

### 2.3.4 PAW Implementation

The PAW method can be implemented on top of a plane-wave code, which uses ultrasoft pseudopotentials, in a relatively straightforward way. It is easy to notice that the one-center parts of the PAW formalism depends on the plane wave calculation only via the augmentation channel occupations $\tilde{\rho}_{ij}$ from equation 2.36.

On the other hand, the plane-wave calculation feels the effect of the one-center terms via the hamiltonian corrections from the equations 2.37 and 2.38. The other main contribution comes from the energy correction of equations 2.34 and 2.35.

The third, more subtle, effect is mediated by the generalized Broyden mixing procedure [38, 37] we have used; in the mixing procedure it is necessary to compute the electrostatic response of the total density difference on subsequent iterations:

$$\beta_{ab} = \int \mathrm{d}r \, v_H[\delta n_a]\delta n_b(r) \tag{2.45}$$

where $\delta n_a$ is the difference of the charge density between the last iteration and $a$ iterations before. In order to guarantee a smooth convergence, this term must include the appropriate PAW corrections. It is also important to note that $\tilde{\rho}_{ij}$ have to be mixed in the same way as the plane-wave density to keep the whole system consistent. In general we have noticed that the cross band occupations can, and should, be treated exactly in the same way as the usual plane-wave charge density term.

### 2.3.5 One center integrals

When calculating the one-center terms we have to keep the usage of computational resources affordable, and the accuracy high; in order to meet both targets the one-center fields have been expressed as a sum of spherical harmonics whenever possible. In practice this is exactly possible only for the Hartree potential, as it only requires the spherical harmonic expansion of $1/|r - r'|$, which is given by the well known formula:

$$V_h(r) = \sum_{lm} Y_{lm}(\hat{r}) \frac{1}{2l+1} \int \mathrm{d}r' 4\pi r'^2 n^{lm}(r') \frac{r_<^l}{r_>^{l+1}} \tag{2.46}$$

Where $r_> = \max(r, r')$ and $r_< = \min(r, r')$; while $n_{lm}(r)$ is the radial part of the $Y_{lm}$ component of the total one-center density, it may be all-electron or pseudo and, in the latter case, it includes augmentation charge as well. It is always possible to compute the $lm$ components of density starting from the $q_{ij}$ functions and using the sum of angular momentum theorem.

On the other hand, there is a potential difficulty for the exchange-correlation energy, as it is non-linear and, in general, it does not have a simple analytic expression. In this case the one-center integral have to be computed on a certain number of radial directions. In order to find a good expression, we observe that the generic spherical harmonic $Y_{lm}(\theta, \varphi)$ is defined in terms of a $\phi$-dependent phase factor and an associated Legendre polynomial of degree $l$ in $z/r = \cos\theta$. We have therefore used Gaussian quadrature [5] to integrate along the $\theta$ angle.

The dependence of $Y_{lm}(\theta, \varphi)$ on $\varphi$ is simply $\sim \exp(-im\varphi)$: to integrate exactly with respect to the azimuth angle it is sufficient to take $l + 1$ evenly spaced samples, multiplied by the constant weight $2\pi/(l + 1)$.

What remains to be settled is the minimum value of $l$ up to which the integrals have to be calculated in order to provides sufficient accuracy. First of all we observe that if the wavefunction includes components that go up to a certain angular momentum, the atomic charge-density expansion can go up to twice that value. The Hartree potential is diagonal

on a basis of spherical harmonic, thus no additional components are required to expand it properly.

On the other hand, the exchange-correlation functional, being strongly non-linear, can in principle have non-negligible components up to a much higher value of $l$; yet the higher components will not contribute to the total energy: as the XC energy is expressed as $\int \mathrm{d}r\, n(r)\varepsilon_{\mathrm{xc}}(n(r))$, the components that are present is $\varepsilon_{\mathrm{xc}}$ but not in $n$ will cancel out in the integral because of orthonormality of spherical harmonics. Nevertheless, as the integral is computed numerically on a finite angular grid higher components can introduce some aliasing error if not integrated correctly. We have found the convergence to be slower for gradient-corrected functionals than for LDA. As a default we have chosen to set the integration parameters in a way that guarantees an exact integration up to $6l_{\max}$ for LDA and $6l_{\max}+2$ for GGA, where $l_{\max}$ is the maximum angular momentum present among the valence wavefunctions.

The integration precision depends on the specific valence configuration of each ions, thus each atomic species is treated separately. Finally, as an important exception, ions that only have $s$ wavefunctions in valence can be integrated exactly with a single radial sampling; in these category we have Hydrogen, Helium and possibly alkali and alkaline earth metal, although for them some additional semi-core wavefunctions are often included in valence,

### 2.3.6 Spherical coordinates derivatives

In order to compute gradient-corrected density functionals, and the corresponding XC potential we had to implement two algorithms to efficiently compute the gradient of a scalar field, and the divergence of a vector field, in spherical coordinates.

Our solution is to expand the field on a basis of spherical harmonics: the charge density is already in this form, while the XC energy has to be converted from a number of radial samples. Then we use the spherical coordinates expression for the operator; in this way we can use the precomputed expression for the derivative of $Y_{lm}$ along the $\theta$ and $\phi$ versors, while only the radial derivative of each component has to be computed numerically.

Finally, as the gradient of a scalar field is a three-dimensional vector, we can use any convenient coordinate system to express it; in our case we found convenient to use radial ($\hat{r}$), azimuthal ($\hat{\theta}$) and inclination ($\hat{\varphi}$) directions.

## 2.4 Computational Tests

### 2.4.1 PAW Datasets and Pseudopotentials

The purpose of our tests has been to verify the accuracy of our PAW implementation, and to estimate how much results can be improved by using the PAW method instead of the ultrasoft pseudopotential method in plane-wave calculations. For this reason we have generated, for each element, two PAW datasets and two ultrasoft pseudopotentials with the following characteristics:

- a very "hard" PAW dataset, designed to reproduce accurately the all electron energy;
- a very "hard" ultrasoft pseudopotential, based on the same radii as the PAW dataset above;
- another PAW dataset soft enough to allow the convergence of total energy within one mRy at a plane-wave cutoff of no more than 30 Ry (about 400 eV);
- an ultrasoft pseudopotential with the same radii as the PAW dataset.

We have used the same pseudization strategy when generating the ultrasoft and PAW wavefunctions, hence using the same cutoff radii guarantees the same projector operators and the same convergence with respect to the plane-wave expansion. The radii used are reported in table 2.1. In the tables we have also reported the minimum kinetic-energy cutoff $E_{cut}$, required to converge the total energy to an accuracy of 1 mRy. In practice and to simplify the comparisons, we have always used $E_{cut} = 70$ Ry for the hard setups and 30 Ry for the soft ones.

Table 2.1: Cutoff radii used to generate "hard" (a) and "soft" (b) PAW datasets and US pseudopotentials. The columns refer to the radius used for the s channel, the p channel and the channel used to generate the local potential. In the last column is report the convergence cutoff in Ry.

(a) "hard"

| el. | $r_c^s$ | $r_c^p$ | $r_c^{loc}$ | loc. | $e_{cut}$ |
|---|---|---|---|---|---|
| H | 0.80 | - | 0.80 | p | 60. |
| Li | 1.30 | - | 1.30 | p | 60. |
| Be | 1.60 | 1.60 | 1.60 | d | 14. |
| C | 1.10 | 1.10 | 0.95 | d | 70. |
| N | 1.10 | 1.15 | 0.95 | d | 70. |
| O | 1.10 | 1.10 | 0.95 | d | 70. |
| F | 1.10 | 1.10 | 0.90 | d | 70. |
| Na | 2.30 | 2.30 | 1.65 | d | 24. |
| Si | 1.80 | 1.80 | 1.65 | d | 12. |
| P | 1.50 | 1.50 | 1.40 | d | 60. |
| S | 1.50 | 1.50 | 1.45 | d | 35. |
| Cl | 1.30 | 1.30 | 1.15 | d | 60. |

(b) "soft"

| el. | $r_c^s$ | $r_c^p$ | $r_c^{loc}$ | loc. | $e_{cut}$ |
|---|---|---|---|---|---|
| H | 1.00 | - | 0.75 | p | 30. |
| Li | 1.80/2.10 | - | 1.65 | p | 24. |
| Be | 1.60 | 1.60 | 1.60 | d | 14. |
| C | 1.30 | 1.45 | 1.10 | d | 30. |
| N | 1.30 | 1.45 | 1.10 | d | 30. |
| O | 1.35 | 1.55 | 1.30 | d | 30. |
| F | 1.45 | 1.60 | 1.30 | d | 30. |
| Na | 2.30 | 2.30 | 1.65 | d | 24. |
| Si | 1.80 | 1.80 | 1.65 | d | 12. |
| P | 1.60 | 1.60 | 1.55 | d | 30. |
| S | 1.60 | 1.60 | 1.60 | d | 28. |
| Cl | 1.60 | 1.80 | 1.60 | d | 26. |

On the other hand the augmentation charge in the PAW method can be pseudized more aggressively than in the US case; hence the cutoff required for the charge density can be considerably lower. In performing our tests we have used the minimum cutoff for PAW calculations: $E_{cut}^{\rho} = 4E_{cut}^{wfc}$. For the hard ultrasoft pseudopotentials we have used $8E_{cut}^{wfc}$, while for the softer USPP we have chosen to increase the charge-density cutoff further up to $10E_{cut}^{wfc}$ in order to ensure proper convergence.

### 2.4.2 Small Molecules

In order to check the accuracy of our PAW implementation we have tested it on the G2-1 molecular test set. [19] This set comprises about 50 small molecules containing atoms from the first and second rows of the periodic table. For each molecule the experimental binding energy is available in literature, together with several computational estimates: all-

electron DFT on a Gaussian basis set, plane-wave pseudopotential DFT, all-electron PAW and accurate quantum-chemistry.

Isolated systems have to be placed in a periodic cell large enough to prevent any significant interaction between fictitious periodic images. After testing the more problematic examples (the molecule which we expect to have larger dipole) we have decided to use a face-centered cubic (FCC) cell of about 300 $Å^3$ volume. We have decided not to include any correction for interaction with fictitious periodic images [9] as this effect was negligible on the final configuration.

Most of the molecules considered are well behaved and could be converged to the structural optimum without any special care. As stated in section 2.4.1, we have used a kinetic-energy cutoff of 30 Ry for the "soft" datasets and of 70 Ry for the "hard ones", which we found to be sufficient to converge all the systems within 1 mRy (about 13.6 meV or 0.31 kcal/mol).

The results are summarized in table 2.2 (next pages); as a reference we have used the all-electron Gaussian calculations performed by Paier et. al. [57]. All the binding energies are expressed in kcal/mol. As it can be seen the precision of ultrasoft calculation do not improve considerably moving from "soft" to "hard" setups. On the other hand "soft" PAW datasets perform at least as good as "soft" ultrasoft, in many cases outperforming them clearly. Furthermore when switching to the "hard" PAW datasets we can reach an accuracy always comparable to the all-electron calculations performed with well-converged Gaussian basis sets.

Table 2.2: Total binding energy in kcal/mol for two PAW and two US datasets, and all-electron reference. The all-electron DFT energies are from ref. [57], except the $H_2$ one, which has been computed by us using a "$1/r$" all-electron potential on plane-wave basis set at a kinetic-energy cutoff of 400 Ry.

| Molecule | PAW hard | Δ | PAW soft | Δ | AE | US hard | Δ | US soft | Δ |
|---|---|---|---|---|---|---|---|---|---|
| $H_2$ | 104.6 | (0.1) | 104.2 | (-0.4) | 104.5 | 104.6 | (0.1) | 104.2 | (-0.4) |
| LiH | 52.1 | (-1.4) | 50.9 | (-2.6) | 53.5 | 52.1 | (-1.4) | 51.5 | (-2.0) |
| BeH | 55.5 | (-0.1) | 55.4 | (-0.2) | 55.6 | 56.9 | (1.3) | 56.8 | (1.2) |
| CH | 84.9 | (0.1) | 84.7 | (-0.1) | 84.8 | 83.7 | (-1.1) | 83.3 | (-1.5) |
| $CH_2$ $^1A_1$ | 179.2 | (0.1) | 178.7 | (-0.4) | 179.1 | 177.1 | (-2.0) | 176.5 | (-2.6) |
| $CH_2$ $^3B_1$ | 194.7 | (0.1) | 194.2 | (-0.4) | 194.6 | 194.0 | (-0.6) | 193.6 | (-1.1) |
| $CH_3$ | 310.1 | (-0.0) | 309.3 | (-0.8) | 310.1 | 308.3 | (-1.8) | 307.5 | (-2.6) |
| $CH_4$ | 420.0 | (-0.2) | 419.2 | (-1.0) | 420.2 | 417.5 | (-2.7) | 416.7 | (-3.5) |
| NH | 88.8 | (0.2) | 88.4 | (-0.2) | 88.6 | 86.8 | (-1.8) | 86.0 | (-2.6) |
| $NH_2$ | 189.0 | (0.1) | 188.1 | (-0.8) | 188.9 | 185.2 | (-3.8) | 183.9 | (-5.0) |
| $NH_3$ | 302.0 | (-0.3) | 300.9 | (-1.4) | 302.3 | 296.9 | (-5.4) | 295.7 | (-6.6) |
| OH | 110.1 | (-0.0) | 109.0 | (-1.1) | 110.1 | 106.8 | (-3.4) | 105.9 | (-4.2) |
| $H_2O$ | 234.4 | (-0.1) | 232.6 | (-1.9) | 234.5 | 228.6 | (-5.9) | 227.5 | (-7.0) |
| HF | 142.1 | (-0.1) | 139.6 | (-2.6) | 142.2 | 140.3 | (-1.9) | 138.4 | (-3.8) |
| $SiH_2$ $^1A_1$ | 148.2 | (0.2) | 147.9 | (-0.1) | 148.0 | 148.2 | (0.2) | 148.0 | (0.0) |
| $SiH_2$ $^3B_1$ | 131.9 | (0.1) | 131.7 | (-0.1) | 131.8 | 131.9 | (0.1) | 131.7 | (-0.1) |
| $SiH_3$ | 222.8 | (0.2) | 222.4 | (-0.2) | 222.6 | 222.7 | (0.1) | 222.4 | (-0.2) |
| $SiH_4$ | 314.0 | (0.3) | 313.4 | (-0.3) | 313.7 | 313.9 | (0.2) | 313.4 | (-0.3) |
| $PH_2$ | 154.8 | (0.2) | 154.3 | (-0.3) | 154.6 | 154.5 | (-0.1) | 154.2 | (-0.4) |
| $PH_3$ | 239.6 | (0.2) | 238.8 | (-0.5) | 239.3 | 239.2 | (-0.1) | 238.7 | (-0.6) |
| $SH_2$ | 182.5 | (0.3) | 182.0 | (-0.2) | 182.2 | 182.1 | (-0.1) | 181.6 | (-0.6) |
| HCl | 106.6 | (0.1) | 106.4 | (-0.1) | 106.5 | 106.4 | (-0.1) | 106.1 | (-0.4) |
| $Li_2$ | 17.8 | (-2.3) | 18.7 | (-1.4) | 20.1 | 17.8 | (-2.3) | 17.8 | (-2.3) |
| LiF | 137.6 | (-1.4) | 136.1 | (-2.9) | 139.0 | 135.9 | (-3.1) | 136.5 | (-2.5) |
| $C_2H_2$ | 415.1 | (0.0) | 413.9 | (-1.2) | 415.1 | 410.0 | (-5.1) | 409.1 | (-6.0) |
| $C_2H_4$ | 571.8 | (-0.1) | 570.4 | (-1.5) | 571.9 | 566.7 | (-5.2) | 565.5 | (-6.4) |

Table continues on next page

Table continues from previous page

| Molecule | PAW hard | Δ | PAW soft | Δ | AE | US hard | Δ | US soft | Δ |
|---|---|---|---|---|---|---|---|---|---|
| $C_2H_6$ | 716.9 | (-0.2) | 715.1 | (-2.0) | 717.1 | 711.8 | (-5.3) | 710.1 | (-7.0) |
| CN | 197.7 | (0.0) | 196.9 | (-0.8) | 197.7 | 190.6 | (-7.1) | 189.8 | (-7.9) |
| HCN | 326.9 | (0.4) | 325.3 | (-1.2) | 326.5 | 319.1 | (-7.4) | 317.8 | (-8.7) |
| CO | 268.9 | (-0.2) | 265.5 | (-3.6) | 269.1 | 260.6 | (-8.5) | 258.3 | (-10.8) |
| HCO | 295.4 | (-0.1) | 292.8 | (-2.7) | 295.5 | 287.4 | (-8.1) | 286.0 | (-9.5) |
| $H_2CO$ | 386.3 | (-0.0) | 383.9 | (-2.4) | 386.3 | 378.0 | (-8.3) | 376.9 | (-9.4) |
| $CH_3OH$ | 520.2 | (-0.2) | 518.4 | (-2.0) | 520.4 | 511.9 | (-8.5) | 511.0 | (-9.4) |
| $N_2$ | 243.8 | (-0.1) | 241.1 | (-2.8) | 243.9 | 233.3 | (-10.6) | 230.7 | (-13.2) |
| $N_2H_4$ | 453.2 | (-0.5) | 451.5 | (-2.2) | 453.7 | 442.9 | (-10.8) | 441.1 | (-12.7) |
| NO | 172.2 | (-0.3) | 168.7 | (-3.8) | 172.5 | 161.9 | (-10.6) | 159.5 | (-13.0) |
| $O_2$ | 143.6 | (-0.4) | 140.3 | (-3.7) | 144.0 | 133.9 | (-10.1) | 132.8 | (-11.2) |
| $H_2O_2$ | 282.3 | (-0.3) | 280.1 | (-2.5) | 282.6 | 270.9 | (-11.7) | 270.5 | (-12.1) |
| $F_2$ | 52.8 | (-0.2) | 51.5 | (-1.5) | 53.0 | 49.5 | (-3.5) | 50.4 | (-2.6) |
| $CO_2$ | 416.1 | (-0.4) | 410.3 | (-6.2) | 416.5 | 401.8 | (-14.7) | 399.0 | (-17.5) |
| $Na_2$ | 19.0 | (0.9) | 17.7 | (-0.4) | 18.1 | 19.1 | (1.0) | 18.9 | (0.8) |
| $Si_2$ | 82.5 | (1.1) | 82.5 | (1.1) | 81.4 | 82.5 | (1.1) | 82.4 | (1.0) |
| $P_2$ | 122.0 | (0.3) | 121.5 | (-0.2) | 121.7 | 121.3 | (-0.4) | 121.0 | (-0.7) |
| $S_2$ | 115.8 | (0.6) | 115.0 | (-0.2) | 115.2 | 115.2 | (-0.0) | 114.4 | (-0.8) |
| $Cl_2$ | 65.9 | (0.1) | 65.3 | (-0.5) | 65.8 | 65.6 | (-0.2) | 64.7 | (-1.1) |
| NaCl | 94.7 | (0.2) | 93.9 | (-0.6) | 94.5 | 94.6 | (0.1) | 94.4 | (-0.1) |
| SiO | 197.2 | (0.6) | 196.7 | (0.1) | 196.6 | 191.3 | (-5.3) | 192.0 | (-4.6) |
| CS | 179.9 | (0.3) | 179.1 | (-0.5) | 179.6 | 176.9 | (-2.7) | 176.0 | (-3.6) |
| SO | 141.8 | (0.5) | 140.0 | (-1.3) | 141.3 | 136.2 | (-5.1) | 135.6 | (-5.7) |
| ClO | 79.8 | (-1.8) | 78.4 | (-3.1) | 81.5 | 74.2 | (-7.3) | 78.5 | (-3.0) |
| ClF | 72.4 | (-0.1) | 71.2 | (-1.3) | 72.5 | 70.6 | (-1.9) | 70.3 | (-2.2) |
| $Si_2H_6$ | 521.5 | (1.1) | 520.5 | (0.1) | 520.4 | 521.2 | (0.8) | 520.5 | (0.1) |
| $CH_3Cl$ | 400.3 | (0.1) | 399.3 | (-0.9) | 400.2 | 397.6 | (-2.6) | 396.4 | (-3.8) |
| $CH_3SH$ | 478.9 | (0.3) | 477.6 | (-1.0) | 478.6 | 476.0 | (-2.6) | 474.7 | (-3.9) |
| HOCl | 175.6 | (-0.1) | 174.0 | (-1.7) | 175.7 | 169.7 | (-6.0) | 168.9 | (-6.8) |
| $SO_2$ | 281.7 | (1.0) | 276.2 | (-4.5) | 280.7 | 269.8 | (-10.9) | 266.8 | (-13.9) |

Table 2.3: Cutoff radii used to generate the paw datasets used in solid crystals calculations. The columns have the same contents as in table 2.1.

| el. | $r_c^s$ | $r_c^p$ | $r_c^d$ | $r_c^{loc}$ | loc. | semi-core | $e_{cut}$ |
|---|---|---|---|---|---|---|---|
| N | 1.30 | 1.45 | - | 1.10 | d | no | 35. |
| Al | 1.90 | 1.90 | - | 1.75 | d | no | 20. |
| Ga | 2.40 | 2.40 | - | 2.40 | d | no | 15. |
| Ga | 2.00 | 2.00 | 2.00 | 2.00 | tm | 3d | 30. |
| In | 2.20 | 2.20 | 2.20 | 1.80 | tm | 4d | 25. |

### 2.4.3 Solids

We have further tested our implementation on a few crystalline structures. As a reference we have taken recent all-electron full-potential linearised plane-wave (FP-LAPW) calculations of group III-V semiconductor compounds: AlN, GaN and InN [20]. For each structure we have computed the ground state energy, binding energy, equilibrium lattice constant and bulk modulus in the zinc-blend structure. Furthermore we have repeated the calculations for the wurzite structure; computing also the c/a lattice parameter.

For Nitrogen atoms we have used the soft PAW dataset from section 2.4.2, whose key characteristics are reported in table 2.3. For Indium we included the $4d$ semi-core orbital in valence, while for Ga we have generated two different datasets, with and without the $3d$ semi-core states in valence. When the $d$ orbitals were not included in valence we have used the empty $d$ channel to generate the local potential; in the other cases we have generated it by smoothing the all-electron potential as described in the Troullier-Martins recipe. [78]

All the calculation have been performed with the generalized-gradient approximation PBE functional and a plane-wave cutoff of 35 Ry. A reciprocal space k-point grid of $8 \times 8 \times 8$ special points was used for zincblend and $7 \times 7 \times 4$ for wurzite, both generated according to Monkhorst and Pack recipe [55]. This choice produces grossly the same number of points per unit volume in the reciprocal cell for the two cases.

The results are collected in tables 2.4 and 2.5. For both the zincblend and the wurzite

Table 2.4: Comparison of FP-LAPW and PAW zincblend structures.

| | a (Å) | | B (MBar) | |
|---|---|---|---|---|
| | paw | lapw | paw | lapw |
| AlN | 4.404 | 4.407 | 1.96 | 1.92 |
| GaN | 4.525 | 4.556 | 1.89 | 1.74 |
| GaN (3d) | 4.556 | 4.556 | 1.68 | 1.74 |
| InN (4d) | 4.404 | 4.407 | 1.33 | 1.28 |

Table 2.5: Comparison of FP-LAPW and PAW wurzite structures. The parameter $u$ is the vertical spacing between planes of Nitrogen and the other element.

| | a (Å) | | c/a | | u | | B (MBar) | |
|---|---|---|---|---|---|---|---|---|
| | paw | lapw | paw | lapw | paw | lapw | paw | lapw |
| AlN | 3.131 | 3.121 | 1.604 | 1.622 | 0.378 | 0.378 | 1.93 | 1.89 |
| GaN | 3.203 | 3.224 | 1.627 | 1.628 | 0.376 | 0.376 | 1.90 | 1.72 |
| GaN (3d) | 3.221 | 3.224 | 1.631 | 1.628 | 0.376 | 0.376 | 1.67 | 1.72 |
| InN (4d) | 3.570 | 3.598 | 1.618 | 1.623 | 0.377 | 0.377 | 1.33 | 1.19 |

structures the PAW calculations can reproduce the full potential result with an accuracy of the order of 0.1% for geometrical parameters; the bulk moduli are reproduced with an accuracy of about 2%. Furthermore, we notice how the accuracy tends to deteriorates when the frozen-core approximation is less accurate: in GaAn and InN the semi-core $d$ orbitals of the III-column elements are resonating with the Nitrogen $p$ orbital. We can notice an improvement in accuracy when the Gallium $3d$ orbitals are treated explicitly in GaN.

## 2.5 Comments on PAW Method

### 2.5.1 Datasets Generation

An important part of a PAW calculation is the generation of the datasets; we will not go in depth on this matter, which has already been discussed thoroughly during the past decades. In general the generation of a PAW dataset is not necessarily more difficult than the generation of an ultrasoft pseudopotential. It must however be noted that, in order to reach all-electron accuracy we cannot generate the local potential by inverting a non-empty pseudized orbital. On the contrary, it is customary for ultrasoft pseudopotentials of transition metal to take the valence $s$ or $p$ orbital - let's call it the local channel - pseudize it, and generate a local potential that reproduces the pseudized orbital exactly, without needing any semi-local projector. This procedure is not allowed in the PAW formalism.

There are two benefits to this approach: the reduced number of projectors can marginally speed up the calculation, and the local channel is immune to the ghost-state problem. On the other hand the local channel has to be node-less and norm-conserving, hence it can have at most norm-conserving accuracy. Instead of using a mixed approach - that would spoil the PAW benefits - we have chosen to use only empty high-energy states to generate the local potential; or to generate it by smoothing the all-electron potential directly.

### 2.5.2 Numerical Efficiency

In general our PAW implementation is computationally very inexpensive. In all our test calculations computing the one-center terms required less than 0.1% of total CPU time; for comparison the parts of the formalism which are equally present in the ultrasoft pseudopotential method, like the projections of equation 2.36 and the summation of augmentation charge, require more than 1% of total time for molecules and up to 10% for crystals.

Moreover, on a plane-wave basis set, the computational cost of one-center terms scales linearly with number of atoms, while the SCF calculation scales with its third power, hence

computing them becomes relatively less expensive for larger system. They are also totally independent of other speed-related parameters - like the plane-wave expansion cutoff and the sampling of the Brillouin zone.

Nevertheless, even a very short computational time can become a bottle-neck on massive parallel systems; for this reason we have parallelized the one-center integrals on several levels. More specifically the first parallelization level distributes the atoms evenly along processors, it is very easy to implement using a Message Passing Interface (MPI) implementation [53] and can give a good scaling up to a few hundreds of processors. When the number of processors becomes substantially higher than the number of atoms this parallelisation scheme is no more sufficient to guarantee a proper scalability; for this reason another level of parallelization has been later introduced in the code by C. Cavazzoni of the CINECA computing centre in Bologna. This parallel distribution of tasks acts on the one-center integrals, estimating concurrently the radial part of the integrals at different azimuth and polar angles; it has been implemented using the Open Multi-Processing application programming interface (OpenMP API [14]) and is only necessary when the number of processors is several times larger than the number of atoms. A third, intermediate, level of parallelization is possible, but not yet implemented: it would parallelize on the augmentation channel, i.e. equation 2.37 would be computed simultaneously for different values of $i$ and $j$.

### 2.5.3 Absolute Accuracy

As we have already noted several times during this work, PAW can effectively reproduce all-electron calculations to a high degree of accuracy. Nevertheless there are two important limiting factors to be kept in mind that can spoil the accuracy.

The first factor is the violation of the frozen core approximation, we have observed it in section 2.4.3, where the resonance of $3d$ orbitals of Gallium with $2p$ orbitals of Nitrogen plays an important role in the chemical bonding. Treating the semi-core implicitly still produced a more than acceptable accuracy, but including it in the valence manifold improved the results.

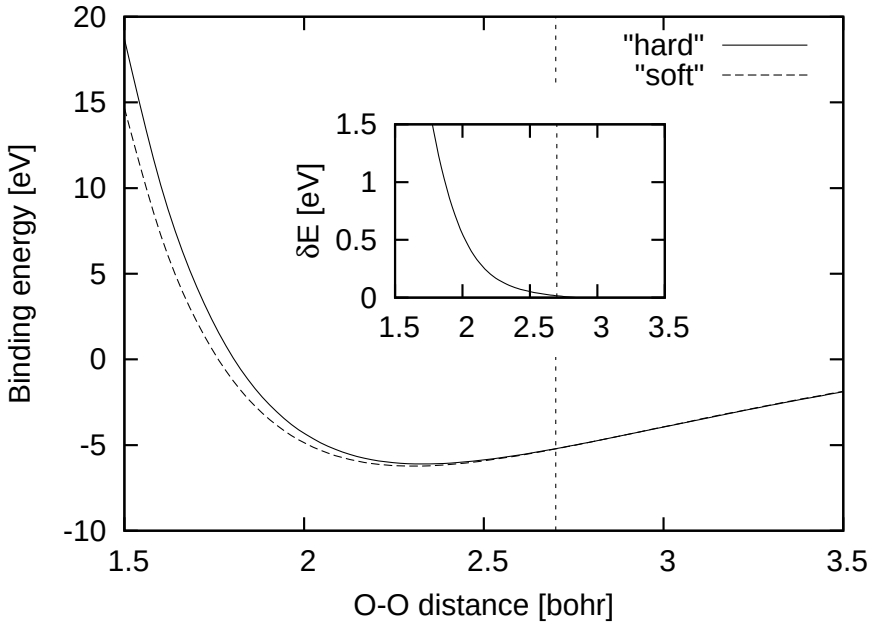


Figure 2.2: Binding energy of an $O_2$ molecule as a function of O−O distance computed using "hard" (solid line) and "soft" (dashed line) datasets. The vertical dotted line indicates the O−O distance where the projectors from different atoms stop to overlap, for the soft dataset. The inset shows the difference between the two curves.

In a more general frame, the outer orbitals of heavier elements cores have smaller binding energies than in light elements. Thus for heavy elements the inclusion of more orbitals in the valence can effectively increase the calculation accuracy of the calculation.

The second limiting factor is the double-counting error introduced when projectors overlap; in section 2.4.2 we have noticed how the accuracy of PAW can rival all-electron for hard setups, but deteriorates slightly when using softer datasets. When stating the PAW formalism we required that $\langle \tilde{p}_i | \tilde{\phi}_j \rangle = \delta_{i,j}$, where $i$ and $j$ refer to any projector or atomic component in the cell. In practice the condition is actively enforced when $i$ and $j$ belong to the same ion; while it is *assumed* to be true when they belong to different atoms. This is however not exactly true when the augmentation spheres of neighbouring atoms overlap significantly and eq. 2.21 does not hold exactly in this case.

In order to estimate the magnitude of the error, done due to projector overlap, we have

used an $O_2$ molecule as a test system. In figure 2.2 we show the binding energy of $O_2$ as a function of interatomic distance, as computed with the "hard" and "soft" datasets introduced in section 2.4.2. All calculations were performed at complete convergence with respect to the kinetic energy cutoff. It can be seen that, although very close, the two curves deviate from each other, especially at smaller distances. In the inset the difference of the two curves is reported as a function of the interatomic distance. The vertical dotted line, present both in the main plot and in the inset, marks the distance at which there is no more overlap between the projectors belonging to the two oxygen atoms for the soft dataset. When the interatomic distance increases beyond the dotted line the "hard" and "soft" curves should coincide exactly. This is indeed the case, except for a small residual difference, less than 5 meV, due to the incompleteness of plane-wave expansion of the projectors[3]. At smaller distances the overlap between projectors of the "soft" dataset does however produce an error of a few kcal/mol at the equilibrium distance.

Although very small and rather acceptable in most situations, this error must be kept in mind when high accuracy is desired and the all-electron accuracy of PAW method is claimed.

[3]As the projectors are only applied to the crystal wavefunctions, higher Fourier components that may be present in the projectors expansion can be safely ignored; according to some generation recipe projectors are not even supposed to be soft, having a discontinuous derivative a the border of the augmentation region.

# Chapter 3

# Computational study of chemical reactions

*In this chapter we will see how to use the results of electronic-structure calculations, such as forces and total energy, to study chemical reactions. The methods presented in this chapter are general: they do not depend on the specific method and approximations used for the underlying calculations. Nevertheless, in our study we have always used the first-principle methods described in chapter 2.*

*In section 3.1 we will describe the Broyden-Fletcher-Goldfarb-Shanno (BFGS) [12, 27, 29, 73] algorithm, a very general optimization algorithm. We have used BFGS method to optimize the geometry of our systems: to minimize the energy and the internal forces in order to find the most stable configuration.*

*In section 3.4 we will describe one possible approach to the study of rare events: the nudged-elastic band method (NEB) [35, 34, 32]. It allows the calculation of reaction barriers that would be inaccessible to a full dynamic calculation because of the reaction rate being too low compared to a reasonable simulation time-step and length.*

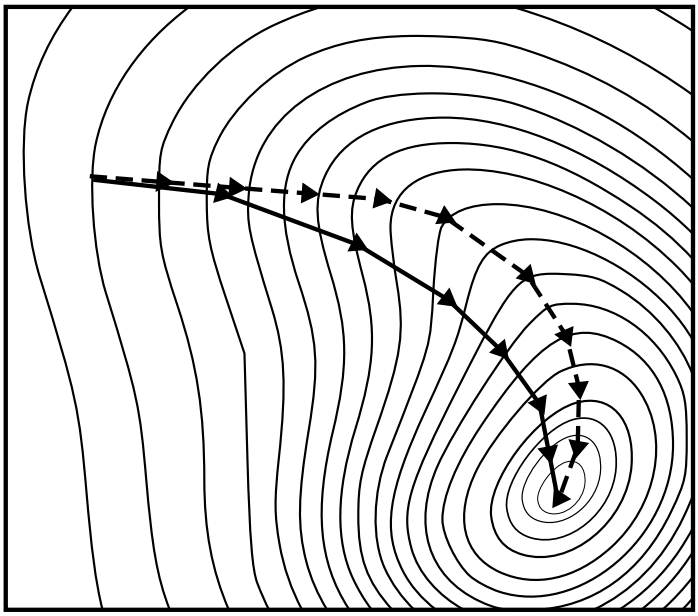

Figure 3.1: The BFGS algorithm (solid line) can reach convergence faster than a standard Steepest Descent (dashed line) simulation by using information on the curvature.

## 3.1 Geometry Optimization (BFGS)

The Broyden-Fletcher-Goldfarb-Shanno method [12, 27, 29, 73] is an improvement on the original Newton's algorithm for function optimization. It requires at each optimization step an estimation of the function and of its first derivatives; it uses them to compute the Hessian matrix of second derivatives, from finite differences, in order to speed-up convergence. In our application the function to minimize will be the total energy of the system and its first derivatives are the forces, which can be computed rather inexpensively using the Hellmann-Feynman theorem, as explained in section 2.1. The second derivatives of the energy can be computed from density-function perturbation theory, as they are related to phonon-frequency at the $\Gamma$ point in the Brillouin zone [8], but their estimation is very expensive; therefore the Hessian is obtained from finite-differences using the value of the forces computed at the previous minimization steps.

We denote the function to be minimized with $E(\mathbf{x})$ and its gradient with $F(\mathbf{x}) = -\nabla_{\mathbf{x}} E(\mathbf{x})$.

The minimization will proceed through a series of discrete steps $\mathbf{x}_k$, $k = 1, 2, ....$ At each optimization stage a new step is taken in direction $\mathbf{d}_k$ defined by the following equation, where $B_k$ is the best estimate for the Hessian matrix available at iteration $k$:

$$B_k \mathbf{d}_k = F(\mathbf{x}_{k-1}) \,. \tag{3.1}$$

In order to define a step length the code uses a trust-region procedure [18]. The algorithm estimates a trust radius inside which the second-order expansion of $E(\mathbf{x})$ is considered accurate enough; it then moves to the estimated minimum, if it is inside the trust region; otherwise it proceeds up to the extreme of the trust region toward the estimated position of the minimum. Once the step length $\lambda_k$ has been decided the step is defined as $\mathbf{s_k} = \lambda_k \mathbf{d}_k$. A new trust radius is then computed from the old one wit ha rescaling procedure; the rescaling factor depends on how well the estimate of the function computed at the previous iteration matched the actual value.

Finally we give the expression used to estimate the Hessian matrix for the next step:

$$B_{k+1} = B_k + \frac{\delta F_k \delta F_k^T}{\delta F_k^T \mathrm{s}_k} - \frac{B_k \mathbf{s}_k \left(B_k \mathbf{s}_k\right)^T}{\mathbf{s}_k^T B_k \mathbf{s}_k} \,; \tag{3.2}$$

where $\delta F_k = F(\mathbf{x}_k + 1) - F(\mathbf{x}_k)$; $\mathbf{s}_k$ is the previous step.

The BFGS algorithm is expected to converge faster than a simple steepest descent or damped-dynamics algorithm as it uses the additional accumulated information on the local curvature of the studied function to take a more direct route to the minimum point. In practice this is only true as long as the estimate of the Hessian matrix is good; in our application we have found it to give satisfactory results.

## 3.2 Chemical Equilibrium in Reactions

In this section we will briefly recall the concept of chemical equilibrium, how it relates to the concept of chemical potential of chemical species involved in a reaction; finally we will

see why theoretical calculations for separate isolated systems cannot be compared directly but has to be referred to an absolute energy scale and how to do it.

We start by considering a chemical reaction that transforms two reactants in two products according to the following scheme:

$$\alpha A + \beta B \rightleftharpoons \gamma G + \delta D\,. \tag{3.3}$$

The chemical species $A, B, G$ and $D$ can be elements, molecules or more abstract concepts such as adsorption sites; $\alpha, \beta, \gamma$ and $\delta$ are the stoichiometric coefficients of each species involved in the reaction. After a possible transient period, the reaction will reach a steady state: the relative abundance of reactants and products will be such that the direct and inverse reactions happen with equal frequency. This state is the chemical equilibrium of the reaction.

It can be shown [39] that at equilibrium the sum of the chemical potentials, multiplied by the stoichiometric factor of the species in the reaction, must be equal for reactants and for products:

$$\alpha\mu_A + \beta\mu_B = \gamma\mu_G + \delta\mu_D, \tag{3.4}$$

$$\alpha\mu_A + \beta\mu_B - \gamma\mu_G - \delta\mu_D = 0\,. \tag{3.5}$$

The opposite argument is also true: if this linear combination of chemical potentials does not sum up to zero the reaction will proceed in the appropriate direction in order to establish the equilibrium. If the products are actively removed from the system by some external mean the equilibrium will never be reached. It is also important to note that the use of a catalyst does not change the equilibrium point: by lowering the involved energy barriers it improves both direct and inverse reactions. In other words, the total equilibrium only depends on the chemical potentials of initial and final species, while the catalyst only acts on the intermediate steps of the reaction.

This equality is extremely useful to estimate the population of chemical species; in particular we will use it to estimate the coverage of a surface by adsorbates. When the adsorbates are

at equilibrium with the gas phase we can equate their chemical potentials; for the adsorbed state it is composed of the adsorption energy $\varepsilon^\star$ and an entropic contribution depending on the coverage [2][1]:

$$\mu_g = \varepsilon^\star + k_B T \ln\left(\frac{\theta}{1-\theta}\right) ; \tag{3.6}$$

the expression can be easily inverted giving the following expression for coverage:

$$\theta = \frac{1}{1 + e^{\left(-\frac{\mu_g - \varepsilon^\star}{k_B T}\right)}} ; \tag{3.7}$$

in the case of low-coverage ($\theta \ll 1$) it can be further simplified:

$$\theta = e^{\left(\frac{\mu_g - \varepsilon^\star}{k_B T}\right)} . \tag{3.8}$$

### 3.2.1 Chemical Potential for the Gas Phase

During the course of our study we will need to estimate the chemical potential of molecular species in the gas phases. Furthermore, we will need it at the condition of temperature and pressure that matches the experimental ones.

$$\mu_g = \left.\frac{dF}{dN}\right|_{T=\text{const}} \tag{3.9}$$

where $F$ can be the Helmoltz or Gibbs free energy depending on the details of the system: the former should be used when pressure is constant, while the latter for constant volume. $F$ itself is related to the logarithm of the partition function.

In particular, for a gas of $N$ classical non-interacting particles, $F$ is just $N$ times the average per-particle energy, hence the chemical potential can be computed from the partition function $\mathbf{Z}^g$ according to the following relation [2]:

$$\mu^g = -k_B T \ln \mathbf{Z}^g . \tag{3.10}$$

the partition function itself can factorized as following:

$$\mathbf{Z}^g = \mathbf{Z}^g_{\text{trans}} \times \mathbf{Z}^g_{\text{int}} , \tag{3.11}$$

[1] In this frame we are ignoring the vibrational modes for the adsorbed specie

where $\mathbf{Z}^g_{\text{trans}}$ is the translational part, associated with the kinetic energy of the molecule while $\mathbf{Z}^g_{\text{int}}$ is the internal part, associated with the roto-vibrational modes and the electronic energy levels. The kinetic part can be easily estimated by explicitly integrating the kinetic energy of a particle in a box, weighted with the Boltzmann distribution function, and then taking the thermodynamic limit $V \to k_B T/P$;

$$\mathbf{Z}^g_{\text{trans}} = \left(\frac{M k_B T}{2\pi\hbar^2}\right)^{3/2} \frac{k_B T}{P}\,; \tag{3.12}$$

where $M$ is the mass of the molecule.

On the other hand, to estimate the internal part is all but straightforward, as the number of roto-vibrational modes depends on the geometry of the molecule and, for a real gas, the summation has to take carefully into account the degeneracy associated with the spin state of the nuclei[2]. On the other hand, vibrational and rotational energies are usually quite small and can often be ignored; for molecules containing hydrogen, like $H_2$ or $NH_3$ it is worth including the zero-point energy (which is the energy of the first vibrational mode). Even for $H_2$ the first rotational mode has an energy of only a few meV. In table 3.1 we report the vibrational energies for a few molecules related to our work.

We have decided to use pre-tabulated values of $\mu^g$ from the NIST-JANAF thermochemical tables [15]. The tables provide the Helmholtz Free Energy, or enthalpy $A$, referred to $A^0 = A(T = 20^\circ\, C) = 0$, and entropy $S$ for a huge number of chemical species in the gas phase. Both quantities are tabulated at reference pressure $p^0 = 1000$ hPA and for a wide range of temperatures, from 0 K to about 1000 K. The chemical potential at the reference pressure can be computed according to the following relation [67]:

$$\mu^0(T) = \mu(T, p^0) = \left(A(T, p^0) - A^0(p^0)\right) - T\left(S(T, p^0)\right)\,. \tag{3.13}$$

The values of $\mu^0(T)$, computed from the JANAF tables, are reported in 3.2 for the molecules involved in our study. From equation 3.13 it is easy to compute $\mu$ at any pressure using the

[2] e.g. for a bi-atomic molecule a rotation along an axis perpendicular to the molecule axis will take the system back to its initial state after a 180° rotation if the spins of the nuclei are aligned, but only after a 360° if they are not.

Table 3.1: Vibrational frequencies for $H_2$, $N_2$ and $NH_3$; zero-point energy corresponds to $\frac{1}{2}$ the lowest energy. All the frequencies were calculated using Density Functional Perturbation Theory and PAW datasets in the Quantum-ESPRESSO code [8, 28].

| | | | | | | | | | | | | |
|---|---|---|---|---|---|---|---|---|---|---|---|---|
| Hydrogen $H_2$ | | | | | | | | | | | | |
| eV | 540 | | | | | | | | | | | |
| $cm^{-1}$ | 4353 | | | | | | | | | | | |
| Nitrogen $N_2$ | | | | | | | | | | | | |
| eV | 293 | | | | | | | | | | | |
| $cm^{-1}$ | 2367 | | | | | | | | | | | |
| Ammonia $NH_3$ | | | | | | | | | | | | |
| meV | 130 | 202 | 426 | 436 | | | | | | | | |
| $cm^{-1}$ | 1046 | 1631 | 3432 | 3518 | | | | | | | | |
| degeneracy | 1 | 2 | 1 | 2 | | | | | | | | |
| Hydrazine $N_2H_4$ | | | | | | | | | | | | |
| meV | 61 | 100 | 133 | 148 | 154 | 162 | 200 | 209 | 424 | 424 | 434 | 440 |
| $cm^{-1}$ | 495 | 804 | 1070 | 1197 | 1245 | 1302 | 1615 | 1686 | 3418 | 3419 | 3502 | 3545 |

following relation:

$$\mu(T,p) = \mu^0(T) + k_B T \ln\left(\frac{p}{p^0}\right) . \tag{3.14}$$

### 3.2.2 Chemical Potential for Adsorbed Species

Computing the chemical potential for a molecule adsorbed on a surface is conceptually very similar to doing it for a gas, as the fundamental relation between $\mu$ and the partition function, from equation 3.10 always holds. What is different is the form of the partition function:

$$\mathbf{Z}^a = \mathbf{Z}^a_{\text{site}} \times \mathbf{Z}^a_{\text{int}} \times \mathbf{Z}^a_{\text{bind}} . \tag{3.15}$$

The first factor of the right-hand side is the entropic, or configurational, contribution to the partition function. In the simplest case, where only one kind of surface site is available and the molecule can only adsorb in one way, it has the following form:

$$\mathbf{Z}^a_{\text{site}} = \frac{S!}{N!(S-N)!} \tag{3.16}$$

Table 3.2: Values of the gas chemical potential $\mu^0$ as a function of temperature, for $H_2$, $N_2$ and $NH_3$ at the reference pressure of 1000 hPa and at 10 hPa. JANAF tables have different temperature resolution for different species; an empty cell has been left where data was not available. The chemical potential is expressed in eV.

| | | | $p^0$ (1000 hPa) | | | $p$ (exp.) (6hPa) | | |
|---|---|---|---|---|---|---|---|---|
| T [K] | T [°C] | $k_B$T [eV] | $\frac{1}{2}$ $H_2$ | $N_2$ | $NH_3$ | $\frac{1}{2}$ $H_2$ | $N_2$ | $NH_3$ |
| 0 | −273.15 | 0.000 | 0.000 | 0.000 | 0.000 | 0.000 | 0.000 | 0.000 |
| 100 | −173.15 | 0.009 | −0.037 | −0.037 | −0.127 | −0.049 | −0.169 | −0.155 |
| 200 | −73.15 | 0.017 | −0.094 | −0.094 | −0.302 | −0.118 | −0.380 | −0.358 |
| 250 | −23.15 | 0.022 | −0.126 | −0.126 | – | −0.156 | −0.492 | – |
| 298.15 | 25 | 0.026 | −0.158 | −0.158 | −0.492 | −0.194 | −0.603 | −0.574 |
| 300 | 26.85 | 0.026 | −0.159 | −0.159 | −0.495 | −0.196 | −0.607 | −0.578 |
| 350 | 76.85 | 0.030 | −0.194 | −0.194 | – | −0.236 | −0.724 | – |
| 400 | 126.85 | 0.034 | −0.229 | −0.229 | −0.701 | −0.278 | −0.844 | −0.812 |
| 450 | 176.85 | 0.039 | −0.266 | −0.266 | – | −0.320 | −0.966 | – |
| 500 | 226.85 | 0.043 | −0.303 | −0.303 | −0.965 | −0.364 | −1.089 | −1.104 |
| 600 | 326.85 | 0.052 | −0.380 | −0.380 | −1.141 | −0.453 | −1.340 | −1.308 |
| 700 | 426.85 | 0.060 | −0.459 | −0.460 | −1.374 | −0.544 | −1.596 | −1.568 |
| 800 | 526.85 | 0.069 | −0.541 | −0.541 | −1.614 | −0.638 | −1.856 | −1.835 |
| 900 | 626.85 | 0.078 | −0.624 | −0.625 | −1.860 | −0.734 | −2.121 | −2.109 |
| 1000 | 726.85 | 0.086 | −0.710 | −0.710 | −2.112 | −0.831 | −2.390 | −2.390 |
| 1100 | 826.85 | 0.095 | −0.797 | −0.797 | −2.178 | −0.930 | −2.661 | −2.483 |
| 1200 | 926.85 | 0.103 | −0.885 | −0.886 | −2.448 | −1.030 | −2.936 | −2.781 |

which is just the number of possible distinct configurations for $N$ particles adsorbed among $S$ available sites. It produces the first term of the chemical potential, through the Stirling approximation, with expression:

$$\mu^a_{\text{site}} = -k_B T \ln\left(\frac{N}{S-N}\right) \tag{3.17}$$

$$= -k_B T \ln\left(\frac{\theta}{1-\theta}\right); \tag{3.18}$$

where we have introduced the dimension-less coverage $\theta = N/S$. For more complicated systems, especially when more that one site is available or when neighbouring sites interact with each other, more complicated expressions have to be used.

The second factor of $\mathbf{Z}^a_{int}$, the internal partition function, is in principle very similar to the one for the gas: it keeps in account the possible roto-vibrational modes of the molecule. The internal partition function for the gas $\mathbf{Z}^g_{\text{int}}$ is often used in place of $\mathbf{Z}^a_{\text{int}}$; this approximation implies that the rotational modes that are strongly perturbed by the surface interaction can be ignored, and that the vibrational modes remain mostly unperturbed. It also ignores rigid vibrations of the adsorbed species with respect to the surface. Taking $\mathbf{Z}^g_{\text{int}}$ works sufficiently well when dealing with physisorption, i.e. when a molecule adsorbs without modifying its chemical structure, but it is clearly insufficient when dissociation follows the adsorption.

In the case of chemisorption, or dissociative adsorption, of diatomic molecules it is often more accurate to ignore $\mathbf{Z}^a_{\text{int}}$ altogether: once the molecule has been atomized the adsorbed atoms have no rotational modes and the surface-adatom vibrations have usually very low energy. As an example, in the specific case of Hydrogen atoms adsorbed on the Palladium (111) surface the perpendicular vibrational mode has an experimental energy of 124 meV[3], which reduces to 68 meV for under-surface Hydrogen atoms [60, 17].

The last factors of equation 3.15 is the binding energy of the adsorbed species. If there is a single adsorption site and if neighbouring sites do not interact, it is simply:

$$\mathbf{Z}^a_{\text{bind}} = exp(-\varepsilon^a / k_b T), \tag{3.19}$$

[3]The vibrational mode of $H_2$ gas is 530 meV per molecule, which can be interpreted as 265 meV per Hydrogen atom, the zero-point energy is half this value.

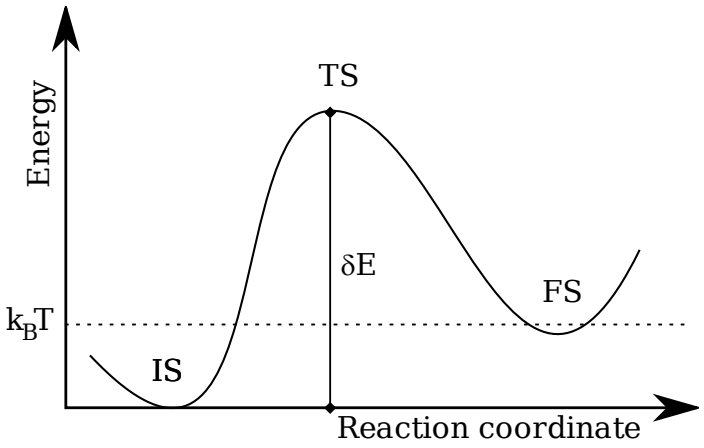


Figure 3.2: Schematic representation of a thermally activated process; the system can go from the initial state (IS) to the final state (FS) by crossing a transition state (TS) which can be several $k_BT$ higher in energy.

where $\varepsilon^a$ is the adsorption energy, and it gives a contribution $\varepsilon^a$ to the chemical potential. Conversely, if there are more adsorption sites, or if they interact, the expression becomes much more complex and may require additional assumption and approximations to be evaluated analytically.

## 3.3 Transition State Theory

A typical chemical process consists in the conversion of reactants to products; usually the reaction cannot progress spontaneously but has to cross an energy barrier that requires a certain amount of energy to be climbed. Even though the source of energy can be of different kinds, such as adsorption of a photon, transition state theory can be used especially for thermally activated processes.

The main difficulty in the study of this kind of processes is that the reaction, though it appears slow at a macroscopic scale, is actually fast but rare at a microscopical scale. In other words, at the microscopic scale it happens rarely that one dose of reactants combine to form one dose of products, but the process itself is fast. As a consequence it is not possible

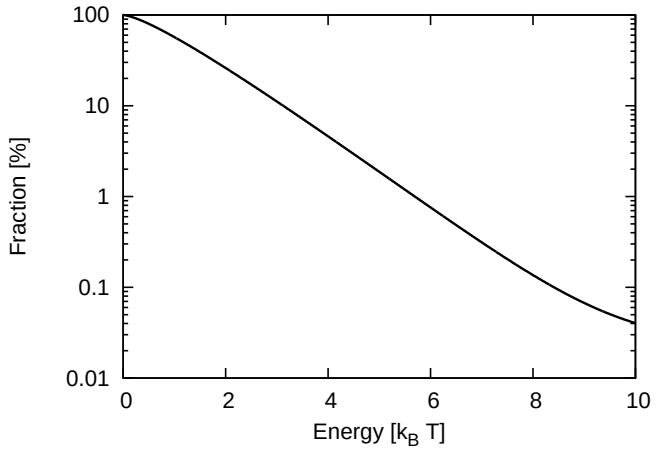


Figure 3.3: Fraction of gas molecules with kinetic energy larger than the amount specified in the $x$ axis, according to Maxwell-Boltzmann distribution. When the threshold becomes larger than a few $k_BT$ the percentage drops to extremely small values.

to study the chemical process with a dynamical simulation: the accuracy of simulated dynamics depends strongly on the time step used to integrate the motion equation which, in a typical system, must be of the order of the femtosecond. Conversely the computational cost does not allow for more than $10^3 - 10^5$ time steps, depending on the technique used, with DFT being one of the most expensive ones. Therefore if a process takes more than $10^{-10}$ s to cross the barrier, it is beyond the reach of direct dynamical simulations.

To have a first qualitative idea, let's consider a gas at a certain temperature T: the kinetic energy of gas particles will have a Maxwell-Boltzmann kinetic energy distribution:

$$\langle \theta(E) \rangle \; dE = 2\sqrt{\frac{E}{\pi (kT)^3}} e^{\left(\frac{-E}{kT}\right)} \, dE \, . \tag{3.20}$$

From the form of the distribution it is clear that only a very small fraction of the molecules will have a kinetic energy larger than a few $k_BT$, and only when one of these energetic molecules happen to collide with another the reaction can cross a high barrier.

To deduce a quantitative estimate we need to make two assumptions the first is that the system does not deviate from thermal equilibrium; the second requires that there is an

intermediate state, called transition state (TS) that the system has to cross when going from the initial state (IS) to the finals state (FS). The second assumption is clarified in figure 3.2; it requires the system to only travel via the minimum energy path (MEP), i.e. the path which has the lowest possible maximum energy.

From this assumptions the transition rate $k$, for the process IS $\rightarrow$ TS $\rightarrow$ FS, is defined as the probability for the system to sit at the TS with velocity pointing toward the final state:

$$k = \frac{\left\langle \frac{p}{m}\delta\left(q - q^{TS}\right)\theta(p)\right\rangle}{\langle\theta(q - q^{TS}\rangle} \tag{3.21}$$

$$= \frac{1}{\langle\theta(q - q^{TS})\rangle}\exp\left(\frac{-\beta E(q^{TS})}{\beta}\right) \tag{3.22}$$

where $\beta$ is $1/k_BT$ and $p$, $q$ are the generalized momentum and the generalized coordinates. Expanding $E(q)$ around the IS to the second order in $q$ we give an estimate for the denominator of equation 3.22:

$$\left\langle\theta(q - q^{TS})\right\rangle = \frac{2\pi e^{-\beta E(q^{IS})}}{\beta\omega(q^{IS})} \tag{3.23}$$

where $\omega(q^{IS})$ is the harmonic frequency at IS:

$$\omega(q^{IS}) = \left(\frac{1}{m}\left.\frac{\partial^2 E(q)}{\partial q^2}\right|_{q=q^{IS}}\right)^{1/2}. \tag{3.24}$$

Substituting equation 3.23 in 3.22 we get the well known van't Hoff-Arrhenius law:

$$k = \frac{1}{2\pi}\omega(q^{IS})e^{-\beta\delta E} \tag{3.25}$$

where not only we provide the exponential relation that links the energy barrier and the temperature with the rate, but also an estimate of the prefactor.

To generalize this result to a larger number of coordinates we observe that in general two minima are separated by a saddle point, there can be more than one but this adds no additional difficulty since each one can be considered separately. For a system with $3N$ degrees of freedom the saddle point will have $3N - 1$ real vibrational frequency and an imaginary one, corresponding to the instability along the MEP. Conversely all the $3N$

vibrational frequencies at the IS are real, as it is a local minima. Assuming the harmonic approximation to hold in both points we can generalize equation 3.25 in the following way:

$$k = \frac{1}{2\pi} \frac{\prod_{i=1,3N} \omega_i(q^{IS})}{\prod_{i=1,3N-1} \omega_i(q^{TS})} e^{-\beta\delta E} \,. \tag{3.26}$$

From this equation we can see that the transition rate only depends on the ground-state properties of the IS and the TS, and on the energy difference of the two states. Instead of sampling the entire free-energy landscape we can have a reasonable estimate by finding the lower saddle point between IS and FS; saddle points with a higher energy can usually be neglected, as the exponential factor will kill their contribution.

Determining the MEP is still a far from trivial task, especially for a large number of degrees of freedom, as the most convenient path can be far away from the shorter one; in the next section we will see one of the most popular algorithm currently used to tackle this problem.

## 3.4 Study of Rare Events (NEB)

The Nudged-Elastic Band (NEB) is a specific algorithm used to find the Minimum-Energy Path (MEP); if we imagine the free-energy of a multi-dimensional configuration space as a landscape we can define the MEP as the specific path, connecting two arbitrary points, that minimizes the maximum value of free energy along itself. As we are not interested in the average of the free energy along the path, but only on its maximum, there is no constraint on the length of the path itself, which in principle can become extremely long.

The number of dimensions of the configurations space is equal to the number of degrees of freedom in the system, hence it is prohibitive to sample uniformly; the NEB method aims at finding the MEP with a minimum number of calculations. Nevertheless, the computational cost of NEB calculations is often one or two order of magnitude larger than a simple optimization calculation, as we will see in a while.

The NEB algorithm is built on several previous method; the oldest one is the Chain of states method [43], it works by constructing a certain number of intermediate configurations, usually called images, between the initial and the final point of the path, which are fixed. The free energy of each image is then optimized with the constrain of keeping the distance between consecutive images equal: the path is allowed to elongate or contract, but the images will remain equispaced; if the constraint is imposed by adding a fictitious spring of natural length zero between images then the algorithm is called plain-elastic band (PEB) and is, in fact, equivalent to a Feynman path integral. The PEB algorithm aims at minimizing the following functional:

$$S(\mathbf{R}_2, .., \mathbf{R}_{p-1}) = \sum_{i=0,p} F(\mathbf{R}_i) + \sum_{i=2,p} \frac{K_i}{2} |\mathbf{R}_i - \mathbf{R}_{i-1}|^2 \tag{3.27}$$

where $\mathbf{R}_i$ is the set of degrees of freedom of image $i$, $F(\mathbf{R}_i)$ its free energy and $K_i$ the elastic constant of the spring connecting image $i$ to image $i-1$. There have been several improvement to the functional form but we will not present them here[4].

While going from the the initial to the final configuration the MEP crosses one or more saddle points, one of which shall be the point of maximum energy, i.e. the transition state; estimating accurately the energy of this point is extremely important for the quality of the algorithm because, as we have seen in section 3.3, it determines the reaction rate. The PEB algorithm has proven effective in many applications, but tends to systematically overestimate the energy of the transition state. The reason is hinted in figure 3.4; it can be seen how PEB tends to "cut the corners", by making the path shorter and reducing the elastic energy of the strings at the expenses of the potential energy of the system.

NEB is a major improvement to this problem although it is quite similar to the original algorithm; the basic idea is to optimize each image by letting act only the component of the spring force parallel to the path and the component of the internal forces orthogonal to the path. More formally, the forces acting on image $i$ are decomposed in the following way:

$$-\nabla_{\mathbf{R}} E = -\nabla^{\perp}_{\mathbf{R}} E - \nabla^{\parallel}_{\mathbf{R}} E \tag{3.28}$$

$$\mathbf{F}_S = \mathbf{F}^{\perp}_S + \mathbf{F}^{\parallel}_S \,. \tag{3.29}$$

[4] A detailed and throughout description of historically MEP methods can be found in ref [32].

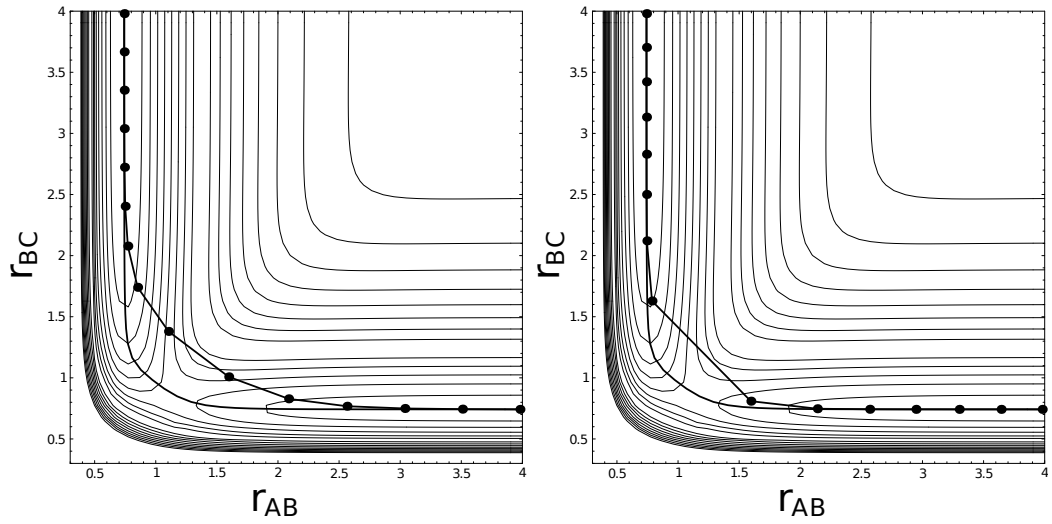


Figure 3.4: The PEB algorithm (left) is compared to the NEB algorithm (right) in a test case where a certain atom A can bond to either B or C; the thick lines joining the dots are the two approximation of the MEP, which is the continuous thin line. It is possible to see how PEB tend to "cut the corners" in the free energy landscape overestimating the saddle point energy (adapted from [32]).

The total force acting on each image is then defined as:

$$\mathbf{F} = \mathbf{F}_S^{\parallel} - \nabla_{\mathbf{R}}^{\perp} E \tag{3.30}$$

This modifications to the algorithm prevents the NEB from cutting the corners, as shown in figure 3.4.

The implementation of NEB that we have used also allows one to define a climbing image [35, 34, 71], which forces the highest energy image to climb the free-energy gradient; this technique improves the estimation of the saddle point by trying to get an image as close as possible to it. The climbing image does not feel the spring force but climbs up the component of internal forces parallel to the string.

# Chapter 4

# The Palladium-Hydrogen system

*In this chapter we will examine the structure of our catalyst, Palladium, when exposed to a large amount of Hydrogen. In the first section, ad its subsections, we will examine in-depth the characteristic of Palladium bulk and its capacity to adsorb Hydrogen atoms; we will see how the system can reach different phases and their geometrical and chemical characteristics.*

*In section 4.2.2 we will move our focus to the Palladium* (111) *surface, which determines Palladiums catalytic properties. We will use a simplified first-principle model to estimate the Hydrogen occupation of the superficial adsorption sites at different thermodynamical conditions. Finally we will use our model to propose a possible structure for the system at the experimental conditions.*

## 4.1 Bulk-adsorption of Hydrogen in Palladium

It has been well known since the sixties that Palladium can incorporate a large amount of Hydrogen; the adsorbed Hydrogen spontaneously dissociate and can diffuse into the bulk with a very low diffusion barrier [47, 25]. What makes the PdH system very interesting is that it can exhibit at least two phases, depending on the ratio $r = N_H/N_{Pd}$, where

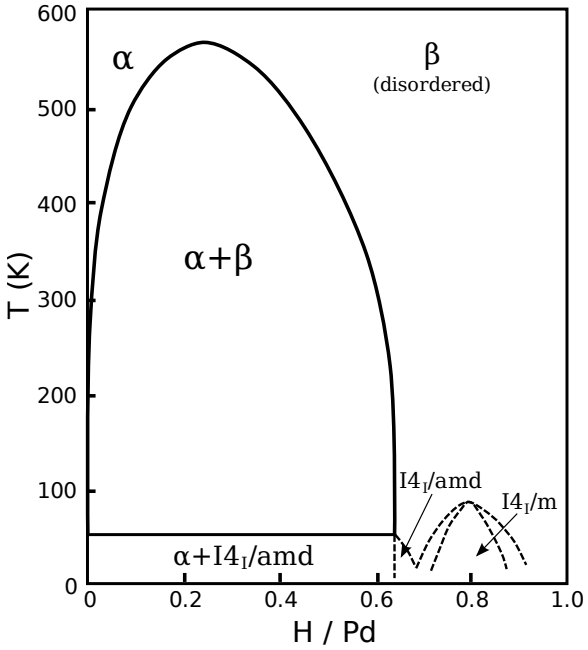


Figure 4.1: Phase diagram of the Palladium-Hydrogen system as a function of the H/Pd ration and temperature (adapted from ref. [66]).

$N_H$ and $N_{Pd}$ are the number of Hydrogen and Palladium atoms in the system. The first phase, called $\alpha$-phase is characterized by very low Hydrogen concentration in the bulk, low absorption energies and unperturbed Palladium structure. The $\beta$-phase occurs at much higher Hydrogen concentration when $r \gtrsim 0.5$; it has slightly higher adsorption energy and the Palladium lattice parameter increases considerably. An increase in volume of 10.4% [1] has been measured for values of $r$ around 50%. There are actually two variants of the $\beta$ phase, that correspond to different adsorption site for the Hydrogen, we will examine this difference in detail later on in this section. It has been suggested that a fourth phase, with simple-cubic lattice geometry, may arise for very high Hydrogen concentrations ($N_H/N_{Pd} \gtrsim 1.3$) and temperature in excess of 923 K [7]. The experimental phase diagram is represented in figure 4.1.

The transition from $\alpha$ to $\beta$ phase does not happen at standard conditions of pressure and temperature. In experiments high pressures (e.g. diamond anvil [33]) or low temperatures are used to favour the bulk adsorption of Hydrogen. In order to have a more

quantitative estimate we have computed the binding energy of Hydrogen in Palladium at several concentrations values. For the calculations we have used the tools contained in the Quantum-ESPRESSO distribution [28] implementing the methods of chapter 2; the technical details are described in more detail in section 5.1.

There are two possible high symmetry sites for the Hydrogen atoms to occupy in the interstices of bulk Palladium: the Octahedral site (O) and the Tetrahedral (T) site; the two configurations are represented in figure 4.2. It is important to note that there are 2 T sites for each Pd atom, we will call them $\mathrm{T}^u$ (the one with a vertex pointing upward) and $\mathrm{T}^d$ (downward); as they are equivalent the naming is purely conventional. We have verified with a NEB calculation that there is no diffusion barrier, other than the energy difference, between T and O sites. In other words, if the T site is favoured the T-T diffusion process has to pass through an O site, having the $\varepsilon_T - \varepsilon_O$ as and energy barrier; where $\varepsilon_X$ is the adsorption energy in site $X \in T, O$. If the O site is favoured than the O-O diffusion has to pass through a T site and the barrier will be $\varepsilon_O - \varepsilon_T$.

The name $\beta$-phase is normally referred to the case of Hydrogen adsorbed in the O site, which is the most commonly studied case. The name $\gamma$-phase has been sometimes used for Hydrogen adsorbed in the T site; although there is no widely-established convention, we will use this name in the present work.

### 4.1.1 PdH Phase at the Experimental Conditions

At the experimental conditions of 900 K of temperature and 6 kPa of partial Hydrogen pressure, the chemical potential of the gas phase Hydrogen is about $-778$ meV per $\frac{1}{2}\mathrm{H}_2$ (see table 3.2). Conversely the binding energy depends on the site (O, T) and on the relative concentration. We have computed it for a few different configurations in a $2\times2\times2$ Palladium FCC supercell. In every case we have relaxed the geometry and the unit-cell volume. We have also repeated the calculation with one Hydrogen in the supercell relaxing the geometry but not the unit-cell volume, provided that adsorbed Hydrogen interact substantially only

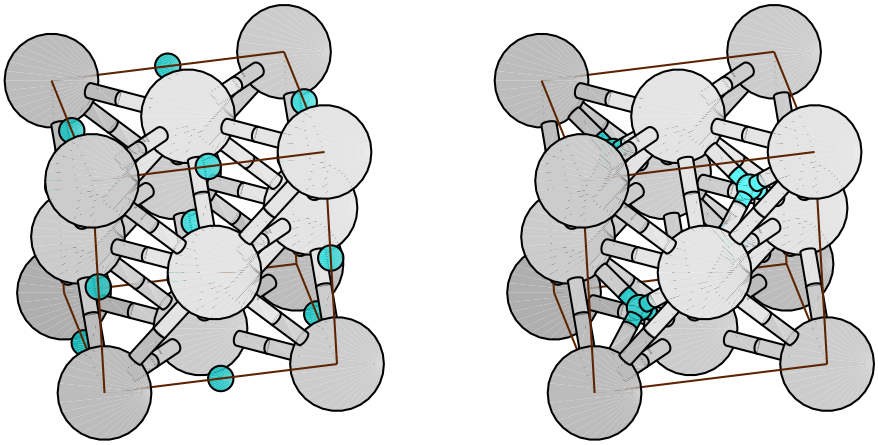

Figure 4.2: Hydrogen adsorbed in the Octahedral (left) and Tetrahedral (right) site in Palladium bulk. The H/Pd ratio is 100% in both pictures [41].

up to nearest-neighbours, this calculation can be used as a good approximation for very low Hydrogen concentration.

Even in the most stable site at the most favourable concentration the binding energy is only about 160 meV. Because of the low mass of Hydrogen we also have to keep into account zero-point vibrational energy. From a very rough estimate based on the reduced mass of the H−H system and the H-Pd system we expect the vibrational frequency of the H-H system to be grossly twice as high as in the Pd−H system. Indeed, the zero-point energy is 135 meV for $\frac{1}{2}H_2$ in the gas phase, which we have computed from first-principles in section 3.2.1, and 51 meV in the bulk, which is available in literature [47].

The last term present in the chemical potential of Hydrogen dissolved Palladium bulk is the configurational entropy. We know that when the bulk concentration of Hydrogen approaches extreme values its chemical potential must tend to minus infinity, when the bulk does not contain any Hydrogen, and to plus infinity, when the bulk is completely filled-up with Hydrogen. In order to have a quantitative estimate we have made the following assumptions:

- neighbouring sites *of the same kind*, which are actually second-neighbours, do not

interact; e.g. the energy of an Hydrogen occupying a $T^u$ sites does not depend on the occupation of any other $T^u$ site;

- binding energy of a site only depends on the average occupation of that site;
- there cannot be more than one Hydrogen per unit cell or, in other words, neighbouring sites *of different kind*, which are first neighbours, interact strongly and repulsively.

The last assumption is justified by the fact that neighbouring sites of different kind are much closer that neighbouring sites of the same kind. To support the assumption we have computed the site-site interaction and found a repulsion of 253 meV for neighbouring O-T sites, we could not estimate it for neighbouring $T^u$-$T^d$ sites as the configuration is not stable and spontaneously expels one of the Hydrogen atoms to another site. Assuming that only one kind of site can be occupied at any time we get the following expression the configurational partition function:

$$\mathbf{Z}_{\text{conf}} = \frac{S!}{(S-N)!N!} \exp\left(-\frac{\varepsilon_X N_X}{k_B T}\right) \tag{4.1}$$

Where $N_S$ is the number of Hydrogen atoms in site $X$, $\varepsilon_X$ is the adsorption energy for the site and $S$ is the total number of said sites, which is equal to the number of bulk Palladium atoms. From $\mathbf{Z}_{\text{conf}}$ we can calculate the chemical potential:

$$\mu_{\text{conf}} = -k_B T \ln\left(\frac{r}{1-r}\right) \tag{4.2}$$

where $r = N/S$ and all the Hydrogen atoms will be placed in the site with the higher binding energy, depending of the specific conditions.

This approximation is accurate at high coverage, and when the O site is substantially favoured over the T sites; but breaks down when we wish to occupy the Tetrahedral site and the Hydrogen population is low. In this case the $T^u$ and $T^d$ sites can be occupied indistinctly, as the chance of having two nearest-neighbours is negligible. As a consequence the number of available T sites is *twice* the number of bulk Palladium atoms. Repeating the calculation of equations 4.1 and 4.2 we find that the chemical potential shifts by a factor $\delta\mu_{\text{conf}}$ defined as following:

$$\delta\mu_{\text{conf}} = -k_B T \ln(2)\,. \tag{4.3}$$

At the experimental temperature ($\simeq$ 900 K) this correspond to a change of 54 meV. However, as we are about to show, the Tetrahedral site is favoured only at high Hydrogen concentration, where the strong repulsive nearest-neighbour interaction does not allow the coexistence of $T^u$ and $T^d$ Hydrogen population in the same region of the bulk.

The equilibrium condition between the gas and bulk-adsorbed phases of Hydrogen is verified when:

$$\mu_g + \varepsilon_v^g = \varepsilon_{\text{bind}} + \varepsilon_v^b + k_B T \ln\left(\frac{r}{1-r}\right) \tag{4.4}$$

$$\varepsilon_{\text{bind}} = \mu_g + \varepsilon_v^g - \varepsilon_v^b - k_B T \ln\left(\frac{r}{1-r}\right) \tag{4.5}$$

Where $\varepsilon_v^g$ and $\varepsilon_v^b$ are the Hydrogen vibrational frequencies in the gas phase and in the Palladium bulk, respectively; $\varepsilon_{bind}$ is the site adsorption energy and $\mu_g$ is the chemical potential of Hydrogen gas. At the experimental condition, it would not be sufficient to cause the transition phase from $\alpha$ to $\beta$. Nevertheless in the experiment a bias is used to force atomized Hydrogen through a proton conductor into the Palladium catalyst from below; we can model the effect of the bias as an additional constant term on the right-hand side of equation 4.4 and 4.5.

We attempt a graphical solution of eq. 4.5 in fig. 4.3. The lines with solid boxes and empty circles are binding energies, for the T and O sites respectively, at different Hydrogen concentration. According to our assumptions only the site with lower energy is occupied, namely the O site up to a concentration of about 55% and the T site for higher concentrations. The solid line, almost vertical on the left, is the right-hand side of equation 4.5: its intersection with the O-sites energy is the equilibrium state; it presents a negligible amount of bulk-adsorbed Hydrogen. The other two lines are parallel to the solid one but translated upward, simulating the effect of an additional effective chemical potential. The dashed one is translated by 300 meV and has an equilibrium point in a region where $\alpha$ and $\beta$-phase coexist, although the dominance of one over the other may depend on temperature. The dotted line is translated by 600 meV, it has an equilibrium point in the $\gamma$-phase. As we have seen in section 1.2.3 the lower value (300 meV) corresponds to the beginning of the

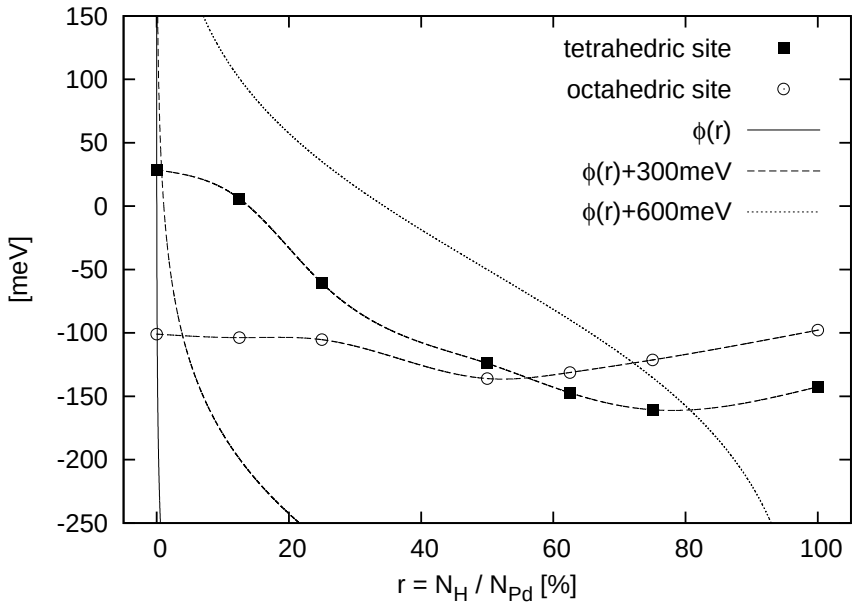


Figure 4.3: Graphical solution of eq. 4.5 at different cell potentials; a detailed explanation of this figure is present in the text.

NEMCA effect. Conversely at 600 meV the NEMCA effect (sec. 1.2) is already consistent with a improvement factor $\Lambda \simeq 2.0$.

Nevertheless the graph of fig. 4.3 should only be interpreted qualitatively, as it depends quite strongly on detail that we do not know with sufficient accuracy. It is not straightforward to estimate which fraction of the electrically-supplied energy is dissipated, by the proton-conductor resistance or other mechanism, which is used to improve the chemical reaction and which residual fraction contributes to increase the fraction of dissolved Hydrogen. Furthermore, in the experiment, different values have been used for the cell potential, raging from 0.4 V to 2.0 V. Finally, the assumptions we have made to give an analytical form for the bulk entropic contribution do not hold tightly when Hydrogen concentration becomes very high; primarily because neighbour interactions can become important and secondly because occupation of first neighbouring sites may appear, although only in a small percentage of the sites.

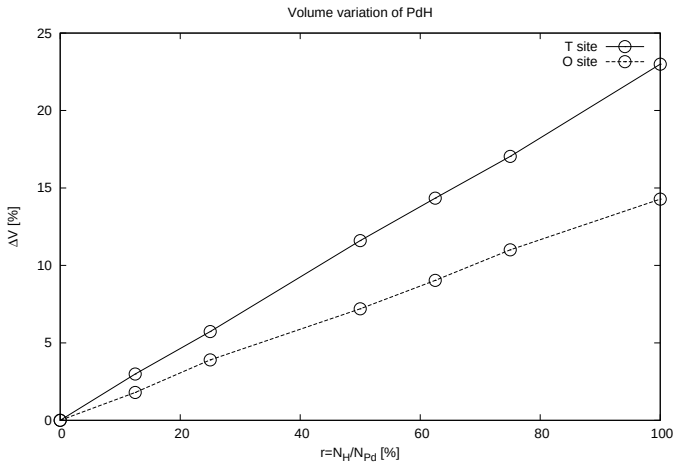


Figure 4.4: Volume variation in percentage of Palladium as a function of the fraction of adsorbed Hydrogen.

We can conclude stating that a high fraction of bulk-adsorbed Hydrogen is definitely present; although we do not know the exact concentration because of uncertainties in the parameter and approximation in our model. Nevertheless what will matter to our research are not the specific details of bulk structure, as much as the change in lattice parameter associated with the transition from the $\alpha$ to the $\beta$ or $\gamma$ phases. In section 4.2.2 we will examine the Hydrogen population of the surface with a different approach that produces more quantitative predictions.

### 4.1.2 PdH Phase at Ultra-high Pressure

To conclude this part we wish to justify an apparent inconsistency between our result and neutron-scattering experiments. Most experiments only detected Hydrogen in the O site, while our calculation predict that T site will be favoured for Hydrogen concentration higher than about 50%; there is one experiment where ion implantation techniques has been used to obtain Hydrogen concentration in excess of 100%, the experimentalists also found the T site to be favoured in these specific conditions [72].

On the other hand, the normal procedure to obtain high Hydrogen concentration requires

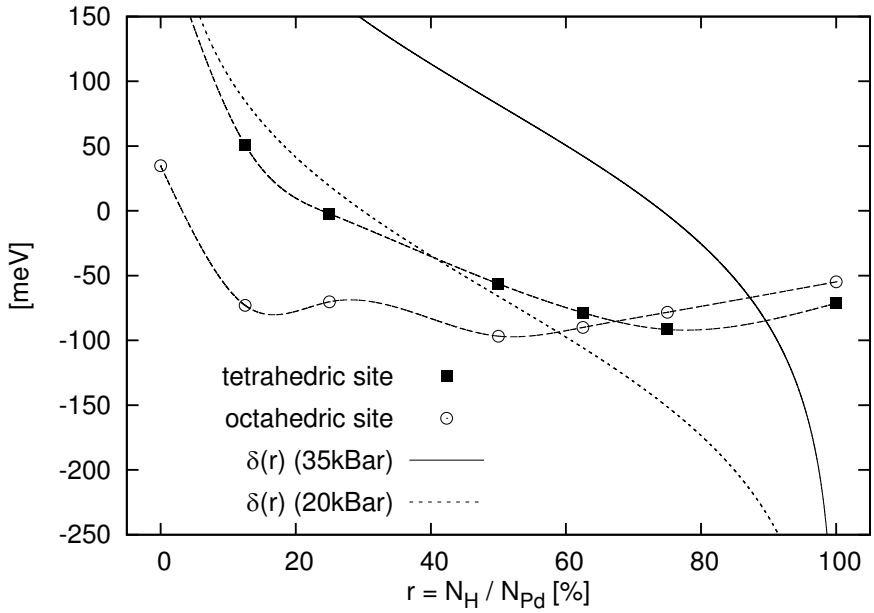


Figure 4.5: This figure is analogous to fig. 4.3 but binding energies were computed at 35kBar. The two plots of $\phi(r) = \mu_g + \varepsilon_v^g - \varepsilon_v^b - k_B T \ln\left(\frac{r}{r}\right)$ correspond to pressures 35kBar (solid) and 20kBar (dashed), because the dependence of adsorption energy on the external pressure is weak the two lines can be compared directly.

low temperature and extremely high pressure, in the order of 10 kBar. As you can see from figure 4.4, when the T sites are occupied the relaxed volume of the system increases faster with $r$ than when the O sites are occupied; as a consequence the use of high pressure may favour the O sites considerably. In order to check this hypothesis we have repeated the calculations for the binding energy at several concentration; but this time we have forced the system to relax the unit cell volume to bear a pressure of 35 kBar. Furthermore, at high pressure, the fugacity must be used instead of the pressure to compute the chemical potential of the gas phase, as they can differ by several orders of magnitude. In order to estimate the fugacity of Hydrogen we have used the parametrization from ref. [82]; the ratio of fugacity over pressure: $\phi = f/p$ is about 64.6 at 30 kBar and 268.2 at 35 kBar.

Even under these conditions we found that the T site is favoured for sufficiently high concentration: at 35 kBar the transition happens at $r \simeq 70\%$. Concurrently a more recent experiment [6] appears to agree with our results, even though at high temperature and pressure the formation of vacancies does not allow a simple quantitative comparison.

## 4.2 Characteristics of (111) Surface of Proton-Enriched Palladium

In the previous section we have studied the adsorption of Hydrogen in Palladium bulk. It is important to our system because the induced phase change can significantly modify the Palladium properties. Nevertheless the catalysis properties depend critically on surface structure, not on the bulk composition. We have focused our attention on the (111) surface; which is the most stable of primary surfaces and thus the most prominent in the nano-cluster structures used for catalysis.

In normal Palladium there is a slight relaxation of the superficial layer; from our calculations the bulk inter-layer equilibrium distance is of 2.281 Å. The distance between the first and the second surface layers increases to 2.290 Å, which corresponds to an increase of 0.36% with respect to the distance in the bulk. Conversely, the distance between the second and the third layer reduces slightly by 0.25%; the relaxation becomes then negligible for deeper layers.

In Palladium Hydride the inter-layer distance along the direction [111] is quite larger than in pure Palladium. The amount of linear expansion depends on the fraction of bulk Hydrogen; we have taken it to be 50% which causes the inter-layer distance to grow by 3.46%, for an equilibrium lattice constant of 2.360 Å. When the surface is exposed and relaxed the distance of the superficial layers decreases sensibly; it reduces to 2.245 Å, which corresponds to a 4.85% decrease. We have inserted some Hydrogen atoms in the third layer, which stops the surface contraction from progressing further. A 100% layer occupation of Hydrogen causes the second and third layers to expand substantially, precisely by 6.85%. On the other hand, a more realistic 50% layer of Hydrogen, in the tetrahedral sites between the third and the fourth layers, stabilises the inter-layer distance to 2.352 Å, which is only 0.29% away from the bulk parameter. This is the occupancy we will be using in chapter 5.

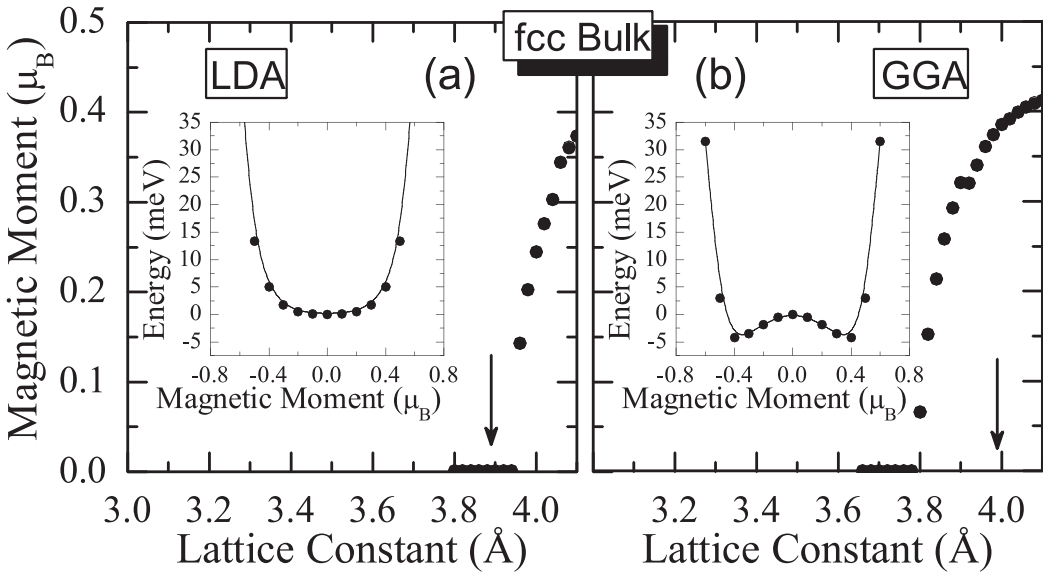


Figure 4.6: Per-atom magnetic moment as a function of the lattice parameter for LDA (left) and PBE (right) functionals. The inset shows the ground-state energy at fixed magnetisation at the equilibrium lattice constant (from ref. [3]).

### 4.2.1 Surface Magnetism

In nature bulk Palladium is not magnetic, nevertheless DFT calculations can present a small magnetic dipole; this effect has been well known and discussed in detail in the last years [21, 3, 22]. It is caused by the PBE functional (sec. 2.2) slightly over-estimating the unit cell volume, thus reducing the coordination of bulk atoms and favouring a magnetic ground-state. On the other hand, the LDA functional, which slightly over-binds the atoms, does not present this peculiar effect. In figure 4.6 we reproduce a picture from ref. [3] where the ground-state magnetic moment is plotted as a function of the lattice parameter.

In our calculation we have carefully chosen the computational parameters to reproduce this effect which, although spurious, is inevitable for a well-converged calculation. Adding Hydrogen to the Palladium bulk causes it to inflate, increases its lattice parameter; however the interstitial Hydrogen atoms have the effect to quench the magnetic moment.

A similar effect happens in proximity of the surface: surface atoms have a lower coordination

number and present a higher magnetic moment, but the magnetism is destroyed if a large number of Hydrogen atoms are adsorbed on the surface and in the first under-surface layers. The absolute magnetization ranges from a maximum of 1.50 $\mu_B$ per surface atom, when there is no Hydrogen in the first layers or on the surface, to a minimum of zero, when the surface and the first under-surface layers are saturated with Hydrogen. This effect is common to both proton-enriched and normal Palladium. We believe this high magnetic moment to be a genuine effect, because the spurious effect of the functional only accounts for a much smaller absolute magnetization, of about 0.4 $\mu_B$ per atom.

### 4.2.2 Adsorption of Hydrogen on Palladium (111) Surface

Because of the geometry of Palladium crystals the (111) surface is hexagonal; hence for each surface unit cell there is one on-top adsorption site, two equivalent bridge sites and two in-equivalent threefold sites; one threefold site corresponds to the structure of an over-surface additional FCC layer while the other correspond to an HCP layer. It is known from Low-energy Electron Diffraction studies that on (111) surface hydrogen can adsorb up to very high coverage favouring the threefold sites or the first under-surface Tetrahedral sites, situated between the first and the second layer [26]. We have also included the first under-surface Octahedral site which is situated right under the FCC one. The position of these sites is depicted in figure 4.7.

Under normal conditions, Hydrogen adsorbed on the surface has to be in equilibrium with both the gas an the bulk phases; because of its reduced symmetry computing the entropic contribution to the surface chemical potential is not as straight-forward as it is for the bulk. In particular it is not possible to assume single-occupation per surface unit-cell, making it difficult to estimate the partition function. In order to have a meaningful estimation we have decided to calculate surface and sub-surface Hydrogen population by Monte Carlo (MC) simulation. First-principle electronic structure calculations are far too computationally intensive to be used to compute the configuration energy at each step of a MC simulation; in order to have an approximate but extremely cheap estimate we have modelled the configu-

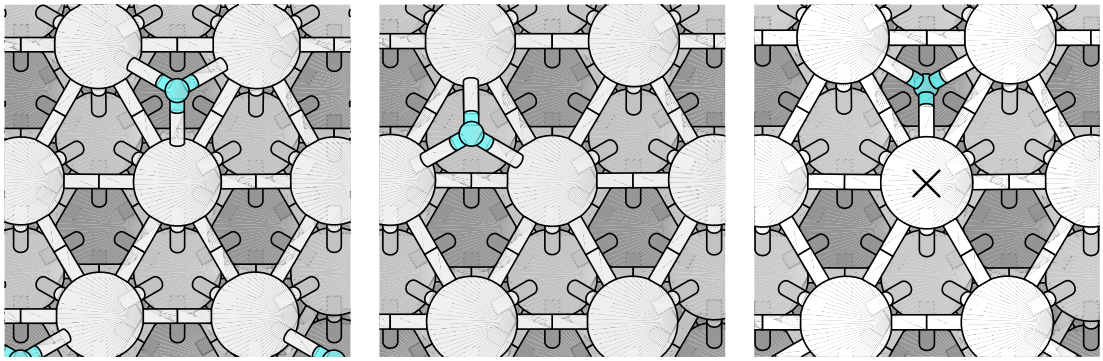

Figure 4.7: Hydrogen atoms adsorbed in the FCC (left) HCP (centre) and octahedral (right) sites on Palladium (111) surface [41]. The tetrahedral site is in the position marked by an $\times$ under the Pd atom.

rational energy expanding it as a sum of one-site and interaction terms.

To have accurate results we have tabulated on-site adsorption energies for each of the sites described in figure 4.7, included the under-surface tetrahedral term. Furthermore we have included nearest-neighbour interactions between superficial sites, between under-superficial sites, and interaction between under-surface and surface sites. Finally we have inserted second-neighbour interactions, which results to be interaction between sites of the same kind. A schematic representation of the interaction is represented in figure 4.8. Nearest-neighbour interaction have been the most tricky to model properly, as they are quite strong, repulsive and non-linear with respect to the number of neighbours; e.g. the repulsion that one FCC Hydrogen feel from *each* of its nearest-neighbour HCP Hydrogen depends on the number of the latter.

The estimation of the interaction terms have been obtained from about twenty DFT calculations. Each configuration was based on a $2 \times 2$ surface supercell designed to simplify the extraction of a single parameter. They were then tested on about ten more complex configurations, again in a $2 \times 2$ cell; we have found very small errors (up to 5 meV per Hydrogen atom) in the less crowded cases, up to 4 Hydrogen per cell, but more consistent errors (up to 30 meV per Hydrogen atom) in the relatively more crowded cases, up to 8 Hydrogen per cell, where the importance of neighbours repulsion terms increases with respect to on-site

terms. In the very crowded cases out simplified model cannot be considered reliable, as it allows for Hydrogen atoms to stay in impossible position, that in reality, would cause the formation and desorption of an $H_2$ molecule. Nevertheless, as we will see in the next section, the system is actually in a low-coverage state at the experimental conditions.

We have computed the necessary terms for both a normal Palladium surface and for the surface of a Palladium-Hydrogen crystal in the $\beta$ phase, as specified in section 4.1.1. Even if the geometry is the same, the relative magnitude of on-site energies and neighbour interactions is quite different between the two systems. In expanded Palladium binding energies are higher and second-neighbour repulsions are generally weaker. On the other hand, because diffusion barriers reduce it becomes tricky to estimate the energy of under-surface sites; the local minimum associated with under-surface site become very flat and swallow, requiring an accurate initial guess t prevent their migration to the surface. Notwithstanding this problem we could collect the necessary data to accurately describe the system; the values are reported in figure 4.8.

### 4.2.3 Grand-canonical Monte Carlo simulation of Hydrogen Surface Adsorption

The elements that define the characteristics of the Palladium-Hydrogen surface are the temperature, the chemical potential of Hydrogen and the configuration energy of adsorbed Hydrogen. The temperature is easily established, as it is defined by the experimental condition. The chemical potential must be equal to one of the gas phase, which we have computed in section 3.2.1. Finally, we computed the configuration energy using the energy terms listed in the previous section. These three ingredients are sufficient for a Grand-Canonical Monte Carlo (GCMC) simulation structured according to the following steps:

1. The surface is initialized including a certain number $S$ of surface and the characteristic energy terms;
2. The surface is initially populated with a random distribution of Hydrogen atoms and the total energy of this initial trial system, called $E_{\text{old}}$, is computed;

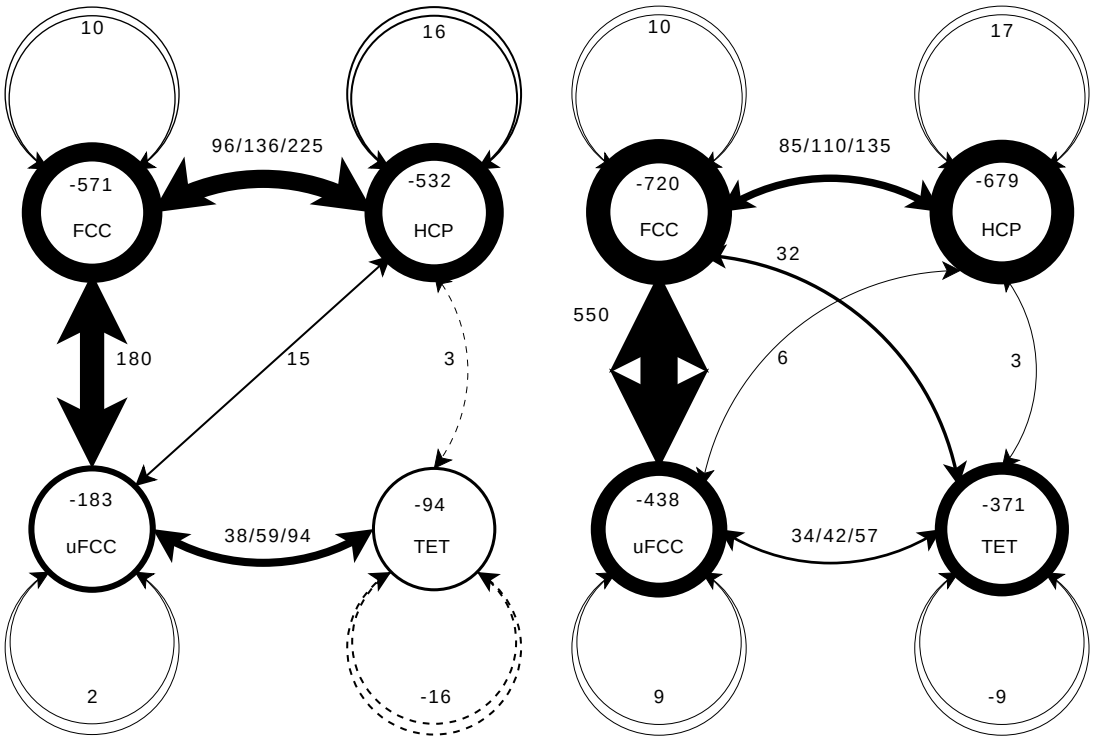


Figure 4.8: Diagrammatic representation of on-site energies and inter-site interaction for the normal Palladium structure (left) and for Palladium in the $\beta$ phase (right). Circles represent the possible adsorption sites, their thickness is proportional to on-site energy (reported in meV). Arrows represent interaction between sites and are labelled with the pair-wise interaction energy, their thickness is proportional to the energy, lines are dotted if the interaction is attractive; double-lines are used for second-neighbours (up to 6), while single lines connect nearest-neighbours (up to 3); when the pair-wise interaction depends on the number of neighbours all the values are specified and thickness is proportional to the average.

3. A random site is selected, and its state is switched; i.e. if it was occupied it is freed and the other way round; then the energy for the new configuration $E_{\text{new}}$ is computed; this procedure corresponds to a MC move;

4. The acceptance rate of a move is computed according to:
   $a = \min\left(\exp(-\beta(E_{\text{new}} - E_{\text{old}} - \delta N \mu_g)), 1\right)$ ;
   where $\delta N$ is $+1$ if a Hydrogen atom is added and $-1$ if it is removed, $\mu_g$ is the gas-phase chemical potential of Hydrogen.

5. If the move is accepted $E_{\text{old}}$ is updated with the value of $E_{\text{new}}$, otherwise the surface is restored to its previous condition

6. The value of $E_{\text{old}}$ is stored to compute the average system energy, at the end of the simulation;

7. The algorithm is repeated from step 3 for a large number of iterations.

A peculiar characteristic of GCMC, with respect to other Monte Carlo flavours, is that the chemical potential $\mu$ is imposed, while the number of particles is fluctuating. This allows to sample the average Hydrogen populations when the system is put in contact with an reservoir, in our case the gas phase, which has a constant and well-defined chemical potential.

We used a supercell of size $50 \times 50$ surface unit cells, containing 10000 possible adsorption sites, 2500 of each kind. We checked by looking at the average Hydrogen population, that the system can normally reach equilibrium in a few hundred thousand iteration with the exact number depending on the quality of the initial guess. To stay on the safe side, we allowed the system to thermalize for the first 2 million MC steps before starting to sample. The convergence of the GCMC method becomes problematic at high values of $\mu$, or in general where coverage is very high, because of the low insertion probability; this well-know problem can be avoided using more sophisticated techniques, such as Configurational Bias GCMC [74]. We can safely ignore it as we are only interested in the low-$\mu$ region; however it can be dealt with in case one wishes to explore the high-coverage region. The results of the simulations are represented in figure 4.9. The fraction of occupied sites is plotted as a function of the gas chemical potential, both for the normal Palladium surface and for the surface of proton-enriched Palladium.

As for the bulk it is not possible to give a precise quantitative estimation of the cell potential effect on the chemical equilibrium; furthermore the dependence of surface sites occupation on the chemical potential of Hydrogen is very steep in the area we are interested in. However, as we will later see in chapter 5, what is important in our model is to have a good fraction

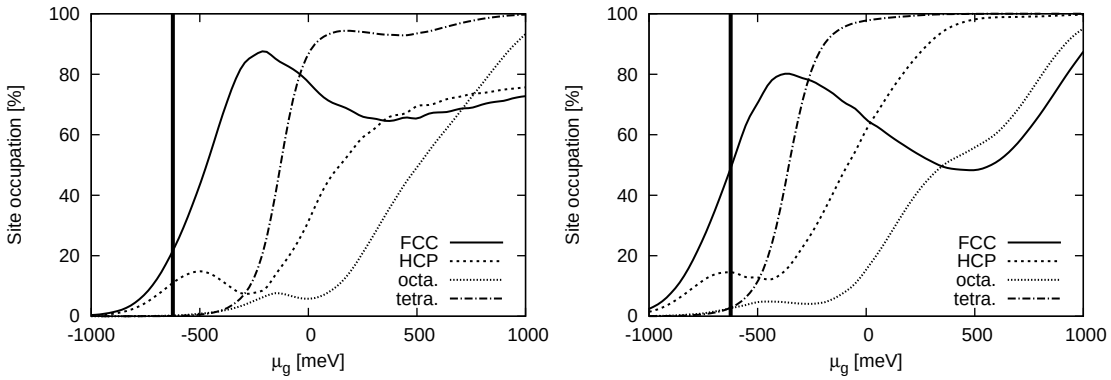


Figure 4.9: Surface and under-surface site occupancy for normal Palladium (111) surface (left) and for the same surface of proton-enriched Palladium. The vertical line at about $-600$ meV is the chemical potential of $\frac{1}{2}H_2$ in the gas phase.

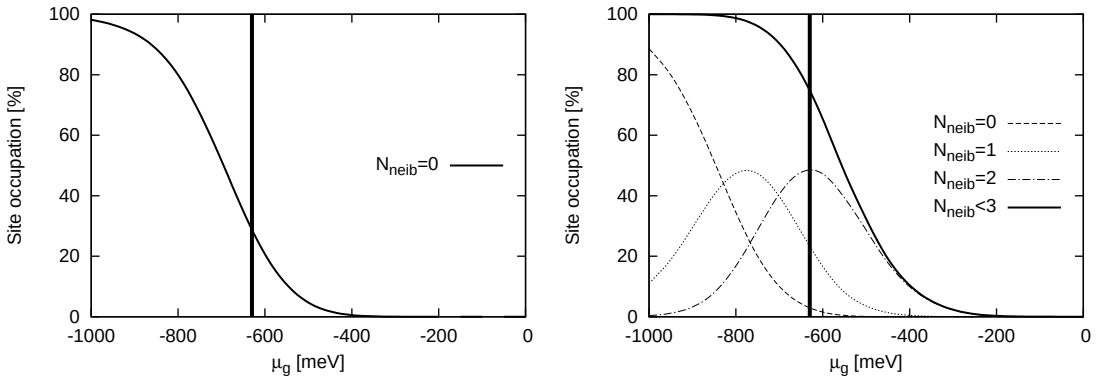


Figure 4.10: Average number of Hydrogen atoms attached to each Palladium during the MC run; the dotted curve represent the fraction of Palladium which are no more suitable for Nitrogen.

of free superficial Palladium atoms, to allow the physisorption of $N_2$. As long as the total coverage remains well under one monolayer this condition is met. As a further reassurance we have also sampled the average number of Hydrogen atoms attached to each surface Palladium atom during the GCMC run; the results are presented in figure 4.10. As we will see, a Palladium atom is considered "free" from the point of view of $N_2$ if it has no Hydrogen atoms attached, in the case of normal Palladium, or up to 2 Hydrogen atoms, in the case of proton-enriched Palladium.

# Chapter 5

# Production of Ammonia on a Proton-enriched Palladium Catalyst

*In this chapter we will present some novel results regarding the production of Ammonia on a Palladium catalyst enriched with a high percentage of bulk-adsorbed Hydrogen; more details about the catalyst structure are described in chapter 1. In the first section we will see the mechanism of molecular Nitrogen adsorption on the surface and the possibility of its dissociation. In the next sections we will instead explore the possibility of Nitrogen Hydrogenation prior to its dissociation, we will analyze a number of possible intermediate steps focusing on their structures and energetics. Finally we will study the reaction barrier of the possible rate-limiting step using the NEB method from section 3.4.*

## 5.1 Methods Used

The results presented in this chapter are the result of extensive numerical simulation performed in the framework of Density Functional Theory (sec. 2.2). The calculations have

Table 5.1: Cutoff radii (in atomic units) and reference energies (in Rydberg, where the eigenvalue $\varepsilon_{nX}$ was not used) used to generate the PAW dataset employed in the present work. $^\star$: the atomic wavefunction has been used to construct the local potential. $^\dagger$: local potential constructed from the all-electron one according to Troullier-Martins recipe [78].

| Hydrogen | | | Nitrogen | | | Palladium | | |
|---|---|---|---|---|---|---|---|---|
| | $r_{cut}$ $(a_0)$ | $\varepsilon_{ref}$ | | $r_{cut}$ $(a_0)$ | $\varepsilon_{ref}$ | | $r_{cut}$ $(a_0)$ | $\varepsilon_{ref}$ |
| $1s$ | 1.17 | $\varepsilon_{1s}$ | $2s$ | 1.32 | $\varepsilon_{2s}$ | $5s$ | 2.30 | $\varepsilon_{5s}$ |
| $1s$ | 1.17 | 0.05 | $2s$ | 1.32 | 0.05 | $5s$ | 2.30 | 0.50 |
| $2p^\star$ | 0.85 | 0.00 | $2p$ | 1.52 | $\varepsilon_{2p}$ | $5p$ | 2.30 | $\varepsilon_{5p}$ |
| | | | $2p$ | 1.52 | $-0.05$ | $5p$ | 2.30 | $-0.10$ |
| | | | $3d^\star$ | 1.10 | 0.15 | $4d$ | 2.30 | $\varepsilon_{4d}$ |
| | | | | | | $4d$ | 2.30 | $-0.25$ |
| | | | | | | $V_{loc}{}^\dagger$ | 2.00 | |

been performed using the Quantum-ESPRESSO distribution [28], which is capable of performing DFT simulations on a plane-wave basis; the distribution also includes a wide choice of post-processing tools for the analysis of the data.

We have chosen to use the Perdew-Burke-Ernzerhof (PBE, [64]) approximation for the exchange and correlation functional (sec. 2.2.4) which we believe can describe effectively both the metallic catalyst and the molecules involved in the reaction. Other functionals, especially the semi-empirical ones such as BLYP [44], have been proved to predict more accurately binding energies and geometrical properties for molecular systems; on the other hand they usually give poor results when used for metals and, more in general, for system where electrons are substantially delocalized [58].

We have decided to model the atoms of our system using PAW datasets (sec. 2.3) constructed to be as accurate as possible without being excessively computationally expensive. The characteristics of these datasets are summarized in table 5.1.

## 5.2 Nano-scale Structure of Palladium Catalyst

We have modeled the catalyst according to our results from sections 4.1.1 and 4.2.2; i.e. we have considered the Palladium bulk to be in the $\gamma$ phase, populated with roughly 50% Hydrogen per Palladium atom in the tetrahedral site. As a consequence the lattice constant is increased by about 3.5% with respect to a pure Palladium crystal.

We have modeled the surface using a surface-slab model composed of 4 asymmetric atomic layers; the atoms in the bottom layer are fixed into their positions and are not allowed to relax; then three layer of free Palladium atoms alternate with layers of Hydrogen, positioned in the tetrahedral sites. Since we have increased the surface cell lattice constant, if a realistic amount of under-surface Hydrogen atoms is not inserted, the relaxation would tend to compensate squeezing the layers close together.

In order to allow enough room for the adsorption of the molecules involved in the reaction we have constructed a $2 \times 2$ supercell containing a total of 16 Palladium and 3 under-surface Hydrogen atoms which will be the base structure of our model catalyst; the structure is depicted in figure 5.1. The under-surface atoms are placed initially in the tetrahedral site, but the position of the more superficial one vary considerably when other chemical species are inserted in the simulation.

In addition to the under-surface Hydrogen we added a certain coverage of surface Hydrogen. It can be either in the HCP or in the FCC site as the energy difference is very small; the Monte Carlo simulation we have performed in section 4.2.3 predicts a coverage of half monolayer for the FCC sites and 15% monolayer for the HCP ones. Clearly this situation cannot be exactly reproduced in a $2 \times 2$ supercell where there are only 4 adsorption sites of each kind. We have have decided to put at most two Hydrogen atoms on the surface, one in the FCC site and one in the HCP site. This choice leaves one of the Palladium atoms on the surface with no Hydrogen attached to it and yet contains enough Hydrogen atoms to study three subsequent reaction stages.

When all the surface sites are occupied, Nitrogen molecules cannot attach to the catalyst.

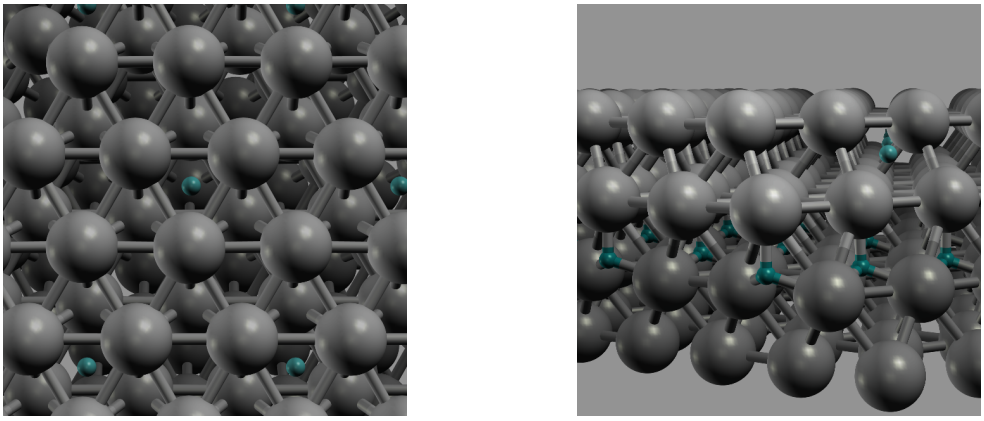

Figure 5.1: Structure of model used to study the catalyst surface; 4 layers of Palladium and two layers of under-surface Hydrogen are included, the bottom layer is kept fixed while the others are free to relax.

$N_2$ molecules still feel a weak bond but only stabilize at a large distance, more than 3 Å. We have observed that $N_2$ can only attach stably on Palladium atoms that have less than three Hydrogen atoms attached to them, either on the surface or under the surface; more specifically when the Palladium atom is coordinated to no more than one Hydrogen atom, the adsorption energy is low but significative (about 0.26 eV) while it is of only a few meV in the other cases. However, as we have seen in section 4.2.3 (see figure 4.10) the fraction of Palladium atoms available for Nitrogen adsorption is very consistent.

## 5.3 Adsorption and Dissociation of Nitrogen

The triple bond that keeps a Nitrogen molecule together is one of the strongest chemical bonds in nature: molecule's binding energy is about 10 eV. In the gas phase dissociation of Nitrogen is negligible even at very high temperature, and even on the best industrial catalysts used in the Haber-Bosch process a temperature of at least 500°C is required to break the adsorbed molecule. Furthermore, Palladium is not a very reactive metal and it is definitely not a good catalyst for this particular purpose. In spite of this the specific experimental conditions could modify the characteristic of Palladium surface enough to

allow for dissociation of Nitrogen.

To verify or falsify this first working hypothesis we have computed the adsorption energy for Nitrogen molecules and atoms. A Nitrogen molecule prefers to adsorb on the on-top site, oriented vertically at a distance of 2.07 Å over the underlying Palladium atom; its structure remains mostly unchanged and the N−N distance only increase by about 0.7% with respect to the gas phase. The favourite adsorption site for atomic Nitrogen is the threefold site, its distance from the three surrounding Pd atoms is 1.91 Å, while its height over the surface plane is of 1.64 Å.

The adsorption energy of Nitrogen molecules on Palladium is quite low, especially if compared with more reactive metals; as we have seen in the previous section, it accounts for about 0.26 eV. On the other hand adsorption of atomic Nitrogen on the same surface is quite stable compared to the energy of an *isolated* Nitrogen atom, its binding energy accounts for about 3.59 eV of the systems total energy; nevertheless it is still 1.60 eV from the energy of $\frac{1}{2}N_2$. As a consequence, and without even keeping into account any additional barrier which may be present, dissociation of Nitrogen on the enriched Palladium catalyst will still cost more than 3.19 eV. According to transition state theory this corresponds to about one dissociation every several second, even at a temperature of 1000 K, assuming a typical frequency prefactor of $10^{11} - 10^{12}$ Hz.

### 5.3.1 Importance of Surface Defects

As we have seen in the previous section Nitrogen does not bind tightly to Palladium, even when it is in the proton-enriched phase, because of the relative inertness of the metal. However catalyst atoms located at surface defects have a lower coordination number, which normally makes them more reactive. In order to examine this effect we have repeated the calculation of Nitrogen adsorption energy for two vicinal surfaces of Palladium (111); namely the (331), exposing the (111) step and the (311), exposing the (100) step. The stepped geometries are represented in figure 5.2.

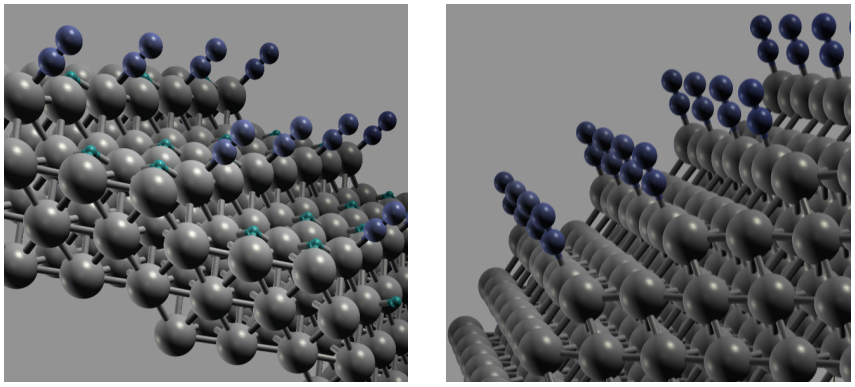

Figure 5.2: Vicinal surfaces of Palladium (111): on the left the [111] step and, on the right, the [100] step.

We found that step Palladium atoms are actually more reactive than the surface ones; the adsorption energy can increase up to 0.58 eV for [111] step and up to 0.50 eV for [100] step. Nevertheless the probability of direct $N_2$ dissociation remains negligible and the character of the adsorption does not change qualitatively. For this reason we have decided to use a normal flat-surface geometry for our calculations, which is less computationally expensive, and only consider the possible effect of surface defects qualitatively when analyzing the results.

## 5.4 Hydrogenation of Molecular Nitrogen in the Gas Phase

After having verified that dissociation of Nitrogen is unlikely to occur on the Palladium substrate, we moved to study the possibility of direct Hydrogenation of the $N_2$ molecule prior to dissociation. There are both experimental studies [77] and DFT calculations [68] suggesting that Hydrogenation of $N_2$ can happen in the process of Ammonia production catalyzed by biological enzyme. In particular on the active site of the nitrogenase enzyme known as FeMoCo [68] which is a $MoFe_6S_9$ complex. What the biological process have in common with our study is that Ammonia production happens at ambient pressure and does not even require high temperature, conversely the necessary energy is provided by hydrolysis

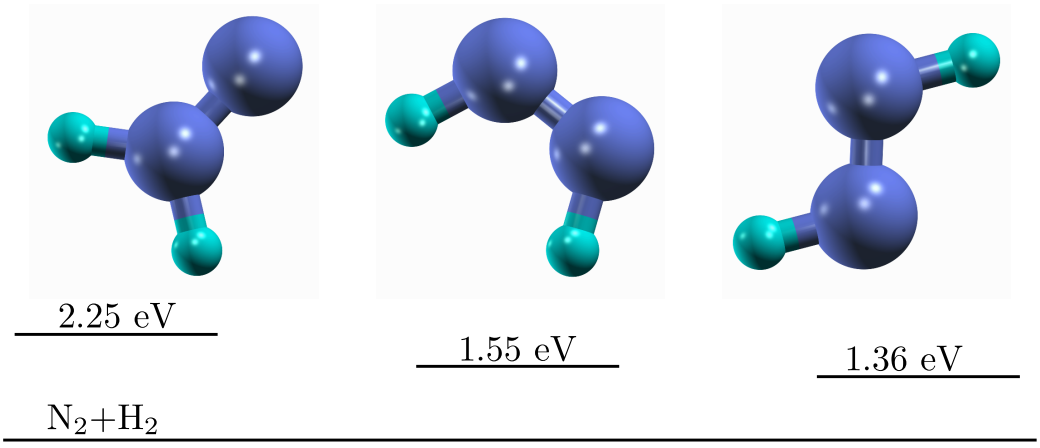


Figure 5.3: Possible configuration in the gas phase for the $N_2H_2$ molecule and their binding energy with respect to isolated $N_2$ and $H_2$ molecules; unnamed asymmetric molecule (left), cis-diazine (center), trans-diazine (right).

of Adenosine triphosphate molecules. The authors of the DFT study go as far as to suggest that the biological process could be artificially reproduced providing the necessary energy by electro-chemical means.

In order to verify if such a process is possible for our system we have computed the ground-state energy of several different kinds of Nitrogen-Hydrogen molecules. The molecules are formed by two Nitrogen atoms and an increasing number of Hydrogen atoms up to 6, when spontaneous breaking of the molecule in two Ammonia is inevitable. The first stage of research involves computing the possible molecular configurations in the gas phase; of these only a few are found in nature, namely Diazine, $N_2H_2$ which can be in a *cis* or *trans* configuration and Hydrazine $N_2H_4$. Geometrical structure and basic information about these molecules are summarized in figures 5.3 and 5.4. While cis-Diazine can easily decompose back into Nitrogen and Hydrogen, trans-Diazine has to change to cis before decomposing; on the other hand 3 Hydrazine molecules decompose to one $N_2$ and four Ammonia, even at low temperature, on several kinds of catalysts [16].

Based on this qualitative observation we can expect that if Hydrogenation of Nitrogen can reach the Hydrazine stage then its decomposition into Ammonia will be very likely, while

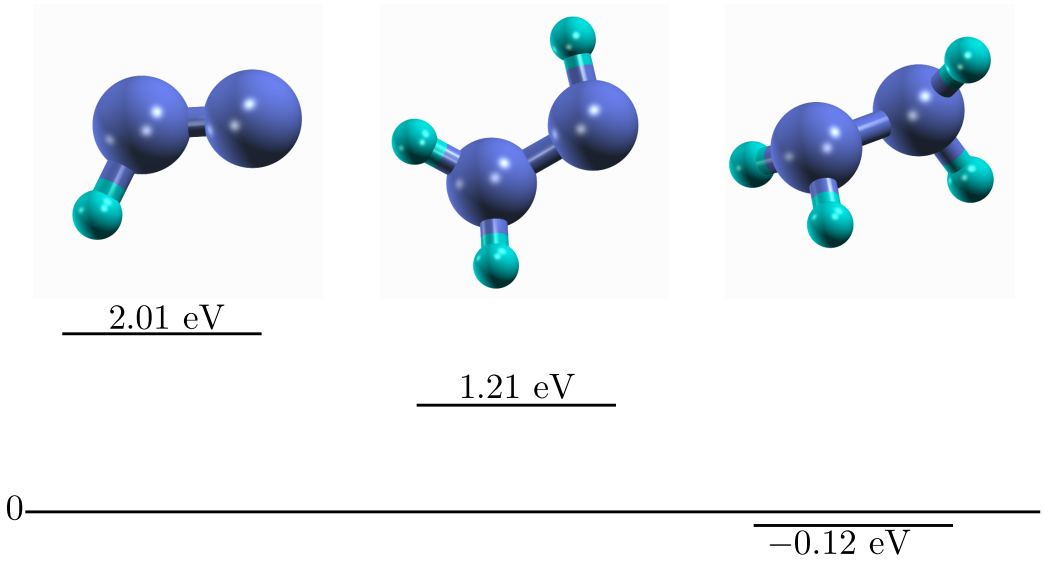


Figure 5.4: More Hydrogenated Nitrogen molecules, as they have different number of Hydrogens the binding energies, computed w.r.t. $N_2$ and the opportune amount of $\frac{1}{2}H_2$, should not be used to derive chemical balance. From left to right: $N_2H$; the most stable form of $N_2H_3$; Hydrazine $N_2H_4$.

the first few Hydrogenation can be more problematic due to the high absolute energy of this species with respect to their constituents. In the next section we will see how the Hydrogenation mechanism can proceed on the catalyst surface.

## 5.5 Hydrogenation of Adsorbed $N_2$

There are many possible intermediate configurations starting from the initial one, i.e. $N_2$ adsorbed on the Palladium surface, to the final production of Ammonia. Since the number of Hydrogen required to form 2 Ammonia molecules is too large to be included in a supercell small enough to keep the computational cost acceptable, the different stages of the process have to studied using systems with different number of atoms. This condition makes it impossible to list the energies of all the intermediate states on a common reference scale. Nevertheless, most of the meaningful configurations are quite consistent with respect to the addition of one or two Hydrogen atoms adsorbed on the surface; it is then possible to

compare subsequent stages building a piece-wise diagram of the complete reaction.

Before going into further detail on the overall process we need to examine more closely the intermediate steps, in particular the different stable configurations that can appear after each subsequent Hydrogenation.

### 5.5.1 Reference Surface and Adsorption of $N_2$

Our reference surface will always be the $2 \times 2$ supercell as described in section 5.2. It is not necessarily the most likely surface configuration, as it only contains Hydrogen atoms both in the FCC and HCP surface sites, but we can expect, from the Monte Carlo simulation, a sensible fraction of the catalyst surface to be in this configuration. Supercells with more superficial Hydrogen as well as supercells with all the Hydrogen in the FCC or in the HCP site have a much smaller binding energy for the Nitrogen; on the other hand if we include only one adsorbed Hydrogen in the supercell it becomes impossible to compare more than two subsequent Hydrogenation steps. Furthermore the MC simulation of section 4.2.3 indicate, at the experimental conditions, an occupation of about 50% of the FCC sites and 15% of the HCP sites, of course this cannot be reproduced exactly in a $2 \times 2$ supercell.

The favourite site for $N_2$ adsorption is on top of a Palladium atom, while the binding energy depends considerably on the number of Hydrogens bound to the Palladium atoms. With no Hydrogen neighbours this energy is of 0.26 eV while for one neighbour it decreases to 0.12 eV, finally for 2 neighbours it decreases further to 0.02 eV. Some adsorption configurations are presented in figure 5.5

Concluding this section we want to give an estimate on the number of $N_2$ that we can expect to be adsorbed on the catalyst at the experimental conditions. In the experiments the surface of the catalyst was estimated to be of about 80 $cm^2$ for the double-chamber reactor and of about 60 $cm^2$ for the single-chamber reactor (sec. 1.2). As we are only interested in an order of magnitude we will just take 100 $cm^2$; the surface cell has an area of 7.23 $Å^2$, which corresponds to about $10^{17}$ surface Palladium atoms. We can expect most

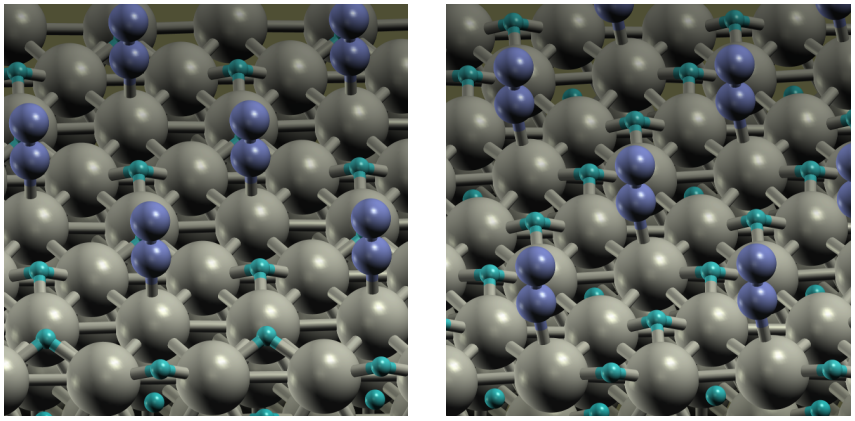

Figure 5.5: Adsorption of $N_2$ in the on-top site on the catalyst surface depending on the number of Hydrogen surrounding the Palladium: from left to right none, one, two. It can be seen how the Nitrogen molecule tends to move from the center of the under-lying Palladium to increase its distance from the Hydrogen. The Pd−N distance is 2.07 Å and 2.12 Å; the N−N distance is 1.12 Å in both configurations.

of the sites to be suitable for adsorbing an $N_2$ molecule. Furthermore we have to take into account the chemical potential of the Nitrogen gas which is of $-2.12$ eV at the experimental temperature and pressure. Combining all these data together we can get our estimate for the coverage $\theta_{N2}$ and the number of adsorbed $N_2$ molecules:

$$\theta_{N2} = e^{-\frac{(\varepsilon_b - \mu_g)}{k_B T}} \; ; \; N_{N2} \simeq f_{\mathrm{Pd}} \frac{S_{\mathrm{cat}}}{S_{\mathrm{cell}}} \theta_{N2} \tag{5.1}$$

Where $S_{\mathrm{cat}}$ and $S_{\mathrm{cell}}$ are the surface areas of the catalyst and of the surface unit cell, $f_{\mathrm{Pd}}$ is the fraction of available Palladium atoms, about 80%. The exponential accounts for the chemical equilibrium between the gas and the surface, at low coverage. Inserting the numbers we get $\theta_{N2} \sim 10^{-11}$, which correspond to about $10^7$ $N_2$ molecules adsorbed at any time on the catalyst surface. We wish to remark that this is only a very rough estimate, probably less precise than an order of magnitude; it depends dramatically on the adsorption energy of $N_2$, about one order of magnitude for a 0.20 eV shift.

To conclude this section we wish to compare this results with similar results for a non-proton enriched Palladium surface. We have found that on clean normal Palladium the adsorption energy of $N_2$ is only slightly lower than on clean proton-enriched one, on the other hand

a single Hydrogen attached to the same Palladium does cause the configuration to become unstable and the Nitrogen molecule to desorb. Under this conditions, the expected coverage of Nitrogen on Palladium is about a factor 10 smaller than for proton-enriched Palladium.

### 5.5.2 Reference Energy for Hydrogen Atoms

As we have anticipated, during the subsequent Hydrogenation stages we will need to add additional Hydrogen atoms to the simulation cell. As a consequence, in order to compare subsequent stages with different number of atoms, we need to choose a reference energy for a single Hydrogen atom. A common choice is to take half the energy of an isolated $H_2$ molecule. However, in our case, Hydrogen is coming from the bulk where it is slightly more stable than in an $H_2$ molecule, about 0.05 eV per atom. Referring to this energy would be an equally valid, and possibly more significant, choice. Finally, we can estimate the adsorption energy of the Hydrogenated Nitrogen-based specie with respect to its own energy in the isolated stage, i.e. the adsorption energy, with respect to a surface with the same number of adsorbed Hydrogen atoms, of the species we have listed in section 5.4.

In order to give an overview as complete as possible, we will state both the adsorption energies of the specific $N_2H_X$, which gives an idea of the configuration stability, and the energy with respect to $N_2$ plus an appropriate amount of Hydrogen atoms assuming they are coming *from the Palladium bulk*, which gives an idea of the overall progress of the reaction and the reaction barriers. To avoid confusion we will indicate the adsorption energies of the molecules as absolute sign-less numbers, e.g. 0.50 eV; the "absolute" energy with respect to the constituents, $N_2$ and bulk-adsorbed H, with always be written with the sign, even if it is positive, e.g. +0.50 eV.

We are never going to directly compare the energies of different species from calculations performed with different number of atoms; hence the physically relevant quantities such as adsorption energy and reaction barriers will be independent from the choice of reference.

### 5.5.3 First Hydrogenation

The first step of the Hydrogenation process is also the most critical one as we will shortly see in detail; the adsorption energy of Hydrogen is quite high while the binding energy of isolated $N_2H$ is very low, hence a strong bond between N and Palladium is required to have a reasonably stable configuration.

If the Hydrogen atom is initially set on the Nitrogen closer to the surface it cannot find a stable configuration and spontaneously moves to the surface, without meeting any significant barrier. On the other hand if the Hydrogen stays on the Nitrogen more distant from the surface there are two possible stable configurations. In the first and more stable one, the Hydrogen stays between the Nitrogen and the Palladium. In this configuration the Hydrogen and the Palladium atom attached to the Nitrogen molecule stay on the same side of the molecule, in a way similar to cis-diazine. For this reason we will call this configuration *cis*. The other, less stable configuration, has the Hydrogen atom attached on top of the Nitrogen, further away from the surface; we will refer to this configuration as *trans*. In both cases the N−N axis of $N_2H$ molecule is not vertical but tilted at an angle of about 60° with respect to the vertical. The two configurations are presented in picture 5.6 and some additional details on the adsorption geometry are listed in the caption.

Energetically the trans configuration is favoured over the cis one by 0.28 eV. The absolute energy of the two species are +1.56 eV for cis and +1.33 eV for trans. The adsorption energy of $N_2H$ is 0.77 eV for the trans geometry and 0.99 eV for the cis one: even though the absolute energy is way higher than for $N_2$, $N_2H$ is attached more firmly to the surface. When we add one more Hydrogen atom to the surface the absolute energy of cis configuration decreases to +0.82 eV and its adsorption energy increases to 1.19 eV.

Provided that the energy for $N_2$ is −0.26 eV, we can estimate the minimum possible energy barrier for the first Hydrogenation as $E_{\text{trans}} - E_{N2}$ which gives 1.59 eV. The actual barrier can be higher than this, to estimate it we have used the NEB method (sec. 3.4) to simulate the path of the Hydrogen atom from the Palladium surface to the top of the Nitrogen molecule. We could not found any barrier, although one must be present to ensure stability

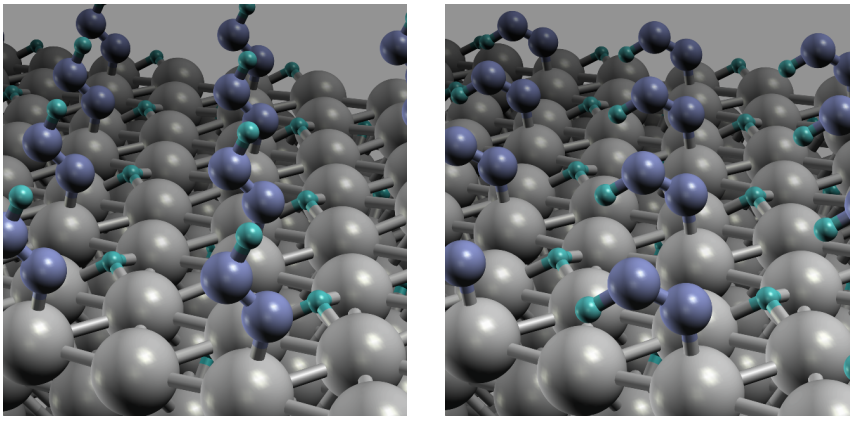

Figure 5.6: Possible configurations for $N_2H$ molecule adsorbed on the Palladium surface. On the left: the more stable *cis* configuration; on the rigs the less stable *trans* configuration. In both cases the N–N distance is about 1.21 Å, 0.02 Å *less* than for isolated $N_2H$. The Pd−N−N angle is slightly less than 130°.

of the final configuration; the barrier may be too low or too close to the final state for the NEB method to find it. We have studied the stability of the final configuration in a short run of DFT-based Born-Oppenheimer molecular dynamic simulation. The Hydrogenation process is presented in fig. 5.7 aside with its energy profile.

We can use Transition-State Theory (sec. 3.3) to estimate the reaction probability, the reaction rate $k$ is defined as in equation 3.26:

$$k = \frac{1}{2\pi} \frac{\prod_{i=1,3N} \omega_i(q^{IS})}{\prod_{i=1,3N-1} \omega_i(q^{TS})} e^{-\beta\delta E} \,. \tag{5.2}$$

The exponential term is $\sim 1 \times 10^{-8}$, while the vibrational-frequency term is normally in the order of $10^{11} - 10^{12}$ Hz; predicting between one thousand and ten thousands Hydrogenations per adsorbed Nitrogen per second.

A critical point of the first Hydrogenation step is that it has to be favoured with respect to, or at least competitive with, the recombination and desorption of Hydrogen molecule. Hydrogen has no dissociation barrier on Palladium, hence its desorption barrier is just twice the binding energy of and Hydrogen atom on Palladium surface. We have compute it to be about 1.44 eV which, although lower, is comparable with the Hydrogenation barrier. We

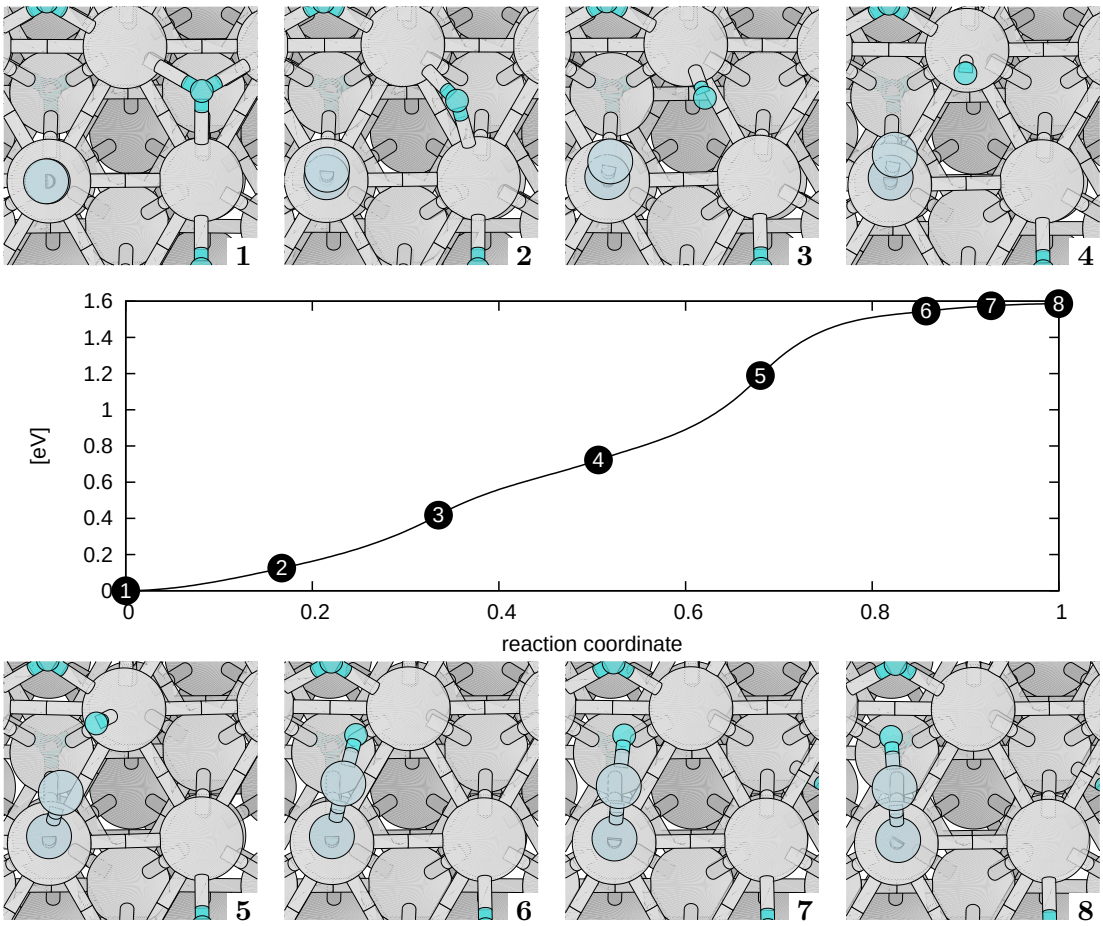


Figure 5.7: Reaction path for first Hydrogenation of $N_2$.

wish to underline how, in the non-proton enriched Palladium, the recombination barrier is substantially lower, about 1.14 eV. In general, a certain amount of Hydrogen will recombine and desorb, instead of combining with $N_2$; this is not a problem as, when it reaches a certain partial pressure it will equilibrate with the superficial one. Furthermore, in the single-chamber experiment, Hydrogen molecules that desorb can be actively recycled through the proton conductor.

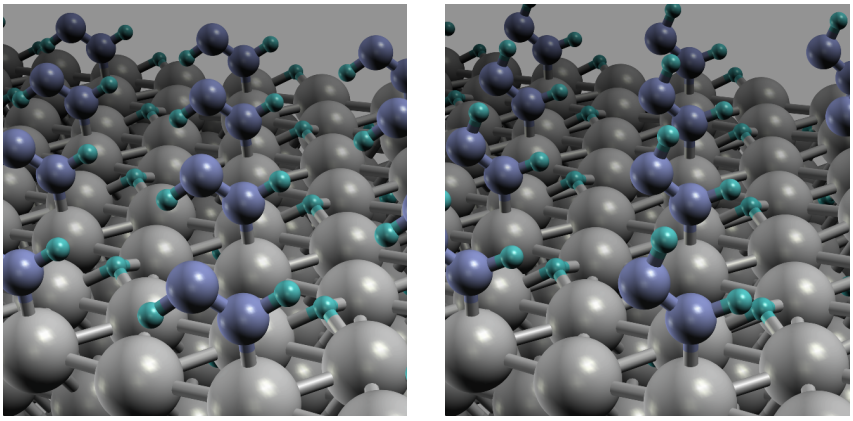

Figure 5.8: Possible configurations for $N_2H_2$ (diazine) molecule adsorbed on the Palladium surface with 2 Hydrogen atoms on the surface. On the left: the more stable *trans* configuration; on the right the less stable *cis* configuration. In both cases the N–N distance is about 1.26 Å, 0.01 Å *more* than for isolated $N_2H_2$. The Pd−N−N angle is slightly more than 130°. The Pd–N distance is larger 2.00 Å, 2.5% than for $N_2H$, which is consistent with a lower binding energy.

### 5.5.4 Second Hydrogenation

There are a few different configurations for adsorbed $N_2H_2$ which correspond to the gas-phase configurations we have seen in figure 5.3. We could not find any stable configuration when both the Hydrogen atoms are attached to the same Nitrogen, hence this possibility will be ignored in the rest of this section; what remains are a *cis* configuration, when both Hydrogen atoms are on the same side of the N–N axis, and a *trans* configuration, when they are on opposite sides. Furthermore, the Hydrogen atom attached on the lower Nitrogen atom can only stay on top of it, which reduces the possible stable configurations to two. This configurations are represented in figure 5.8 with additional geometrical details listed in the caption.

It appears from the geometrical characteristics how the two configurations are actually quite similar; nevertheless the difference in energy is significant, with the trans configuration being more stable by about 0.28 eV. The exact difference depends on the number of Hydrogen atoms adsorbed on the Palladium surface, but only by a few meV. It is interesting to

note how the energy difference between the two species is actually higher than for the isolated molecules, where it is of 0.19 eV; this means that the interaction with the surface is improving the selectivity of the trans specie which, incidentally, does not spontaneously decompose back to $N_2$ + $H_2$.

To avoid confusion, we wish to recall that the most stable form of $N_2H$ was the *cis* one, while now it is the *trans* one; notice however that trans-$N_2H_2$ is similar to cis-$N_2H$ with only one additional Hydrogen atom attached on the lower Nitrogen atom[1].

When there are no Hydrogen on the surface the adsorption energy is 0.63 eV for trans-diazine and 0.54 eV to cis-diazine, which correspond to an absolute energy of +1.08 eV and +1.36 eV respectively. As a comparison to the previous reaction stage, the diazine species are less bound to Palladium than $N_2H$, but their absolute energies are lower, indicating that the reaction is now proceeding downhill.

When we add one Hydrogen atom onto the surface the binding energies become 0.70 eV (trans) and 0.61 eV (cis) with respect to the gas-phase $N_2H_2$ molecules; while, the absolute energies further decrease to +1.08 (trans) and +1.36 (cis). We have also simulated the adsorption of trans-diazine with one additional Hydrogen, i.e. with two Hydrogen atoms on the surface; this configuration has an absolute energy of +0.93 eV.

From here on we will only consider the most stable trans state, which will be the *final* state of our reaction. The *initial* state will be the final state of section 5.5.3, i.e. the cis form of $N_2H$. When the $N_2H \rightarrow N_2H_2$ has to consume up the last available Hydrogen the energy difference between the initial and the final state is of 0.33 eV. On the other hand if we insert an additional Hydrogen in the cell the difference reduces to 0.15 eV, decreasing by more than half. We wish to recall that, as seen in section 4.1, Hydrogen adsorbed in Palladium has a very high mobility and a very low diffusion barrier making this process likely to happen on a shorter time-scale than the Hydrogenation.

Finally we have used the NEB method to estimate the Hydrogenation reaction barrier. The

[1] Also, cis-$N_2H_2$ is similar to trans-$N_2H$ with an additional Hydrogen atom attached on the lower Nitrogen atom, but as these are the least stable configuration we are not interested in it.

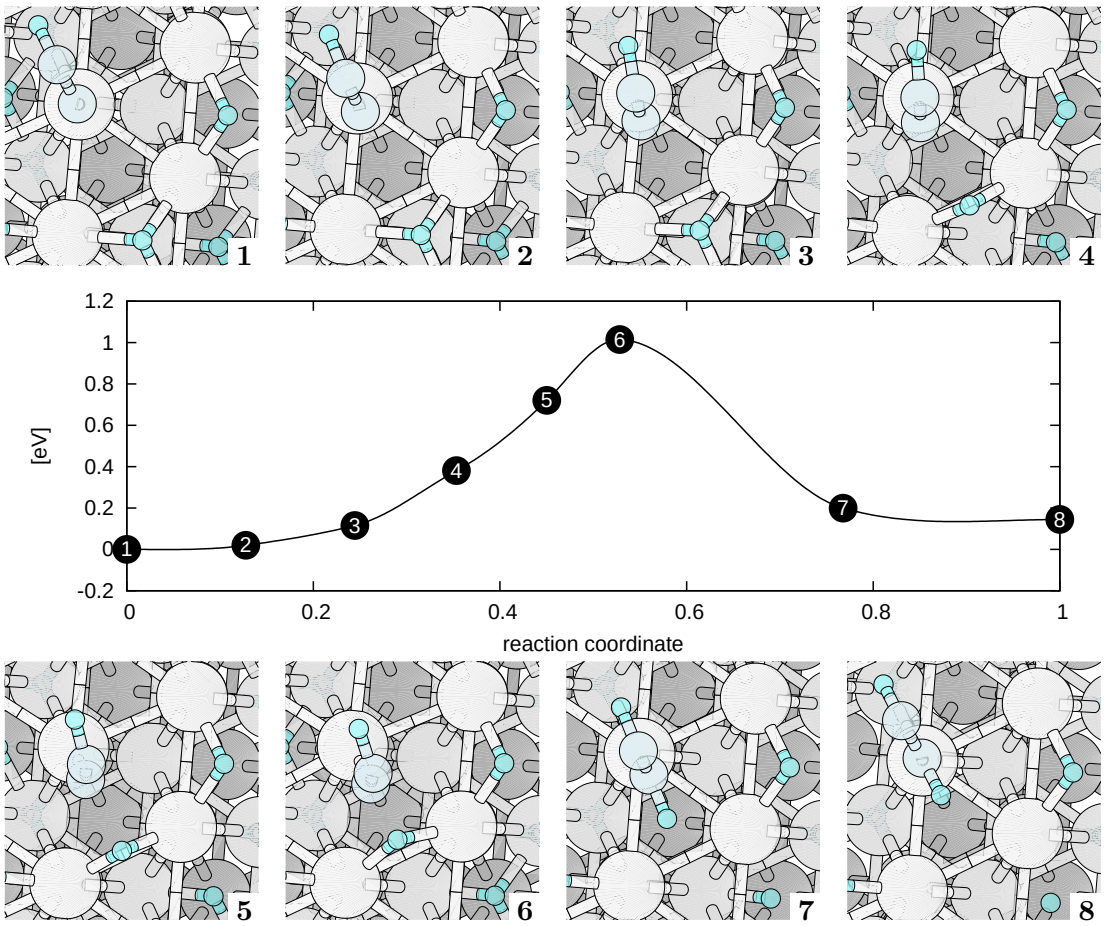


Figure 5.9: Reaction path for second Hydrogenation of $N_2$.

reaction path and its energy profile are depicted in figure 5.9; it is possible to see how the diazine molecule have to tilt on the side to reduce the N–H distance. The estimated energy barrier is of 0.99 eV, which is consistently lower than for the first Hydrogenation.

### 5.5.5 Third Hydrogenation

After the second Hydrogenation has occurred we have a trans-diazine molecule adsorbed on the catalyst surface. As in the previous cases there are several possible configurations that can result from the addition of another Hydrogen atom. The total number of hydrogen atoms in the simulation cell is again important, with an higher number favouring the more

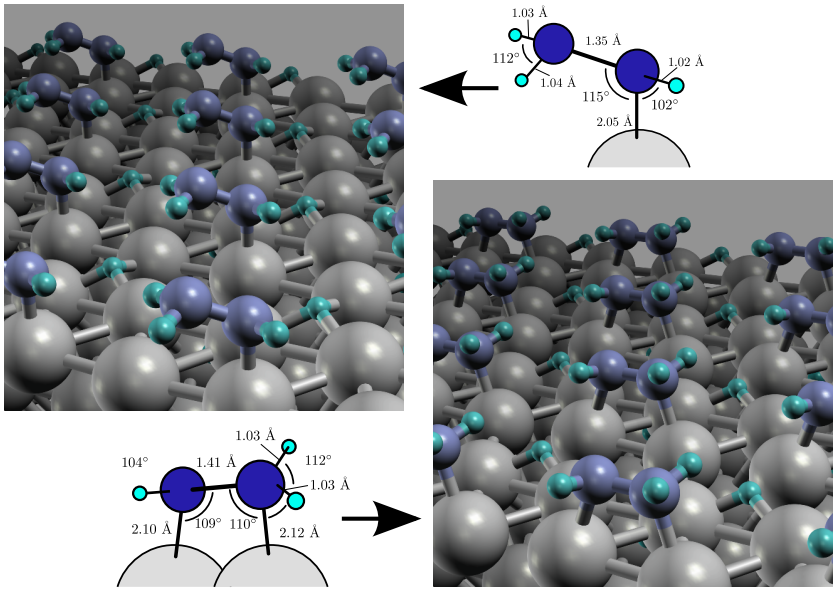


Figure 5.10: Possible configurations for $N_2H_3$ adsorbed on the Palladium surface with 2 Hydrogen atoms on the surface and their geometric parameters. In the rightmost configuration the N–N axis is almost parallel to the surface and the N–N distance has increased by $\sim 20\%$ w.r.t. the $N_2$ molecule.

Hydrogenated specie ($N_2H_3$) with respect to trans-diazine.

The only two stable adsorption configurations of $N_2H_3$ that we could find, are represented in figure 5.10. The binding energy of the most stable "horizontal" configuration of $N_2H_3$ on a clean proton-enriched Palladium surface is very high, about 3.93 eV, while its absolute energy is still +1.00 eV, with respect to $N_2$ from the gas phase and H from the bulk. For the least stable "vertical" configuration the adsorption energy is slightly lower, about 3.63 eV, while the absolute energy is +1.30 eV. Adding one or two Hydrogen atoms on the surface renders the "vertical" configuration unstable, making it spontaneously convert to the "horizontal" one. In these cases the binding energy is 3.73 eV (one Hydrogen atom) and 3.88 eV (two H atoms) while the absolute energies are +0.69 eV and +0.35 eV respectively.

At this stage the number of Hydrogen atoms attached to the $N_2$ molecule start to modify significantly its chemical structure. The least stable configuration still retain clear molecular characteristics: the N–N bond is already 18.6% longer than for gas-phase $N_2$ but the

molecule has a single bond to the surface. In the most stable configuration the N–N bond further elongates, reaching 1.41 Å, which is 22.1% longer than in gas-phase $N_2$, and 15.6% longer than in gas-phase trans-diazine.

In order to estimate the minimum energy path we have taken adsorbed trans-diazine as initial state; the final state will of course be the most stable configuration of 3-Hydrogenated Nitrogen. The energy difference of the two states is in general very small; the final state is favoured by 0.08 eV when there is only one surface-adsorbed hydrogen but disfavoured by 0.05 eV when an additional Hydrogen ad-atom is added. We have used the NEB method to compute a better estimate in the latter case. The reaction path is represented in figure 5.11; the barrier results to be 0.69 eV, although it could be marginally higher as we have not used the climbing image NEB feature in this case. It is quite low and not as sharp as in the previous stages of the reaction.

### 5.5.6 Final Hydrogenations and Production of Ammonia

After the first three Hydrogenations the reaction can proceed almost down-hill to the subsequent ones, until the N–N bond finally breaks. The $N_2H_4$ (Hydrazine) molecule itself is known to break spontaneously to form Ammonia even at temperatures lower than the experimental ones. In some biological ammonia-production reactions the breaking point is actually $N_2H_4$ [68, 77] which seems a reasonable option also in our case.

In the gas phase Hydrazine does not have any symmetry, but when adsorbed on Palladium the dihedral angles formed by the H–N pairs at opposite ends of the molecule changes significantly. On the other hand the angle formed by H–N–H on the same side of the molecule remains almost unchanged, at about 110°. Energetically the Hydrazine adsorbate is favoured over the $N_2H_3$ adsorbate; the energy difference of these two configurations depends on the number of Hydrogen atoms in the unit cell. It ranges from 0.13 eV, when there are no Hydrogen atoms adsorbed on the surface, up to 0.35 eV when an Hydrogen atom is added to the surface. On the other hand the adsorption energy of Hydrazine

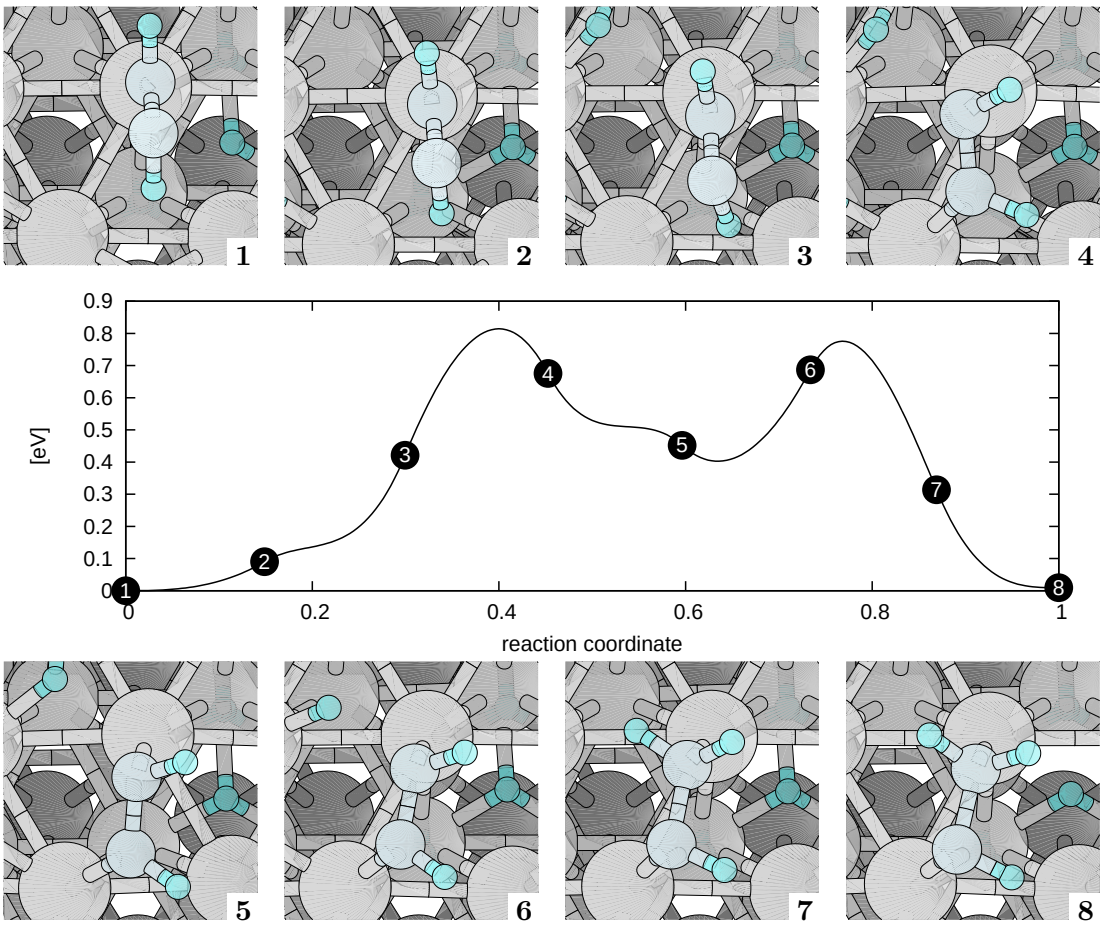


Figure 5.11: Reaction path for third Hydrogenation of $N_2$.

suddenly decreases to about 0.48 eV (on clean surface) and 0.53 eV (with one Hydrogen atom on the surface).

At this stage breaking the N–N bond starts to become more favourable; it is possible for $N_2H_4$ to break in two $NH_2$ molecules, each adsorbed in a bridge site. Another mechanism could be the simultaneous breaking of the N–N bond and Hydrogenation of one or both $NH_2$. This would immediately produce one or two Ammonia molecules, that can desorb to the gas phase without any significant barrier. It is difficult to say which path is preferred, it is also possible for both to happen in nature, with one mechanism being only slightly favoured over the other.

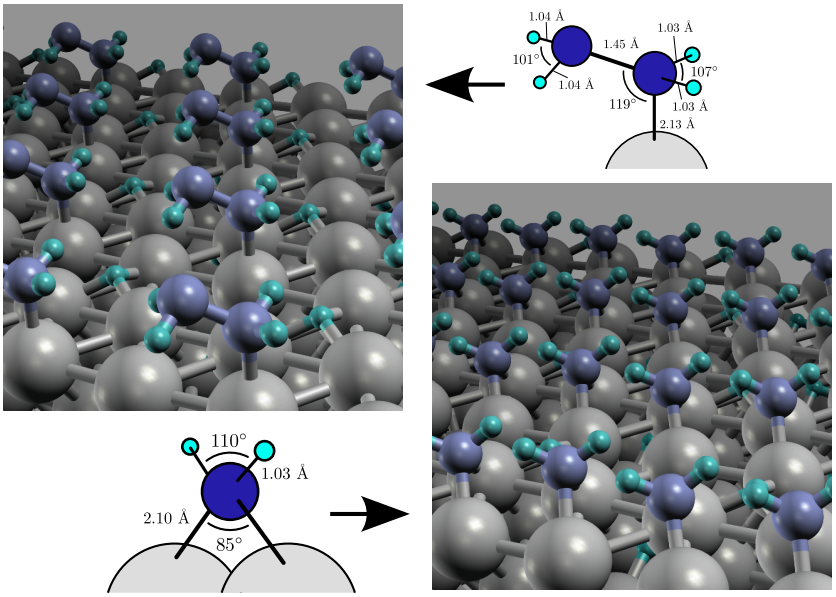


Figure 5.12: $N_2H_4$ (hydrazine) molecule adsorbed on the Palladium on-top site (left) and two $NH_2$ adsorbed in equivalent bridge sites (right).

We have tried to force additional Hydrogenation of the molecule, up to $N_2H_5$, but we found this specie to be extremely unfavoured with respect to Hydrazine, its chemical energy being about 0.580 eV higher. From this result we can state that more than 4 Hydrogenations, before N–N bound breaking, are very unlikely to happen; hydrazine is the more promising critical point where the N–N bond breaks and formation of Ammonia can finally occur.

## 5.6 Reaction Overview and Discussion

Having analysed each reaction step in detail we are going to recapitulate the entire proposed reaction path and re-examine the critical points from a wider angle. The reaction path is represented in detail in figure 5.13. Starting from adsorbed $N_2$ we immediately have the rate-limiting step, with a barrier of 1.59 eV; taking into account a typical vibrational frequency the reaction rate is comprised between $10^4$ Hz and $10^5$ Hz at 600 K, but can rise to $10^6$ Hz at 1000 K, the maximum temperature used in the experiments.

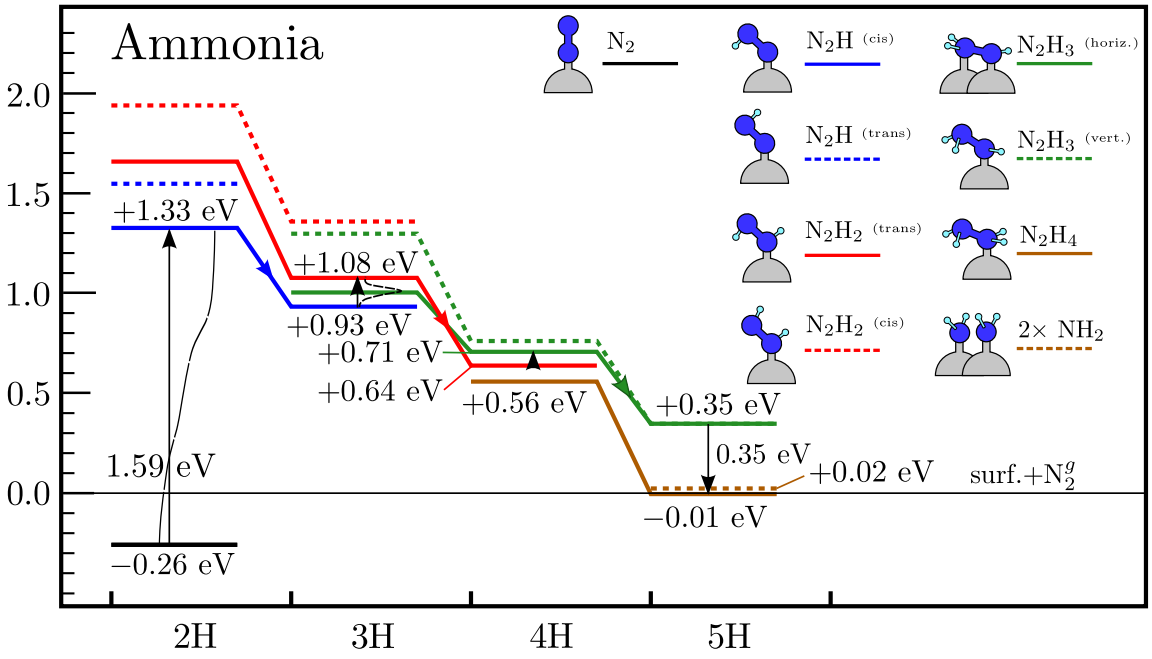


Figure 5.13: Our proposed reaction path for the formation of Ammonia. Each line colour corresponds to a specific level of Hydrogenation (black: none, blue: one, red: two, green: three, brown: four), dashed lines are less-stable variants of the same specie. The horizontal axis is the number of Hydrogen atoms on the catalyst surface and on $N_2$. Vertical lines represent proposed transitions; when possible we have added the barrier profile next to the arrow. The energies of transition states are reported.

The subsequent Hydrogenation steps have much lower barriers; the second one is slightly higher than 1 eV, which implies a reaction rate of more than $10^7$ Hz, even at the lower temperature. The last Hydrogenation that we have examined in detail, the third one, presents an even smaller barrier (about 0.69 eV) which can be crossed with no effort at the experimental conditions. We wish to remark that some transitions that from the picture appear more convenient are not directly possible, as they involve two simultaneous Hydrogenation; e.g. the transition from trans-diazine to hydrazine in the 4H region.

When examining each reaction step individually it is easy to overlook the importance of continuous Hydrogen supply. However, when looking at the whole reaction, it appears clear how this mechanism can prevent the reaction from proceeding backward. With each addition of Hydrogen the more Hydrogenated species become more favoured with respect

to the least Hydrogenated ones; at the same time the lack of free surface sites can make it impossible, or very unlikely, for Hydrogen atoms to rebind to Palladium. For this to happens the typical transfer rate of Hydrogen atoms from the bulk and from the gas phase to the surface must be faster than the inverse-reaction steps; this is actually true, with the possible exception of the first Hydrogenation.

To conclude this section we want to estimate the macroscopic Ammonia production rate and compare it to the experimental values. We have just seen how we can expect a reaction rate $k$ of $10^4 - 10^5$ Hz, for the rate limiting step; this means that each $N_2$-*occupied* surface site will produce two Ammonia molecules in a time between $10^{-5}$ and $10^{-4}$ seconds. The number of occupied sites ($N_{N2}$) have been estimated in section 5.5.1 to be of the order of $10^7$. We can therefore estimate the macroscopic production rate as: $= N_{N2^\star} * k$; which is of the order of $10^{11} - 10^{12}$ $NH_3$ per second. This rate correspond to approximately $10^{-11} - 10^{-12}$ mol/sec of Ammonia. It is however important to keep in mind that DFT calculation can easily be inaccurate to the order of 10 meV or more; being the reaction rate exponentially dependent on the reaction energy barrier it is only meaningful as an order of magnitude.

In the experiment the measured production rate ranged from a minimum of $10^{-13}$ mol/sec for the double-chamber experiment to a maximum of $10^{-9}$ mol/sec for the single-chamber one. The other physical parameters that contribute to determining the rate are the partial pressure of the reactants, the temperature and the cell potential; these parameters can easily change the reaction rate by two orders of magnitude. Also the physisorption energy of $N_2$ plays a critical role in determining the Ammonia production rate; we have seen in section 5.3.1 how it can increase by a factor 2 or more on surface steps and defects. In light of these facts, we can consider our calculations to be in good agreement with experiment.

We have proposed a viable and previously unstudied reaction path – the Hydrogenation of Nitrogen prior to its decomposition – which can offer some insight on the experiment; we have also ruled out the possibility of direct Nitrogen decomposition, which cannot explain the experiment by many orders of magnitude. The proposed reaction path can likely be

improved and examined with higher accuracy, nevertheless we believe it is already sufficient to explain the fundamental of reaction mechanism.

# Conclusions

Let's review briefly our work and draw some conclusions. We have started, in the introduction, by stating the importance of Ammonia synthesis, how its production on industrial scale requires a huge amount of energy and resources in order to meet the increasing request from the market. We have then seen (chap. 1) the normal industrial setup, based on the Haber-Bosch process. It requires quite high temperature, to make the dissociation of $N_2$ possible, and very high pressure, to move the chemical equilibrium toward Ammonia. We have also reviewed an experiment [49] where the production of Ammonia has been performed at low atmospheric pressure, using an electro-chemical method to supply the required energy and Hydrogen.

In the experiment, a perovskite proton-conductor was coated on two sides by Palladium granular films, which, when connected to a voltage source, act as an anode and a cathode. The Hydrogen that dissociates on the anode is then stripped of its electron, which travels thorough the external circuit, while the proton crosses the perovskite to resurface on the anode where it recombines with the electron. The experiment showed the occurrence of a non-Faradayc Electrochemical Modification of Catalytic Reaction (NEMCA), which requires the structure of the catalyst, in this case Palladium, to be substantially modified.

This NEMCA effect is what we have tackled in our work. In the framework of Density-Functional Theory (chap. 2), using the tools available from the Quantum-ESPRESSO plane-wave based code distribution [28] we have constructed a model of the catalyst from first principles. We have used Born-Oppenheimer and the Projector-Augmented Waves (PAW)

method to model the atoms; BFGS structural optimisation, to characterize the intermediate reaction steps, and the Nudged-Elastic Band method to estimate the reaction barriers (chap. 2 and 3).

We have dedicated the entire chapter 4 to the study of the Palladium catalyst nano-scale structure. We have constructed a simplified, but realistic, model of the experimental conditions where the effect of active Hydrogen pumping can increase the bulk Palladium Hydrogen population to very high level. The ratio of Hydrogen over Palladium atoms in bulk can exceed 50%, where a phase transition occurs. The resulting structure, a Palladium Hydride, can have tetrahedral or octahedral site occupation, depending on the details of preparation. According to our DFT calculations, we found the tetrahedral one to be favoured. In both cases the Palladium lattice constant increases by about 3.5%, which changes substantially the property of surface atoms. In the resulting structure the surface Palladium atoms have a lower coordination number, which can increase their reactivity and cause the surface to exhibit a strong magnetisation, of the order of 0.75 $\mu_B$ per surface atom.

The modification of the surface structure also changes the surface population substantially, as surface energy becomes less favoured with respect to the bulk adsorption. Hydrogen surface population decreases, with respect to pure Palladium, increasing the number of potential adsorption sites for $N_2$; Nitrogen adsorption energy is slightly increased, although it remains low (about 0.26 eV per molecule).

Under these specific conditions direct Nitrogen dissociation is not possible, the adsorption energy of atomic Nitrogen is consistent, but still very low compared to the strong triple bond of $N_2$. For these reasons we have explored (chap. 5) the possibility of direct Hydrogenation of $N_2$ occurring prior to dissociation. We have found the first Hydrogenation to be the rate-limiting step, with a reaction barrier of almost 1.6 eV; although high, it can still be crossed at the experimental temperature (about 750°).

Subsequent steps have much lower barriers, no more than 1 eV; at each step the absolute energy of subsequent reaction steps decreases steadily (i.e. they become more and more favoured) and the N–N distance increases up to 20% compared to its value in the $N_2$

molecule. Hydrazine ($N_2H_4$) is formed after four hydrogenations; we checked that further hydrogenation are no more energetically favoured. On the other hand, breaking the N–N bond becomes likely as the energy of two adsorbed $NH_2$ molecule is similar to the one of adsorbed Hydrazine. From $NH_2$ the formation of Ammonia is practically bound to happen, being energetically very favoured. Another possibility is the simultaneous breaking of the N–N bond and formation Ammonia, which can desorb with no significant barrier.

We have estimated the reaction rate to be of the order of $10^{-11}$ to $10^{-12}$ mol/s, which, albeit low is compatible with the experimental ones. We found the most critical points to be the energy barrier of the first Hydrogenation, which can be difficult to change, and the low physisorption rate of Nitrogen molecules. The adsorption rate can be improved by increasing the partial pressure of Nitrogen, in the experiment $N_2$ has been supplied mixed with Helium; according to our estimate, supplying it pure would be enough to increase the reaction rate by two orders of magnitude.

# Bibliography


[1] P. C. Aben and W. G. Burgers. Surface Structure and Electrochemical Potential of Palladium While Absorbing Hydrogen in Aqueous Solution. *Trans. Faraday Soc.*, 58:1989 – 1992, 1962.

[2] Arthur W. Adamson. *Physical Chemistry of Surfaces*. John Wiley and Sons, 1990.

[3] Simone S. Alexandre, Maurizio Mattesini, Jose M. Soler, and Felix Yndurain. Comment on "Magnetism in Atomic-Size Palladium Contacts and Nanowires". *Physical Review Letters*, 96(7):079701, 2006.

[4] O. Krogh Andersen. Linear Methods in Band Theory. *Phys. Rev. B*, 12(8):3060–3083, Oct 1975.

[5] Avery Andrews. *Numerical Recipes in Fortran 77*, volume 1. University of Cambridge, 1986.

[6] V. Azambuja, S. Miraglia, D. Fruchart, S. Tavares, D. dos Santos, and M. Mezouar. In Situ X-ray Diffraction Analysis of the Pd-H System at High Pressure. *Journal of Alloys and Compounds*, 404-406:77 – 81, 2005. Proceedings of the 9th International Symposium on Metal-Hydrogen Systems, Fundamentals and Applications (MH2004), The International Symposium on Metal-Hydrogen Systems, Fundamentals and Applications, MH2004.

[7] R. Baranoya, R. Khodryrey, and R. Imamoy. *Sov. Phys. Cryst.*, 25:736, 1980.

[8] Stefano Baroni, Stefano de Gironcoli, Andrea Dal Corso, and Paolo Giannozzi. Phonons and Related Crystal Properties from Density-Functional Perturbation theory. *Rev. Mod. Phys.*, 73(2):515–562, Jul 2001.

[9] Lennart Bengtsson. Dipole Correction for Surface Supercell Calculations. *Phys. Rev. B*, 59(19):12301–12304, May 1999.

[10] Peter E. Blöchl, O. Jepsen, and O. K. Andersen. Improved Tetrahedron Method for Brillouin-Zone Integrations. *Phys. Rev. B*, 49(23):16223–16233, Jun 1994.

[11] Carl Bosch. *Nobel Lectures, Chemistry 1922-1944*. Elsevier Publishing Company, Amsterdam, 1966.

[12] C. G. Broyden. The Convergence of a Class of Double-Rank Minimization Algorithms. *Journal of the Institute of Mathematics and Its Applications*, 6:76–90, 1970.

[13] D. M. Ceperley and B. J. Alder. Ground State of the Electron Gas by a Stochastic Method. *Phys. Rev. Lett.*, 45(7):566–569, Aug 1980.

[14] Barbara Chapman, Gabriele Jost, and Ruud van der Pas. *Using OpenMP: Portable Shared Memory Parallel Programming*. The MIT Press, 2007.

[15] Malcom W. Chase, Jr. *NIST-JANAF Thermochemical Tables*. National Institute of Standards and Technology, fourth edition, 1990.

[16] Xiaowei Chen, Tao Zhang, Mingyuan Zheng, Zili Wu, Weicheng Wu, and Can Li. The Reaction Route and Active Site of Catalytic Decomposition of Hydrazine over Molybdenum Nitride Catalyst. *Journal of Catalysis*, 224(2):473 – 478, 2004.

[17] H. Conrad, M. E. Kordesch, R. Scala, and W. Stenzel. *Spectrosc. Relat. Phenom.*, 90, 1979.

[18] H. P. Crowder and P. Wolfe. Linear Convergence of the Conjugate Gradient Method. *IBM J. Res. Develop.*, 16:431–433, 1972.

[19] Larry A. Curtiss, Krishnan Raghavachari, Paul C. Redfern, and John A. Pople. Assessment of Gaussian-2 and Density Functional Theories for the Computation of Enthalpies of Formation. *The Journal of Chemical Physics*, 106(3):1063–1079, 1997.

[20] B. Daoudi, M. Sehil, A. Boukraa, and H. Abid. FP-LAPW Calculations of Ground State Properties for AlN, GaN and InN Compounds. *Int. J. nanoelectronics and Materials*, 1:65–79, 2008.

[21] A. Delin, E. Tosatti, and R. Weht. Magnetism in Atomic-Size Palladium Contacts and Nanowires. *Phys. Rev. Lett.*, 92(5):057201, Feb 2004.

[22] A. Delin, E. Tosatti, and Ruben Weht. Delin, Tosatti, and Weht Reply. *Physical Review Letters*, 96(7):079702, 2006.

[23] M. Dion, H. Rydberg, E. Schröder, D. C. Langreth, and B. I. Lundqvist. Van der Waals Density Functional for General Geometries. *Phys. Rev. Lett.*, 92(24):246401, Jun 2004.

[24] Oliver Einsle, F. Akif Tezcan, Susana L. A. Andrade, Benedikt Schmid, Mika Yoshida, James B. Howard, and Douglas C. Rees. Nitrogenase MoFe-Protein at 1.16 Å Resolution: A Central Ligand in the FeMo-Cofactor. *Science*, 297(5587):1696–1700, 2002.

[25] D. H. Everett and P. Nordon. Hysteresis in the Palladium + Hydrogen System. *Proc. R. Soc. Lond.*, 259:341–360, 1960.

[26] T. E. Felter, Erik C. Sowa, and M. A. Van Hove. Location of Hydrogen Adsorbed on Palladium (111) Studied by Low-Energy Electron Diffraction. *Phys. Rev. B*, 40(2):891–899, Jul 1989.

[27] R. Fletcher. A New Approach to Variable Metric Algorithms. *Computer Journal*, 13:317–322, 1970.

[28] Paolo Giannozzi, Stefano Baroni, Nicola Bonini, Matteo Calandra, Roberto Car, Carlo Cavazzoni, Davide Ceresoli, Guido L Chiarotti, Matteo Cococcioni, Ismaila Dabo, Andrea Dal Corso, Stefano de Gironcoli, Stefano Fabris, Guido Fratesi, Ralph Gebauer,

Uwe Gerstmann, Christos Gougoussis, Anton Kokalj, Michele Lazzeri, Layla Martin-Samos, Nicola Marzari, Francesco Mauri, Riccardo Mazzarello, Stefano Paolini, Alfredo Pasquarello, Lorenzo Paulatto, Carlo Sbraccia, Sandro Scandolo, Gabriele Sclauzero, Ari P Seitsonen, Alexander Smogunov, Paolo Umari, and Renata M Wentzcovitch. QUANTUM ESPRESSO: a Modular and Open-Source Software Project for Quantum Simulations of Materials. *Journal of Physics: Condensed Matter*, 21(39):395502, 2009.

[29] D. Goldfarb. A Family of Variable Metric Updates Derived by Variational Means. *Mathematics of Computation*, 24:23–26, 1970.

[30] Jie Guan, Stephen E. Dorris, Uthamalingam Balachandran, and Meilin Liu. Transport Properties of $SrCe_{0.95}Y_{0.05}O_3$-$\delta$ and Its Application for Hydrogen Separation. *Solid State Ionics*, 110(3-4):303 – 310, 1998.

[31] Fritz Haber. *Nobel Lectures, Chemistry 1901-1921.* Elsevier Publishing Company, Amsterdam, 1966.

[32] Greg Mills Hannes Jonsson and Karsten W. Jacobsen. *Nudged Elastic Band Method for Finding Minimum Energy Paths of Transitions In Classical and Quantum Dynamics in Condensed Phase Simulations.* World Scientific, Singapore, 1998.

[33] H. Hemmes, A. Driessen, R. Griessen, and M. Gupta. Isotope effects and Pressure Dependence of the $TC$ Of Superconducting Stoichiometric PdH and PdD Synthesized and Measured in a Diamond Anvil Cell. *Phys. Rev. B*, 39(7):4110–4118, Mar 1989.

[34] Graeme Henkelman and Hannes Jonsson. Improved Tangent Estimate in The Nudged Elastic Band Method for Finding Minimum Energy Paths and Saddle Points. *The Journal of Chemical Physics*, 113(22):9978–9985, 2000.

[35] Graeme Henkelman, Blas P. Uberuaga, and Hannes Jonsson. A Climbing Image Nudged Elastic Band Method for Finding Saddle Points and Minimum Energy Paths. *The Journal of Chemical Physics*, 113(22):9901–9904, 2000.

[36] P. Hohenberg and W. Kohn. Inhomogeneous Electron Gas. *Phys. Rev.*, 136(3B):B864–B871, Nov 1964.

[37] D. D. Johnson. Modified Broyden's Method for Accelerating Convergence in Self-Consistent Calculations. *Phys. Rev. B*, 38(18):12807–12813, Dec 1988.

[38] M. Kawata, C. M. Cortis, and R. A. Friesner. Efficient Recursive Implementation of the Modified Broyden Method and the Direct Inversion in the Iterative Subspace Method: Acceleration of Self-Consistent Calculations. *The Journal of Chemical Physics*, 108(11):4426–4438, 1998.

[39] I. M. Klotz and R. M. Rosemberg. *Chemical Thermodinamics*. John Wiley and Sons, 1994.

[40] W. Kohn and L. J. Sham. Self-Consistent Equations Including Exchange and Correlation Effects. *Phys. Rev.*, 140(4A):A1133–A1138, Nov 1965.

[41] Anton Kokalj. Computer Graphics and Graphical User Interfaces as Tools in Simulations of Matter at the Atomic Scale. *Computational Materials Science*, 28(2):155 – 168, 2003. Proceedings of the Symposium on Software Development for Process and Materials Design.

[42] G. Kresse and D. Joubert. From Ultrasoft Pseudopotentials to the Projector Augmented-Wave Method. *Phys. Rev. B*, 59(3):1758–1775, Jan 1999.

[43] A Kuki and PG Wolynes. Electron Tunneling Paths in Proteins. *Science*, pages 1647–1652, 1987.

[44] Chengteh Lee, Weitao Yang, and Robert G. Parr. Development of the Colle-Salvetti Correlation-Energy Formula into a Functional of the Electron Density. *Phys. Rev. B*, 37(2):785–789, Jan 1988.

[45] M Levy. *Universal Variational Functionals of Electronic Densities, First-Order Density Matrices, and Natural Spin-Orbitals and Solution of the N-Representability Problem.* Proc. Nat. Acad. Sci., USA 76:6062, 1979.

[46] Mel Levy. Electron Densities in Search of Hamiltonians. *Phys. Rev. A*, 26(3):1200–1208, Sep 1982.

[47] F.A. Lewis. *The Palladium Hydrogen System.* New York: Accademic, 1966.

[48] George Marnellos, Olga Sanopoulou, Areti Rizou, and Michael Stoukides. The Use of Proton Conducting Solid Electrolytes for Improved Performance of Hydro- and Dehydrogenation Reactors. *Solid State Ionics*, 97(1-4):375 – 383, 1997.

[49] George Marnellos and Michael Stoukides. Ammonia Synthesis at Atmospheric Pressure. *Science*, 282(5386):98–100, 1998.

[50] George Marnellos, Stergios Zisekas, and Michael Stoukides. Synthesis of Ammonia at Atmospheric Pressure with the Use of Solid State Proton Conductors. *Journal of Catalysis*, 193(1):80 – 87, 2000.

[51] R. M. Martin. *Electronic Structure.* Cambridge University Press, 2004.

[52] Nicola Marzari, David Vanderbilt, Alessandro De Vita, and M. C. Payne. Thermal Contraction and Disordering of the Al(110) Surface. *Phys. Rev. Lett.*, 82(16):3296–3299, Apr 1999.

[53] Message Passing Interface Forum. *Int. J. Supercomputer Applications*, 8 (3/4):165–414, 1994.

[54] M. Methfessel and A. T. Paxton. High-Precision Sampling for Brillouin-Zone Integration In Metals. *Phys. Rev. B*, 40(6):3616–3621, Aug 1989.

[55] Hendrik J. Monkhorst and James D. Pack. Special Points for Brillouin-Zone Integrations. *Phys. Rev. B*, 13(12):5188–5192, Jun 1976.

[56] S. G. Neophytides, D. Tsiplakides, P. Stonehart, M. M. Jaksic, and C. G. Vayenas. Electrochemical Enhancement of a Catalytic Reaction in Aqueous Solution. *Nature*, 370(6484):45–47, Jul 1994. 10.1038/370045a0.

[57] Joachim Paier, Robin Hirschl, Martijn Marsman, and Georg Kresse. The Perdew–Burke–Ernzerhof Exchange-Correlation Functional Applied to the G2-1 Test Set Using a Plane-Wave Basis Set. *The Journal of Chemical Physics*, 122(23):234102, 2005.

[58] Joachim Paier, Martijn Marsman, and Georg Kresse. Why Does the B3lyp Hybrid Functional Fail for Metals? *The Journal of Chemical Physics*, 127(2):024103, 2007.

[59] E. Panagos, I. Voudouris, and M. Stoukides. Modelling of Equilibrium Limited Hydrogenation Reactions Carried Out in H+ Conducting Solid Oxide Membrane Reactors. *Chemical Engineering Science*, 51(11):3175 – 3180, 1996. Chemical Reaction Engineering: From Fundamentals to Commercial Plants and Products.

[60] J.-F. Paul and P. Sautet. Density-Functional Periodic Study of the Adsorption Of Hydrogen on a Palladium (111) Surface. *Phys. Rev. B*, 53(12):8015–8027, Mar 1996.

[61] P.E.Blöchl. Projector Augmented-Wave Method. *Phys. Rev. B*, 50(24):17953, Dec. 1994.

[62] G. Pekridis, K. Kalimeri, N. Kaklidis, C. Athanasiou, and G. Marnellos. Electrode Polarization Measurements in the $FeSrCe_{0.95}Yb_{0.05}O_{2.975}Au$ Proton Conducting Solid Electrolyte Cell. *Solid State Ionics*, 178(7-10):649 – 656, 2007. 13th Solid State Proton Conductors Conference.

[63] J. P. Perdew and Alex Zunger. Self-Interaction Correction to Density-Functional Approximations for Many-Electron Systems. *Phys. Rev. B*, 23(10):5048–5079, May 1981.

[64] John P. Perdew, Kieron Burke, and Matthias Ernzerhof. Generalized Gradient Approximation Made Simple. *Phys. Rev. Lett.*, 78(7):1396, Feb 1997.

[65] John P. Perdew and Yue Wang. Accurate and Simple Analytic Representation of the Electron-Gas Correlation Energy. *Phys. Rev. B*, 45(23):13244–13249, Jun 1992.

[66] A. Pundt and R. Kirchheim. Hydrogen in Metals: Microstructural Aspects. *Annual Review of Materials Research*, 36(1):555–608, 2006.

[67] Karsten Reuter and Matthias Scheffler. Composition, Structure, and Stability of $RuO_2(110)$ as a Function of Oxygen Pressure. *Phys. Rev. B*, 65(3):035406, Dec 2001.

[68] T. H. Rod, A. Logadottir, and J. K. Norskov. Ammonia Synthesis at Low Temperatures. *The Journal of Chemical Physics*, 112(12):5343–5347, 2000.

[69] Takaaki Sakai, Hiroshige Matsumoto, Reiri Yamamoto, Takao Kudo, Sachio Okada, Masato Watanabe, Shin ichi Hashimoto, Hitoshi Takamura, and Tatsumi Ishihara. Performance of Palladium Electrode for Electrochemical Hydrogen Pump Using Strontium-Zirconate-based Proton Conductors. *Ionics*, 15(6):665–670, 2009.

[70] C. N. Satterfield. *Heterogeneous Catalysis in Practice*. McGraw-Hill, 1980.

[71] Carlo Sbraccia. *Computer Simulation of Thermally Activated Processes*. SISSA (PhD Thesis), Trieste, Italy, 2005.

[72] SA Semiletov, RV Baranova, YP Khodyrev, and RM Imamov. Electron-Diffraction Studies of a Tetragonal Hydride PdH. *Kristallografiya*, 25(6):1162–1168, 1980.

[73] D. F. Shanno. Conditioning of Quasi-Newton Methods for Function Minimization . *Mathematics of Computation*, 24:647–656, 1970.

[74] Jrn Ilja Siepmann and Daan Frenkel. Configurational Bias Monte Carlo: a New Sampling Scheme for Flexible Chains. *Molecular Physics: An International Journal at the Interface Between Chemistry and Physics*, 75:59–70, 1992.

[75] A. Skodra, M. Ouzounidou, and M. Stoukides. $NH_3$ Decomposition in a Single-Chamber Proton Conducting Cell. *Solid State Ionics*, 177(26-32):2217 – 2220, 2006. Solid State Ionics 15: Proceedings of the 15th International Conference on Solid State Ionics, Part II.

[76] J. C. Slater. A Simplification of the Hartree-Fock Method. *Phys. Rev.*, 81(3):385–390, Feb 1951.

[77] R. N. F. Thorneley, D. J. Lowe, and Editor T. G. Spiro. *Molybdenum Enzymes, Chapter 5*. Wiley-Interscience, New York, 1985.

[78] N. Troullier and José Luriaas Martins. Efficient Pseudopotentials for Plane-Wave Calculations. *Phys. Rev. B*, 43(3):1993–2006, Jan 1991.

[79] David Vanderbilt. Soft Self-Consistent Pseudopotentials in a Generalized Eigenvalue Formalism. *Phys. Rev. B*, 41(11):7892–7895, Apr 1990.

[80] C. G. Vayenas, S. Bebelis, and S. Neophytides. Non-Faradaic Electrochemical Modification of Catalytic Activity. *The Journal of Physical Chemistry*, 92(18):5083–5085, May 2002. doi: 10.1021/j100329a007.

[81] S. H. Vosko, L. Wilk, and M. Nusair. Accurate Spin-Dependent Electron Liquid Correlation Energies for Local Spin Density Calculations: a Critical Analysis. *Can. J. Phys.*, 58:1200–1211, 1980.

[82] Li Zhou and Yaping Zhou. Determination of Compressibility Factor and Fugacity Coefficient of Hydrogen in Studies of Adsorptive Storage. *International Journal of Hydrogen Energy*, 26(6):597 – 601, 2001.

# Acknowledgements

Part of the calculations included in this work has been performed at the CINECA consortium in Bologna; I wish to thank the CINECA staff for all the assistance, in particular Carlo Cavazzoni, Ivan Girotto and Andrew Emerson. I also wish to thank the HPC staff at SISSA, in particular Stefano Cozzini, Piero Calucci and Moreno Baricevic.

I wish to thank all the authors and collaborators of Quantum-ESPRESSO included, but not limited to, all the authors of ref. [28]. A special thanks goes to Paolo Giannozzi, for its invaluable management of the entire project, and Stefano Baroni for its efforts to push the limits forward.

One of the most important acknowledgements goes of course to Stefano de Gironcoli, for his support during the course of the PhD and for being always available for help. I especially wish to thank him for stressing the importance of consistency, accuracy and integrity in scientific research.

During the last three years I have collaborated, argued or just enjoyed some time with many students and young researchers at SISSA. It would be too long to list all of them, here are the initials of those I can recall: AM AP AS CE EK GB GC GP GS JFC MC MS NLN OBS PC SB TC YC.

The most personal thanks goes to Paola, to my family and to my friends for helping and supporting me in every possible way.